Progress towards GaAs multiplexed single-electron pump arrays

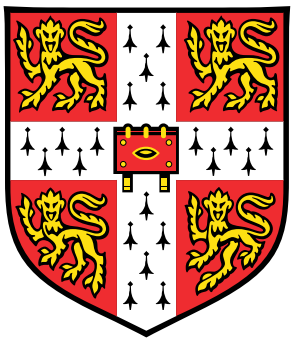

Teng Yi

Department of Physics

University of Cambridge

This dissertation is submitted for the degree of Doctor of Philosophy

Jesus College

November 2018

Declaration

I hereby declare that except where specific reference is made to the work of others, the contents of this dissertation are original and have not been submitted in whole or in part for consideration for any other degree or qualification in this, or any other university. This dissertation is my own work and contains nothing which is the outcome of work done in collaboration with others, except as specified in the text and Acknowledgements. This dissertation contains fewer than 65,000 words including appendices, bibliography, footnotes, tables and equations and has fewer than 150 figures.

Teng Yi
November 2018

Abstract

Progress towards GaAs multiplexed single-electron pump arrays
Teng Yi

In this thesis we present progress towards making multiplexed GaAs single-electron pump arrays. The single-electron pump is a device for transferring an accurate integer number n of electrons per cycle to generate precise current $I = nef$, where f is the frequency of the periodic AC voltage applied and e is the electron charge. Multiplexing electron pumps may also allow the pumps to be measured in parallel, increasing the output current and thereby enabling a higher accuracy reading.

Firstly, a 4 x 32 multiplexed wide-channel electron pump array is studied and we observe a large rectified current (about 100 μA) instead of a pumping current (which would be 18 pA at 110 MHz). We designed several variations of single wide-channel electron pump devices and found out that the rectified current is from the wide-channel electron pump and not the multiplexer. We developed a model to qualitatively explain the origin of rectified current in the wide-channel electron pump devices and investigate the effects of changing the RF frequency and amplitude on the rectified current.

Secondly, we characterise the transmission of RF voltage signals through the quantum multiplexer using an array of bar gates. We find that about 300 mV AC amplitude voltage can be transmitted to the bar gate device, which may be sufficiently large for an electron pump to operate. We also present the statistical study of multiplexed bar gate devices. We find that 0.1 μm wide bar gates are different from 0.2 μm wide bar gate or wider gates: more negative voltage is needed to pinch off 0.1 μm wide bar gates, because 0.1 μm is comparable with the 2DEG depth. We redesign the multiplexer structure and determine that the capacitance of the multiplexer is about 1.93 pF which will help the future multiplexed single-electron pump array design to give best RF power transmission.

Thirdly, since gate insulators are required in the multiplexed electron pump design. We demonstrate electron pumping in a single-electron pump device in which the gates

extend across the entire GaAs channel, and are insulated from the GaAs channel by a polyimide layer as required in the multiplexed design. We also study how design variations such as the pump gates design (quantum dot radius and tunnel barrier width), channel etch design and order of fabrication will affect the RF power required to observe clear quantised pumping. Based on the above results, we present our designs for full GaAs multiplexed electron pump arrays.

Acknowledgements

I would like to begin my thanking my supervisor Professor Charles Smith, for giving me the opportunity to study for this PhD here in Cambridge. His belief in my abilities and continued enthusiasm sustained my inspiration in the overwhelming and sometimes frustrating project. Charles, even though he is so busy, always made himself available for discussion and advice whenever I went to his office. He is also considerable for all the aspects of my PhD study in Cambridge and he is always ready to help when I meet difficulties in my life.

Many thanks goes to Dr Joanna Waldie. My thanks to Joanna is beyond words can describe. My project would not have existed without the work she completed during her PhD. She is an extremely talented scientist. From designing the mask, measurement setup, carrying out experiments, data analysis to thesis correction, Joanna helped me every aspect of my project. Your patience and efforts have been outstanding! Also her successful collaboration with National Physical Laboratory (NPL) gave me the chance to discuss with the scientists there.

I would like to say a big thank-you to Dr Luke Smith. In my last year of my PhD, I am really lucky to catch up with Luke's return to SP Group. His suggestions on measurements and device design really help this project. Also his day-to-day based comments on thesis correction push me to have the best way to present this work. I will always keep the tons of hand-writing thesis comments from Luke to remember the unforgettable PhD.

I would say a special thanks to Dr Patrick See. He is probably the champion of pump device fabrication all over the world. From him you can really understand what focus and profession means. Thanks Patrick for the help of fabrication and useful discussion of designing the devices.

I am grateful to Dr Reuben Puddy, Dr Kaveh Delfanazari and Dr Stephen Flemming for his help during my PhD. I also like to thank the people in the multiplexer project: Pengcheng, Moda, Gulzat and Jack. I also appreciate the help from NPL: Dr Masaya Kataoka, Dr Stephen Giblin, Dr Jonathan Fletcher and Dr Ateeq Nasir. I am thankful

to all the members of SP, who have helped me in many ways throughout the course of this PhD. Thanks for Prof. David Ritchie for his leadership of the group. Especially for Yuqing, Jinggao, Binbin, Hangtian, Shuwei, Ziwei, Wenting and Xinya, chatting with you for a break always give me energy to come back to experiments.

I also want to thank my girlfriend- Lu Bai, who is a very lovely and kind girl. Your accompany means a lot to me, making me brave and confident to face the difficulties during the PhD study. I am so happy that we can graduate from this famous university together!

I also would like to thank my friends in Cambridge who have made my PhD life colourful: Jiaqiang Wang, Xie Chen, Zhen Tong, Hangtian Hou, Chunyang Wu, Chao Yun *et al*.

Lastly, the greatest ‘thank you‘ goes to my family: Dad, Mom, my older brother, my sister in law and my nephew. I always feel being loved by you. I am grateful for you and thanks for your constant support! I Love you!

Table of Contents

1

Introduction

There are seven base units in the International System of Units: the metre for measurement of length, the kilogram for mass, the second for time, the ampere for electric current, the kelvin for temperature, the candela for luminous intensity, and the mole for amount of substance [1]. At present, the definition of the ampere is based on electromechanical force: the ampere is that "constant current which, if maintained in two straight parallel conductors of infinite length, of negligible circular cross section, and placed 1 metre apart in vacuum, would produce between these conductors a force equal to 2×10^{-7} newton per metre of length" [1]. However, infinite-length, zero-cross-sectional-area wires and vacuum in the definition cannot be realised perfectly. Researchers are developing new ways to use the fundamental constant electron charge e to redefine the ampere, which could measure the quantum current standard precisely [2–5].

To realize a quantum current standard, tunable-barrier single-electron pumps are promising candidates. The tunable-barrier single-electron pump fabricated on semiconductors is a device transferring an accurate integer number n of electrons per cycle to generate precise current $I = nef$. Here f is the frequency of the periodic AC voltage applied to modulate the barrier, whose relative uncertainty can be controlled under 1 part in 10^{10} [6]. Significant improvements have been made since the device

was first demonstrated by Blumenthal *et al.* in 2007 [2]: currently state of the art error rates are 0.16 ppm at 600 MHz (96.1 pA) [7] and 0.3 ppm at 1 GHz (160.2 pA) [8]. However, even better accuracy, a current at least 100 pA with error rate less than 1 part in 10^7, is required to redefine the electrical standards.

The cryogenic on-chip quantum multiplexer is a multilayer structure developed on a GaAs/AlGaAs heterostructure allowing many devices to be measured at the same time [9]. The quantum multiplexer has been applied to study the statistics of fabrication yield, reproducibility [9] and interesting quantum effects such as so-called '0.7 structure' [10] on one-dimensional wires [11]. In this thesis we want to extend the multiplexer application to quantum metrology redefining the ampere.

Multiplexing electron pumps may allow pumps to be measured in parallel, increasing the total output current and realizing a higher accuracy reading [12, 13]. And also the quantum multiplexer architecture could allow the measurement of a large number of electron pumps to be carried out in a single cryogenic cool-down using a limited number of measurement wires. Therefore we can also evaluate electron pumps with different designs on a single chip within a cool down.

Here we present progress towards realising such multiplexed pump arrays. The thesis is organised as follows: Chapter 1 introduces the motivation for this study which is the redefinition of the ampere base unit, the concept of the electron pump and quantum multiplexer, and the benefits of multiplexed electron pump arrays. Chapter 2 presents background theory of the semiconductor devices relating to the work presented in subsequent chapters: low-dimensional transport, Coulomb Blockade, and single-electron transport. Chapter 3 describes the design and processes of fabricating devices and low-temperature measurement techniques employed in this thesis. Chapter 4 introduces the reason of designing the wide-channel electron pumps and how rectified current is observed in these devices. Then we present our work on the 4 x 32 multiplexed wide-channel electron pump array and single wide-channel electron pump device. Lastly, we develop a model to explain this rectified current. In chapter 5 we characterise the transmission of RF voltage signals through the quantum multiplexer using an array of bar gates. Also we use multiplexer to do the statistical study of bar gates with different gate widths and calculate the capacitance of the multiplexer. In chapter 6 we demonstrate that our design of single-electron pump with an insulator layer of polyimide added realizes quantised charge pumping. This is a necessary step to make multiplexed pump arrays. We measure several design variations of pump gates namely dot radius and the tunnel barrier width, channel etch design and order of fabrication and observe clear electron pumping. We discuss if there is a relationship between

the tunnel barrier width/dot radius and the power required to see charge pumping. Chapter 7 is a summary of our work and future research proposals.

2

Background

This chapter presents the background theory and literature review relevant to the work described in the following chapters. Firstly, we will introduce different low-dimensional semiconductor structures. Secondly, the development of single-electron pumps is presented. Lastly, we will describe the concept, design, operation and application of the quantum multiplexer technique.

2.1 Low-dimensional semiconductor structures

2.1.1 Two-dimensional electron gases and heterostructures

In a bulk semiconductor electrons will travel in three dimensions. With the development of 'band engineering' or 'wavefunction engineering' [14], the electrons can be confined to travel in two dimensions or even lower. A two-dimensional electron gas (2DEG) is a sheet of electrons which can only move freely in two dimensions. A large variety of quantum experiments can be carried out using 2DEGs. A particular realisation of 2DEG systems is semiconductor heterostructures, which are made up of more than one semiconductor material.

A typical GaAs/AlGaAs heterostructure is shown in Fig. 2.1 (a). The 2DEG is formed 90 nm below the wafer surface. The structure consists of a semi-insulating GaAs substrate on which a ∼1 μm of high-quality GaAs buffer layer is grown. Following this a 40 nm un-doped AlGaAs spacer is grown, which is used to keep the 2DEG a certain distance from the donors. This will reduce the scattering and increase the electron mobility of the 2DEG. After this a 40 nm Si-doped donor layer is grown to provide the electrons forming the 2DEG, following this a final 10 nm GaAs cap is grown on the top to prevent the Al content in the AlGaAs being oxidized. Because of the conduction band offset of GaAs and AlGaAs, the band profile forms a triangular potential well at the GaAs/AlGaAs interface, which is shown in Fig. 2.1 (b). At low temperature, the triangular potential well is so narrow that only the ground state wave function in the confinement direction is occupied. This means the electrons in the 2DEG can only move in two dimensions and a sheet of electrons parallel to the interface is formed. All the experiments measured in this thesis use a GaAs/AlGaAs heterostructure.

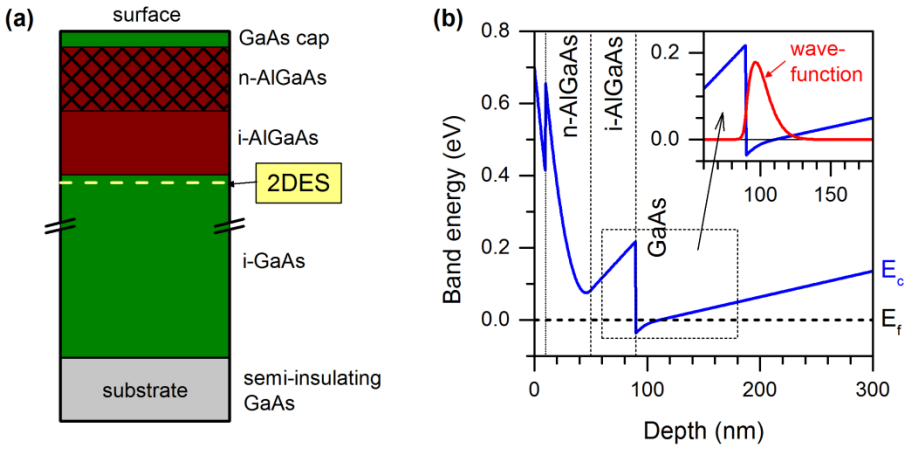

Figure 2.1: (a) Typical GaAs/AlGaAs wafer structure used in this work. (b) Band structure of the GaAs/AlGaAs heterostructure. Taken from [15].

We can get the density of states of a 2DEG from Schrödinger's equation for the electron motion in the z direction (perpendicular to the 2DEG) :

$$\left[-\frac{\hbar^2}{2m^*}\frac{d^2}{dz^2} + V(z)\right]\psi(z) = E\psi(z) \tag{2.1}$$

where $V(z)$ is the potential energy, $\psi(z)$ is the electron wavefunction and E is the energy. By solving the equation, the allowed energy states of confined electrons for a 2DEG can be given as:

$$E_i(k_x, k_y) = E_i + \frac{\hbar^2}{2m^*}\left(k_x^2 + k_y^2\right) \tag{2.2}$$

where m^* is the electron effective mass, h is Planck constant, $\hbar = \frac{h}{2\pi}$, $k_n, n\epsilon\{x, y\}$ is the wave vector and E_i are the quantised energy levels for electron motion in the z direction. In all of our work, only the first energy level ($i = 0$) is occupied. The density of states can be described as:

$$g_{2D}(E) = \frac{m^*}{\pi\hbar^2} \tag{2.3}$$

This assumes spin degeneracy (spin up and spin down electrons have the same energy). The density of states for a 2DEG system is presented in Fig. 2.2.

2.1.2 Quantum wire

Further reduction in dimensionality will lead to one-dimensional transport of electrons in a quantum wire. Starting with a 2DEG introduced above, another confinement in the perpendicular direction to the original confinement is added to the 2DEG. The lateral confinement can be realised by using a split-gate transistor [16] or etching to remove some of the material to create a narrow-channel of the 2DEG [17]. The width of the narrow channel can vary depending on the 2DEG carrier density. The energy states of the confined electrons in the quantum wire can be described as:

$$E_{i,j}(k_x) = E_i + E_j + \frac{\hbar^2 k_x^2}{2m^*} \tag{2.4}$$

where E_i are the quantised energies for motion in the z direction and E_j are the quantised energies in the y direction (perpendicular to the wire). In a typical device at low temperature, several of the quantum wire subbands (E_j levels) can be occupied. And the density of states function can be given by

$$g_{1D}(E) = \frac{2(2m^*)^{\frac{1}{2}}}{h} E^{-\frac{1}{2}} \tag{2.5}$$

This assumes spin degeneracy, and that the energy E is relative to the subband bottom ($E_{i,j}$). The density of states for a quantum wire system is shown in Fig. 2.2.

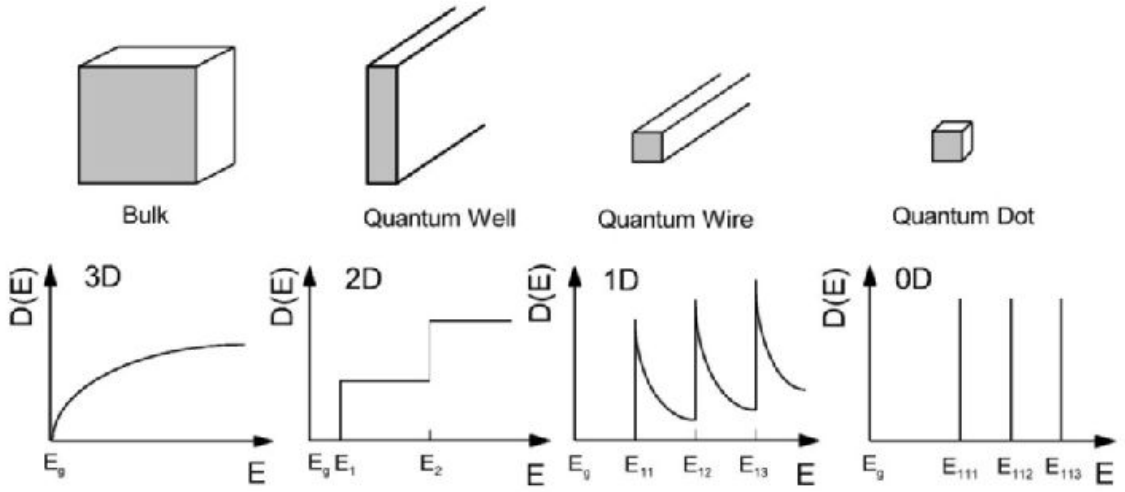

Figure 2.2: Schematic diagram of electronic density of states of different dimensionality. Taken from [18].

2.1.3 Quantum dot

For a small enough conducting island (smaller than the phase-coherence length of electrons), electrons can be confined in all three dimensions to form a quantum dot [19]. In this case only discrete energy levels are allowed. Quantum dots [20–22] can be defined by gates on a 2DEG [15] or by finger gates fabricated on quantum wires [2]. For the case of square well confinement in all three directions, the allowed energy states of the electrons confined in quantum dots can be described by:

$$E_{i,j,k} = \frac{h^2}{8m^*}\left(\frac{i^2}{L_z^2} + \frac{j^2}{L_y^2} + \frac{k^2}{L_x^2}\right) \tag{2.6}$$

where i, j and k are integers and L_x, L_y and L_z are the dimensions of the quantum dot. The density of states (shown in Fig. 2.2) is then:

$$g_{0D}(E) = \delta(E - E_{i,j,k}) \tag{2.7}$$

Additionally, there is an electrostatic energy cost e^2/C for adding an extra electron to the quantum dot, where C is the total capacitance of the dot. Figure 2.3 shows the schematic of a quantum dot and energy level diagram of the system. As the plunger gate is capacitively coupled to the dot, it can control the conductance through the dot, and is used to manipulate the energy levels of the dot, and can be tuned to raise or lower the possibility of an electron tunnelling on to or off the dot. At low temperature

electrons can only tunnel on and off the dot when one of the dot energy levels is lined up with the chemical potential μ_s, μ_d of the source and drain leads. If they are not aligned then no current can flow and this is the Coulomb blockade [23]. The devices studied in Chapter 6 are based on this principle.

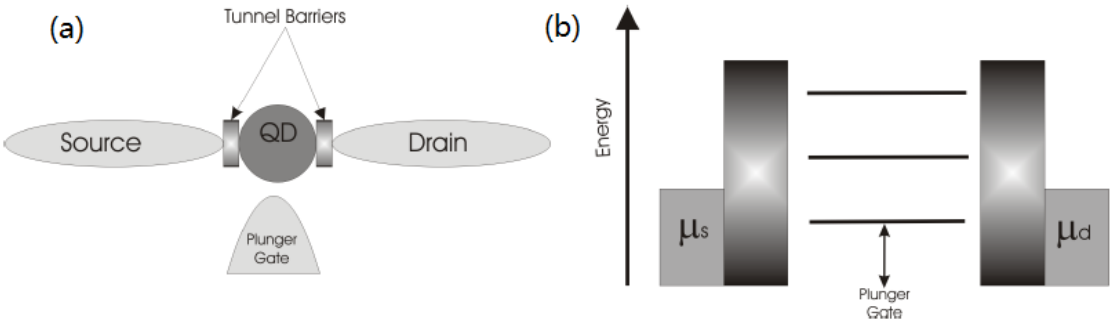

Figure 2.3: (a) Schematic diagram of a quantum dot. (b) Energy level diagram of the quantum dot. Taken from [24].

2.2 The single-electron pump

Researchers are interested in the single-electron pump for its metrology application: a quantum current stand and could be realised using the pump. We will present a literature review of the development of single-electron pumps. Lastly we will describe its application beyond metrology such as single-electron sources and quantum optics.

2.2.1 Metrology

Metrology is defined as "the science of measurement, embracing both experimental and theoretical determinations at any level of uncertainty in any field of science and technology" by the International Bureau of Weights and Measures (BIPM) [25].

In the field of electrical metrology, the Quantum Metrological Triangle (QMT) [26] experiment was proposed by K. Likhzrev and A. Zorin in 1985 [27]. A schematic of the Quantum Metrological Triangle is shown in Fig. 2.4. The QMT was proposed to use the fundamental constants-electron charge e and Plank's constant h to redefine the standards of electrical voltage, resistance and current.

For a quantum standard of electrical voltage, the Volt can be realised using the ac Josephson effect [29]: if an AC current at frequency f is applied to a Josephson junction, the voltage equals $hf/2e$ across the junction. As the frequency can be accurately

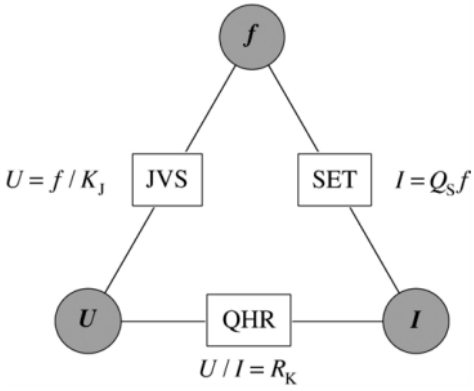

Figure 2.4: Schematic diagram of the Quantum Metrological Triangle. Taken from [28].

controlled, the Josephson voltage standard has been achieved with the error rate less than 0.01 ppm [6]. For the quantum standard of electrical resistance, the Ohm can be realised using the quantum Hall effect [30]: as the Hall resistance of a 2DEG is quantised to h/e^2, a quantum resistance standard can be precisely achieved.

However, for the current unit ampere, the ampere is still defined as the: "constant current which, if maintained in two straight parallel conductors of infinite length, of negligible circular cross section, and placed 1 metre apart in vacuum, would produce between these conductors a force equal to 2×10^{-7} newton per metre of length"[1]. Infinite-length, zero cross-sectional area wires and a vacuum in the definition cannot be realised perfectly. Researchers are developing new ways to use the fundamental constant electron charge e to redefine the ampere, in terms of a precise quantum current standard [2–5].

Based on quantum standards of electrical voltage and resistance, the electrical current can be redefined with Ohm's Law. However, if an independent quantum current standard can be realised using the fundamental constants, the new current definition can not only be precise but can also be used to examine the consistency of the quantum electrical standards via the closure of the Quantum Metrological Triangle. A current generated by electrons transported one-by-one through a quantum dot at an exact frequency is a possible way to redefine the quantum current standard.

2.2.2 Electron turnstiles and pumps

Single-electron turnstiles and pumps are two promising methods to transport an exact integer number n of electrons per cycle at frequency f, which can generate a precise current $I = nef$.

Quantum charge transport was first demonstrated in a single-electron turnstile by Geerligs *et al.* [31]. This device was fabricated using arrays of metallic (aluminium) islands separated by tunneling junctions (aluminium oxide). The chemical potentials of the dots could be modulated by the gates when RF signals were applied. The RF signal increases and decreases the possibility of electrons tunneling on and off the dot (via the Coulomb blockade), to produces a precise current. Figure 2.5 shows a semiconductor turnstile, where the RF signal modulates the tunnel barriers. The first single-electron pump was demonstrated by Pothier *et al.* in 1992 [32]. The device was also based on the periodic manipulation of the Coulomb blockade effect in metallic junctions. This device does not need a source-drain bias voltage and the current direction is only dependent on the gate voltages.

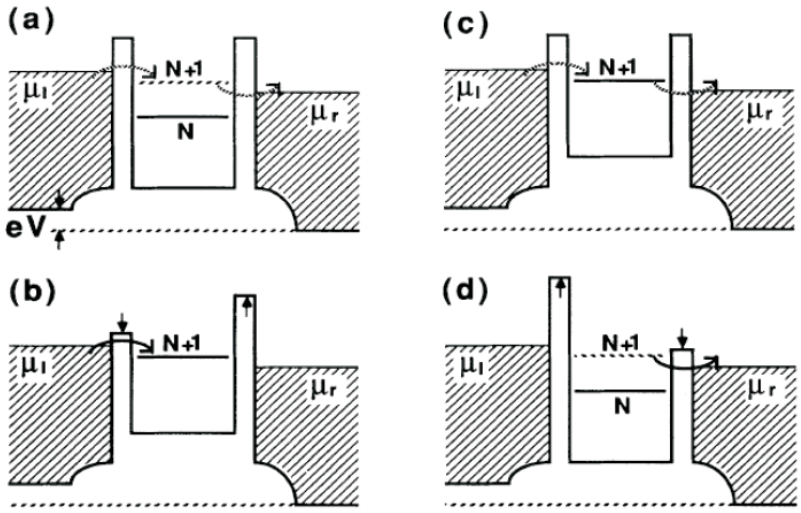

Figure 2.5: A schematic of the single electron turnstile. Taken from [33].

However, there is a limitation of these metallic turnstiles and pumps: the RF frequency applied cannot be very high (about tens of megahertz) because of the RC time-constant of the metal-oxide junctions. This will limit the total current to about 10 pA. However even better accuracy, a current of at least 100 pA with error rate less than 1 part in 10^7, is required to redefine the electrical standard. This means metallic turnstiles and pumps are not suitable to realise the quantum current standard.

High RF frequency that generates large pumping current can be achieved on semiconductor quantum dot devices because of the low RC constant. On these devices, metallic surface gates with negative voltage applied are used to confine the quantum dot. When RF voltage is applied to the tunnel barrier gates, the electrons will be transported through the dot periodically. Kouwenhoven *et al.* demonstrated the first

single-electron turnstile on GaAs/AlGaAs heterostructure in 1991 [33] and Fujiwara *et al.* first demonstrated a silicon single-electron turnstile generating 16 pA current in 2004 [34]. For gigahertz pumping, Blumenthal used a GaAs/AlGaAs tunable-barrier quantum dot electron pump to generate current 87.64 at the frequency 547 MHz. with an error rate of 100 ppm in 2007. Significant improvements has been made since the device first demonstrated by Blumenthal *et al.* in 2007 [2]: currently state of art error rates are 0.16 ppm at 600 MHz (96.1 pA) [7] and 0.3 ppm at 1 GHz (160.2 pA) [8]. However even better accuracy, a current of at least 100 pA with error rate less than 1 part in 10^7, is required to redefine the electrical standards. More details about the pumping mechanism are described in Chapter 6. Single-electron turnstiles and pumps have also been demonstrated based on graphene [35], hybrid normal-metal-superconductor structures [36] and carbon nanotubes [37].

Parallel pumping could increase the total output current and enable a higher accuracy current measurement [12, 13, 38]. Figure 2.6 shows two parallel pumps demonstrated by Wright *et al.* [38] and three parallel pumps demonstrated by Mirovsky *et al.* [12].

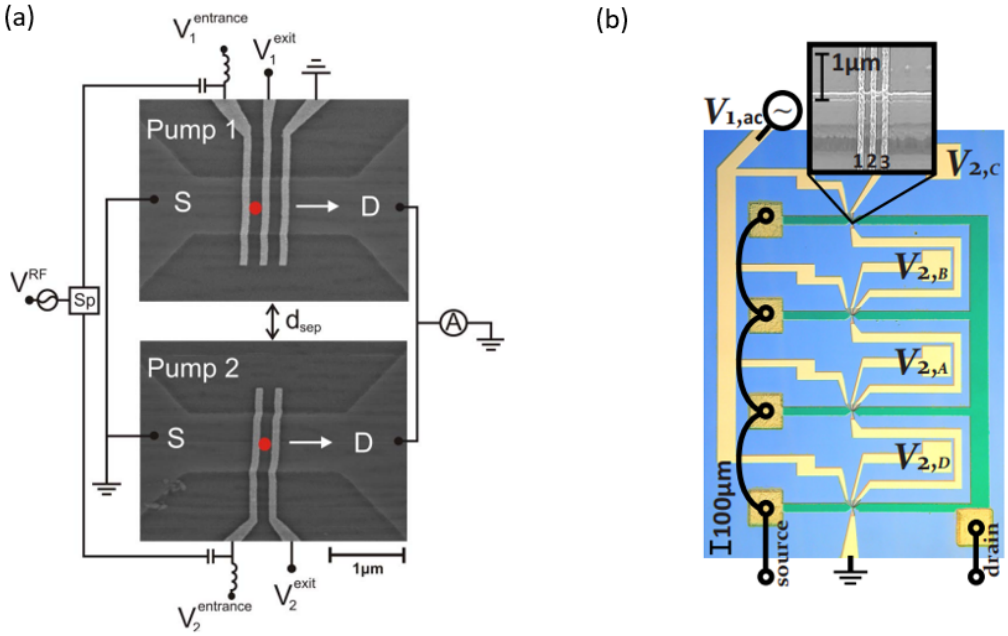

Figure 2.6: Parallel pumping. (a) Two parallel pumps demonstrated by Wright *et al.* Taken from [38]. (b) Three parallel pumps demonstrated by Mirovsky *et al.* Taken from [12].

Apart from the application in metrology, single-electron turnstiles and pumps can also be used as an on-demand emitter of single electrons. These turnstiles and pumps operate at high frequency, which are highly desirable for fast quantum information processing [39–41]. Besides, if the emitting electrons enter a p-type material and combine with holes, photons will be emitted. Therefore single-electron turnstiles and pumps are promising for acting as single-photon emitters [42, 43]. Electron pumps also can emit electrons into quantum Hall edge states, which act like waveguides. And 1D channels can be used like beam splitters to do experiments like the Hong-Ou Mandel test [44].

2.3 Quantum multiplexer

The cryogenic quantum multiplexer is an on-chip architecture using the limited number of available cryogenic measurement wires to increase the number of measurable devices on a single chip. This technique can be used to study the statistics of device fabrication yield, reproducibility and quantum effects. This section will introduce the theory, design and application of the quantum multiplexer.

In electronics, a multiplexer, commonly shortened to 'MUX', is a device selecting one signal among several input signals and forwarding the selected signal to the output line. The biggest advantage of the multiplexer is that within a certain time or bandwidth the multiplexer can increase the amount of data to be sent. In contrast, a demultiplexer is a circuit than can send an input signal to many output lines. Multiplexers and demultiplexers normally work in pairs. Figure 2.7 shows diagrams of a 2-to-1 multiplexer and 1-to-2 demultiplexer.

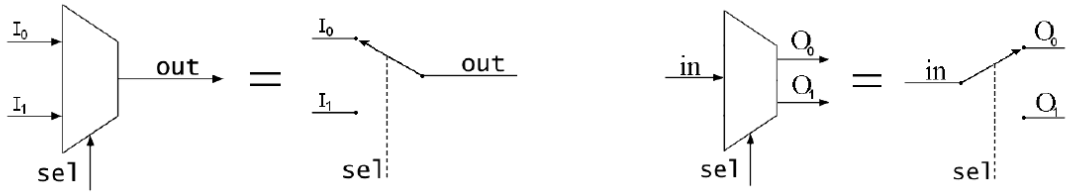

Figure 2.7: Schematic of multiplexer and demultiplexer.(a) 2-to-1 multiplexer. (b) 1-to-2 demultiplexer. Taken from [45].

The quantum multiplexer uses a similar principle, which can exponentially increase the number of electrical gates that can be contacted to different quantum devices such as split gates or single-electron pumps. The quantum multiplexer is able to measure

up to thousands of devices depending on the number of contacts on the chip carrier, which is hard to achieve without a multiplexer.

The quantum multiplexer studied in this thesis is a multilayer structure developed on a GaAs/AlGaAs heterostructure. Figure 2.8 (a) shows the schematic diagram of the quantum multiplexer structure. Figure 2.8 (b) describes how the multiplexer is controlled to transmit the input voltage V to the selected path 1. The mesa has a binary tree-like structure, and each level of the mesa is controlled by two addressing gates. There are six addressing gates (G1 to G6) to determine the path in this structure. When we want to pinch off one path, we need to apply some negative voltage (typically -0.3 V) to the corresponding addressing gate. The negative voltage should be large enough to pinch off the mesa path without polyimide, however, it should not be too large to pinch off the mesa path with polyimide insulator. In Fig. 2.8 (b) when -0.3 V is applied to the addressing gates G2, G4, G6, the mesa under the G2, G4, G6 gates without polyimide will be pinched off, therefore the input voltage V will reach path 1.

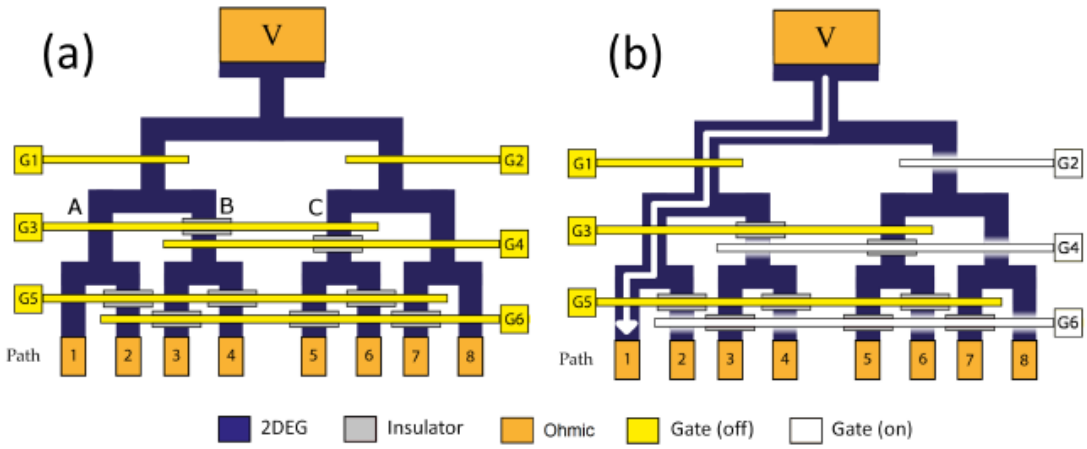

Figure 2.8: Schematic diagram of quantum multiplexer structure. (a) Schematic diagram of the multiplexer structure. (b) Negative voltage applied to the addressing gates G2, G4 and G6 to pinch off the other paths except path 1. Taken from [9].

If we have n contacts for the multiplexer structure, one contact is for the input V and the total number N_{MUX} of output paths the multiplexer is given by:

$$N_{\mathrm{MUX}} = 2^{(n-1)/2} \tag{2.8}$$

Since the quantum multiplexer was first introduced, many applications have been demonstrated [9, 10, 46–50]: for example, using the standard LCC chip carrier which has 20 contacts, 256 split-gate devices were measured in a single cool-down by Al-Taie

et al. [9]. Puddy *et al*. used multiplexed charge-locking system (Fig. 2.9) to measure the Coulomb-blockade peaks of a single quantum dot [11]. A statistical study of conductance properties in one-dimensional quantum wires focusing on the 0.7 anomaly using a multiplexer as presented by Smith *et al*. [10]. In summary, the quantum multiplexer is an architecture that can measure large numbers of devices using limited contacts on a chip in a single cool down. Our aim is to extend its applications to MUX single-electron pump arrays.

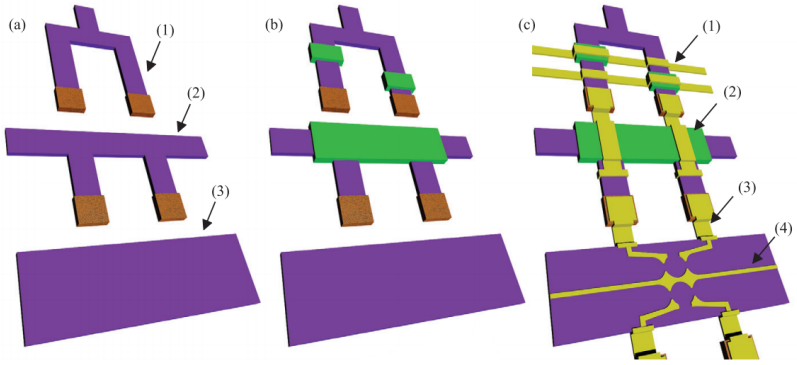

Figure 2.9: Schematic of charge-locking system based on the quantum multiplexer: more details are shown in [11]. Taken from [11].

2.4 Conclusion

This chapter has presented the background theory of low-dimensional semiconductor structures required to understand the work in the following chapters. Then we described how the single-electron pump promises to realise a quantum current standard, and presented a literature review of single-electron turnstiles and pumps. Finally, we have introduced the quantum multiplexer technique which can measure a large number of devices in a single cool-down.

3

Device Fabrication and Measurement Methods

This chapter presents the semiconductor processing techniques used to fabricate the devices and the measurement methods used in this thesis. Devices were designed with assistance from Dr Joanna Waldie (University of Cambridge), Dr Luke Smith (University of Cambridge), Dr Reuben Puddy (now at the University of Sussex) and Dr Patrick See (National Physical Laboratory). The single-electron pump devices with polyimide were fabricated by Dr Patrick See. Fabrication of devices has to be implemented in an orderly manner: etch a mesa, deposit ohmic contacts, e-beam patterned etch if necessary, e-beam gates evaporation if necessary, spin-on insulator, optical gates and bonding and device packaging.

In more detailed, the order of the fabrication steps is different for the different types of devices. For rectified current devices (see Fig 3.1) and MUX bar gates (see Fig 3.2) the order is mesa, ohmics deposition and annealing, EBL gates, polyimide, optical gates. For the pump with polyimide devices the order is optical mesa, ohmics deposition, EBL etch, ohmics annealing, EBL gates, polyimide, optical gates. We also tried doing the EBL gates after the polyimide and the optical gates (see Fig 3.3).

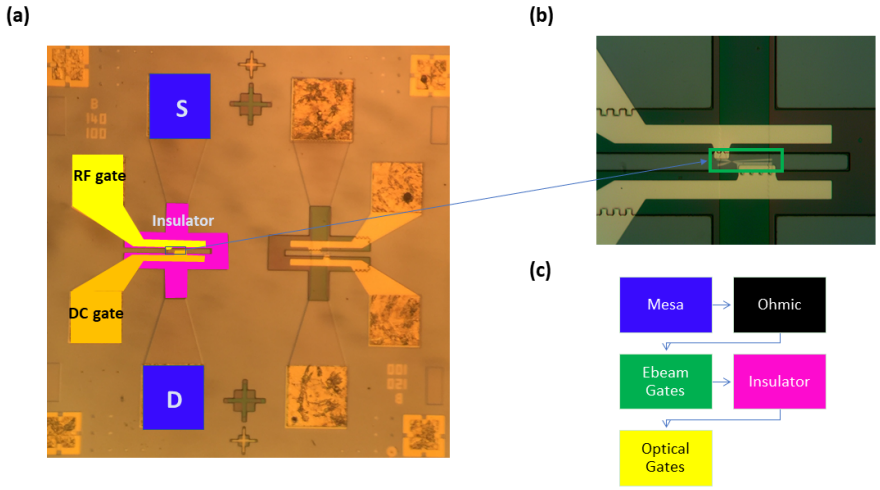

Figure 3.1: Device layout for wide-channel electron pump device. (a) Optical image. (b) The optical image of the e-beam gates area. (c) Fabrication order.

3.1 Wafer selection and preparation

The semiconductor material used for the devices is the high-electron-mobility transistor HEMT GaAs/AlGaAs structure grown on a (100) GaAs substrate by Molecular Beam Epitaxy at the Cavendish Laboratory by Dr Ian Farrer and Dr Christine Nicoll. These wafers contain a 2DEG 90 nm below the surface, which forms due to a narrow potential well in the conduction band profile in the z-direction between the GaAs and AlGaAs layers. Figure 3.4 is a schematic of the wafer we used to fabricate devices. We select wafers whose 2DEG has an electron density in excess of 1.5×10^{11} cm^{-2} and mobility greater than 10^6 cm^{2}V^{-1}s^{-1}. Three wafers are used for this work: W0261 is used for MUX bar devices; W0546 is used for rectified current devices and W1077 is used for single-electron pumps with polyimide (W0261 and W1077 wafers were grown by Dr Ian Farrer and W0546 by Dr Christine Nicoll). Their characteristics at 1.5 K are listed in Table 3.1. Here n_s is the sheet carrier density of the 2DEG and μ_s is the electron mobility.

The selected wafer is cleaved into rectangular chips using a diamond scribe. On each chip an array of several devices (usually 2×3) can be pattered. These devices are only separated from each other just before bonding. During scribing of the wafer, we orientate the wafer to make the etched channel can be patterned parallel to the $[01\bar{1}]$ crystallographic direction to enhance the mobility. Before processing, chips are usually

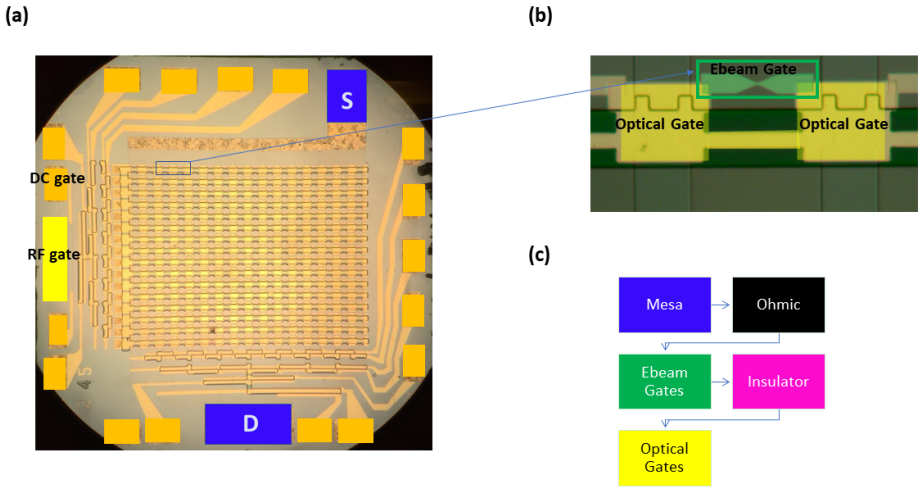

Figure 3.2: Device layout for MUX bar devices. (a) Optical image of MUX bar devices. (b) The optical image of the e-beam gates area. (c) Fabrication order of MUX bar devices.

Table 3.1: 2DEG assessment characteristics at 1.5K for HEMT wafers used in this work. 'Dark' is without any illumination. 'Light' is measured after the cooled device has been illuminated for 180 s with a red LED.

Wafer I.D.	n_s in dark $[m^{-2}]$	n_s in light $[m^{-2}]$	μ_s in dark $[m^2/Vs]$	μ_s in light $[m^2/Vs]$
W0261	1.894×10^{11}	3.482×10^{11}	2.091×10^{6}	4.52×10^{6}
W0546	1.722×10^{11}	3.272×10^{11}	1.36×10^{6}	2.956×10^{6}
W1077	2.022×10^{11}	3.575×10^{11}	2.655×10^{6}	4.752×10^{6}

put in a beaker of Acetone in an ultrasonic bath for 2 minutes, cleaned in Acetone, rinsed in IPA and then dried in N_2 gas.

3.2 Mesa Fabrication

Optical photolithography is used to pattern the features that are larger than 10 μm. Single electron pump with polyimide devices needed to be etched in two stages: large features patterned by optical photolithography and small features by electron-beam lithography (EBL). For wide-channel pumps and MUX bar devices, the mesa is patterned using just optical photolithography.

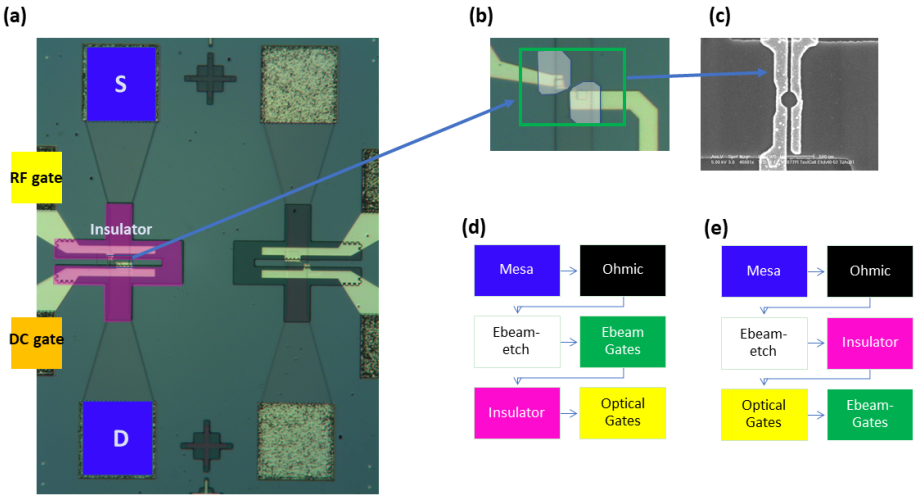

Figure 3.3: Device layout for single electron pump with polyimide devices. (a) Optical image of single electron pump with polyimide devices. (b) The optical image of the e-beam etching area. (c) The optical image of the e-beam gates area. (d) Fabrication order of part of single electron pump with polyimide devices. (e) Fabrication order of the other part of single electron pump with polyimide devices.

3.2.1 Optical lithography etch

Firstly, Shipley Microposit 1813 was spun onto the surface of the chip at 5500 rpm for 30 s to give resist thickness about 1.3 μm. Then the chip was baked at 115°C for 60s to harden the photoresist and bake out the solvent.

The chip was subsequently exposed to UV radiation for 6.5 s at power of 350 W in an optical mask aligner. The glass mask with the mesa pattern was fixed into the optical aligner above the chip. Then a controlled amount of ultra violet radiation was used to expose the photo-resist outside of the mesa.

The exposed photo-resist was dissolved away by placing the chip in MF319 developer for 40s. Then the chips are washed in de-ionised (DI) water and dried in N_2 gas. In this way, the mesa pattern, which is defined by the regions of leftover photo resist, has been transposed from the mask to the surface of the chip.

To etch the wafer to the required depth (the ideal etch depth is 110-120 nm, if the etch is deeper then the metal gates deposited later may not climb continuously up the mesa sidewalls easily). The height of the photoresist was measured using a Dektak surface profiler. The chips are dipped in a solution of 10% HCl for 30 s, to remove the surface oxide and any remain photo-resist in the exposed area, then rinsed in DI water.

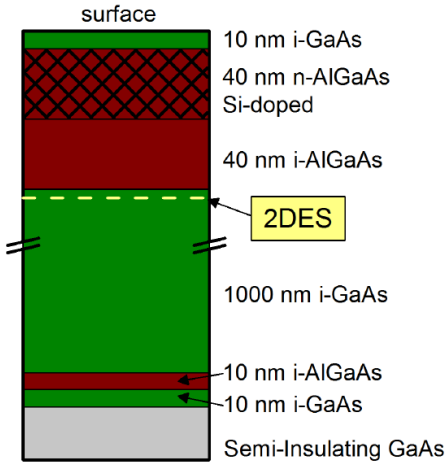

Figure 3.4: A schematic diagram of the cross section of the GaAs/AlGaAs heterostructure wafers used to fabricate rectified current devices, mux bar gate devices and single electron pump with polyimide devices. Adapted from [15].

Then the chip was placed in a solution of 1:8:120 H_2SO_4 : H_2O_2 : H_2O for about 15 seconds. The chip was subsequently rinsed in a weir of flowing DI water. The chip was measured again to get the required depth (etch again if necessary). The remaining photoresist is removed from the surface of the chip by cleaning in Acetone and IPA and drying in N_2 gas. Figure 3.5 (a) to (d) shows a schematic illustration of the etching process.

3.2.2 EBL-pattern etch

The electron beam lithography (EBL) in this work was done by Jon Griffiths and Tom Mitchell, at the Cavendish Lab. For the single-electron pump with polyimide, in the centre the mesa narrows to a 2-μm-wide channel, which needs to be patterned by EBL. The Leica EBL machine in the SP Group was used to pattern a thin layer of acrylic known as polymethy-methacrylate (PMMA)-based resist.

The PMMA (A4 950k) is spun onto the surface of the chip in a similar way to the photo-resist. PMMA (A4 950k) is spun onto the chips at 3000 rpm to give a thickness of about 400 nm. Then the chip was placed in an oven and baked at 150°C for 50 mins to harden the PMMA and bake out the solvents. The areas to be etched are exposed to an electron beam to breaking the PMMA. Then the PMMA is developed in a solution of 1:5:15 methyl-ethyl-ketone(MEK):methy-isobutyl-ketone(MIBK):IPA for 8-9 s, then chip is rinsed in IPA for 60 s and dried in N_2 gas.

Before etching the narrow channel, the chip was dipped in 10% HCl for 30 s to remove any oxides and rinsed in DI water for a few seconds. The etching solution is 1:8:1600 $H_2SO_4 : H_2O_2 : H_2O$. As the EBL-patterned gates need to run continuously up the sidewall of the etch, the etch must be relatively shallow. From the fabrication experience of Dr Patrick See and others, etching 30-40 nm is sufficient to prevent the 2DEG conducting [24, 51]. An atomic force microscope (AFM) was used to determine the etch rate of the solution using several test chips (the time calibrated is usually around 70 to 80 s). The chips are washed in DI water and dried in N_2 gas after etching. The PMMA was removed from the surface of the chip in Acetone, rinsing in IPA, and drying with N_2 gas.

3.3 Ohmic contacts

A contact between a metal and a semiconductor which has a low resistance, linear current-voltage (I-V) characteristic that obeys Ohm's law is called an ohmic contact.

To realize ohmic contacts, firstly S1813 is spun on the chip and baked at 90°C for 1 minute. Then the chip is exposed to UV radiation for 6.5 s at a power of 350 W in an optical mask aligner. After that the chip is submerged in chlorobenzene (C_6H_5Cl) for 3 minutes to harden the unexposed resist, which can make the removal of unwanted metal in the lift-off procedure easier. Then the chip is developed in MF319 for at least 1 minute. The chip should be etched with a RF plasma asher for 45 seconds to remove any residual resist on the ohmic targets before evaporation. Ashing is a process where organic matter is removed using oxygen plasma. As the device has been exposed to oxygen, the chip then needs to be immersed in the 20 % HCl solution for 30 seconds and dried with dry N_2 gas to remove the oxide layer.

To get ohmic contacts, a ∼150 nm thick gold-germanium-nickel (AuGeNi) layer is deposited in a thermal evaporator in a low-pressure (2×10^{-6} mbar) environment. Then we remove the resist to lift off the metal using acetone to leave the patterned ohmic contacts on the chip. The samples are annealed at 430C for 80 s in a rapid thermal annealer. The expected measured resistance of the devices should be less than 40 kΩ at room temperature and less than 10 kΩ at liquid nitrogen temperature (77 K). The process of depositing Ohmic contacts is shown in Fig 3.5 (e) to (h).

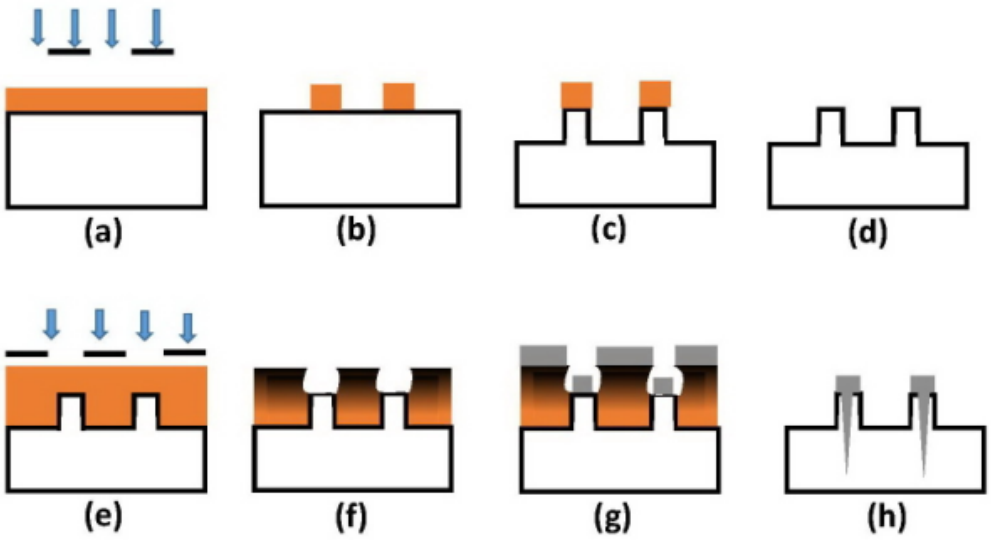

Figure 3.5: Illustration of fabrication processes. (a) to (d) Mesa etching. (e) to (h) Ohmic contact deposition. Adapted from [9].

3.4 Insulators deposition

Polyimide is an organic polymer which can be spun on to the chip and then cured to remove solvents, leaving a solid insulating film, which has high thermal stability and chemical resistivity. At the Cavendish Lab, we use polyimide coatings consisting of HD Microsystems HD4104 polyimide and T9039 (2:1) as an insulator between the leads and the mesa. As water-polymer interaction may impair the insulating effect, the device needs to be baked at 125°C for 3 minutes to remove any moisture on the sample surface and also to strenghten the polyimide adhesion. By flushing the spinner cabinet with N_2, the humidity of the spinner enviroment is controlled to be dry and have less than 50% humidity.

In the spinning step, the rotation speed is first set at 5000 rpm for 50 seconds and then gradually increased to 7500 rpm within the first 10 seconds. Then we bake the sample at 65 °C for 120 seconds, 90 °C for 180 seconds and expose to UV radiation for 70 seconds. Subsequently we wait for at least 5 minutes and bake again at 80°C for 1 minute. Next is the developing step: the sample is put into HD Microsystems PA401D developer for about 15 seconds to dissolve the unexposed polyimide, and then rinsed in PA400R solution. Afterwards RF ashing is utilized for 120 seconds to remove the

residual unexposed polyimide. The last step is curing which is baking the sample in a temperature-controlled oven in inert N_2. The oven temperature ramps up slowly to 270 °C for 60 minutes and then decreases slowly to room temperature.

3.5 Surface gate deposition

Nanometre-scale gate patterns were written by EBL after the ohmic-contact deposition. The EBL defined gates are metal right on top of the surface of the chip (not on top of the insulator). The large-scale gates like the multiplexer addressers and the leads from the EBL-defined gates to the bond pads defined by optical lithography were made to contact the EBL-defined gates by overlapping them.

3.5.1 Optically-patterned gates

Optical photolithography is used to pattern features larger than a few micrometers. Here we use a two-layer resist process: In order to achieve a more robust deposition and lift-off of unwanted metal, Lift-Off Resist (LOR 7B) is initially spun onto the chip at 3000 rpm for 50 seconds, followed by a 10 minute bake at 175℃. Then a standard positive resist (Shipley 1805) is spun on it at 5500 rpm for 30 seconds and baked at 115℃ for 1 minute to create an undercut profile. The dual-layer resist results in a steep undercut in the developed parts and reliable lift off. The gates pattern is exposed to UV radiation for 3.5 s at 350W and developed in MF319 developer. Then the sample is mounted on a rotating stage angled at 45° to the horizontal in the thermal evaporator to make sure the metal is continuous over the mesa and insulator regions. Typically a 10/100 nm titianium/gold (Ti/Au) multi-layer is deposited at low-pressure which is ideally about 2×10^{-7} mbar for large metal gate contacts. Here gold is used for low-resistance bonding and Titanium acts as 'wetting layer' for good adhesion to the wafer. After the evaporation, we lift-off the resist and unwanted metal using hot SVC-14 photoresist stripper (about 50 $°C$). Figure 3.5 (e) to (g) shows the schematic illustration of the lift off process.

3.5.2 EBL-patterned gates

EBL is used to pattern the nanometre-scale features which can confine the electrons to zero dimensions by forming QDs. We use a two-layer PMMA-based resist to ensure good lift-off of unwanted metal after deposition. Firstly, a solution of 1:1 PMMA (A6 100k):anisole is spun at 5000 rpm for 60 seconds to give a thickness of about 100 nm,

then baked in a 150°C oven for 15 minutes. Secondly, a solution of 5:1 PMMA (A11 950k):MIBK is spun at 7000 rpm to give a thickness of of about 40 nm, then baked at 150°C for 15 minutes.

The chips are subsequently sent to the e-beam suite to write the desired patterns. After exposure, the PMMA is developed for 8-9 in 1:5:15 MEK:MIBK:IPA, then the chips are rinsed in IPA for 60s and dried in N_2 gas. Then the layers of metal were evaporated in the same way as the optical gates, except that the thickness of the metals here is 81 nm in total. To ensure successful lift-off, the gates must be thin. After lift-off overnight in Acetone, the metal on the surface of the PMMA is removed. As the film-thickness monitor inside the evaporator is not sufficiently precise for these small thickness, we use the AFM to find the actual thickness of metal deposited by calibrating using test chips.

After the deposition, to reduce any ageing due to oxidation, we often spin a layer of PMMA onto the surface at 3000 rpm for 50s and bake it at 150°C for about one hour, which acts as a protective coating on the surface of the devices.

3.6 Wire bonding

Once all the required patterns have been etched or patterned, the chips are ready to be cleaved into individual devices. The protective PMMA was removed by submerging the device in acetone. The acetone was then washed away with IPA and the device was dried with N_2 gas.

Next, the device needs to be bonded and packaged in order to perform cryogenic measurements. The devices are glued to the sample holders using GE varnish. To prevent the ESD damage, we use a wedge bonder rather than a ball bonder to connect the ohmic contacts and gates to the electrical connections on the sample holder. As the devices are very sensitive to ESD damage, when we are bonding the devices, we always keep the bonder, user and any tweezers connected to the same ground potential.

3.7 Low-temperature measurements

3.7.1 4 K ^{4}He dip station

Measurements must be performed at very low temperatures to study quantum transport, which ensures that the electron pumping or other quantum effects can be observed. All the measurements in this work, including the rectified current, multiplexer bar gates,

and single-electron pump with polyimide measurements are performed in a ^{4}He dip station. Only the 4 x 32 multiplexed wide-channel pump devices were measured at lower temperature in a dilution fridge.

We use a custom-made PCB sample holder [see Fig. 3.6(b)], which has a 21-way dc connector and two SMP connections for RF signals to measure the devices. Figure 3.6(a) shows the basic room-temperature measurement electronics for mux bar-gate devices. The dc voltages were applied to the gates using Stanford Research systems SIM928 isolated voltage sources. The current coming out of the device was amplified using a Femto DDPCA-300 current-to-voltage (I-V) converter. When we do differential conductance measurements with a lock-in amplifier using an ac voltage bias, a gain of 10^6 V/A was used. When we do dc current measurements, a gain of 10^{10} V/A was used. We use a lock-in detection technique to measure the differential conductance ($G = dI/dV$) to characterise the devices initially and then do the AC measurements or DC measurements as required.

3.7.2 Electrostatic discharge precautions

The EBL-patterned gates are vulnerable to damage during fabrication and measurement. And electrostatic discharge (ESD), which is a sudden flow of electricity from a charged object to the device resulting in sparking and dielectric breakdown, is one common cause.

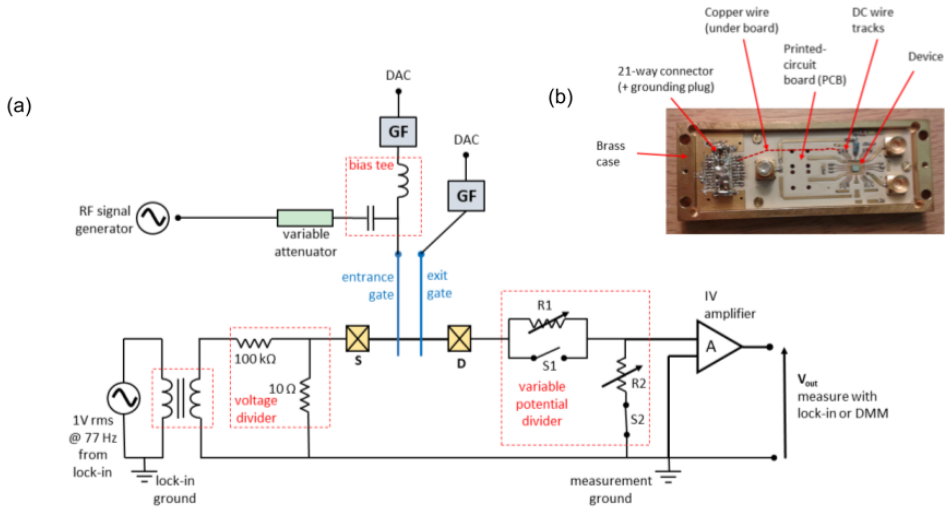

Figure 3.6: Electrical circuit for measurement set up. (a) Schematic of the measurement circuits. (b) The sample holder, GF is the gate filter. Adapted from [15].

We take the following precautions to protect the devices from the ESD damage: we use the ultrasonic wedge bonder instead of a ball bonder for bonding the device. After bonding, the devices were always transported in conducting, anti-static sample boxes. The grounding wrist straps were always worn when bonding, handing devices or performing electrical measurements. All the instruments connected to the device are powered through a uninterruptible power supply (UPS). The UPS also smooths out spikes in the power supply. The instrument rack/shelves are gounded by connecting them to the case of one of the instruments. We use the rack to ground ourselves (by the wrist strap) and the dewar. A shorting plug is fitted to the 21-way dc connector which connects to the gates and ohmic contacts to keep the same potential as the brass case of the sample holder except when measuring. We also use a variable attenuator to connect the inner conductor to the outer conductor of the RF cable going to the bias tee when we are not applying an RF signal. When we were doing the pumping measurement, we needed switch the gain of the amplifier from 10^6 V/A to 10^{10} V/A. During this gain changing process, the DDPCA-300 can send a voltage spike to the device which could damage this device. To solve this problem, a variable potential divider designed by Dr Masaya Kataoka (NPL) was added between the device and the amplifier. The electrical circuit for the measurement set up is shown is Fig 3.6(a).

As the devices are most sensitive to the ESD damage at low temperatures, therefore we always configure the set up for electrical measurements at room temperature before cooling down.

3.8 Summary

This chapter presented the clean-room processing techniques we use to fabricate devices in this work. Also, the low temperature measurement set-up and how the devices are protected from electrostatic discharge damage has been discussed.

4

Wide-channel electron pumps and rectified current

Most semiconductor electron pumps are based on narrow etched wires (a few microns wide or less). As we aim to achieve multiplexed electron pumps, a big problem is that the narrow channel can become non-conducting at low temperature due to ESD damage, which might be because the surface states on the channel side walls become charged up. The channel could also become non-conducting if there is a semiconductor defect in the channel. This is a big problem for the multiplexed electron pumps sample, because one non-conducting channel means we will lose the whole column (row) of electron pump devices. As a way to remove this problem, we could use wide-channel devices to improve yield and also save an e-beam step (patterning the narrow channel etch) in the fabrication process. Also, the device fabrication is a lot easier without having to etch the narrow channel, because if we etch the narrow channel then the thin e-beam gates (about 50 nm wide) have to climb up the sidewall, which is difficult to achieve without the metal breaking. However, instead of showing a pumping current, these wide-channel devices introduced an interesting issue: they produced a DC current much bigger than the expected pumping current. An example of this current is shown as a function of the entrance and exit gate voltages in Fig. 4.1. The peak current here

is about 100 μA, but the expected pump current $e \times f$ (here e is the electron charge) at this frequency is only about 18 pA. As this is a DC current generated by an AC voltage, we call it rectified current.

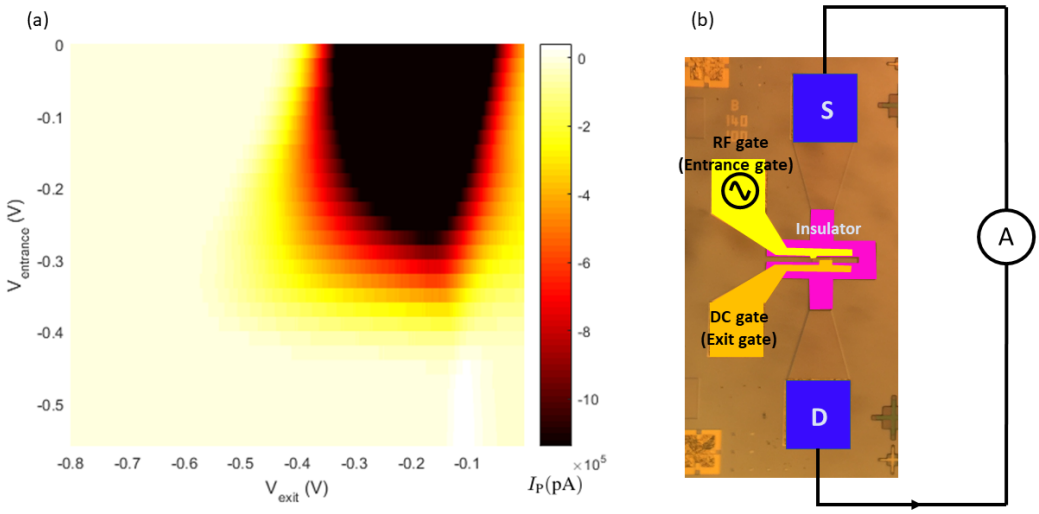

Figure 4.1: (a) A typical colourmap of rectified current vs exit gate voltage and entrance gate voltage with 110 MHz, -5 dBm RF signal applied to the entrance gate. (b) A schematic of the measurement circuit.

Rectified current has been seen in many previous studies. The rectified current is small in narrow-wire pumps and is much larger in wide-channel pump devices and standard top-gated Hall bars. Giblin *et al.* 2012 [3] researched rectified current in pump devices, and showed that it occurs because the RF signal on the entrance gate is parasitically capacitively coupled to the 2DEG. He suggested that the asymmetric pick-up on the source and the drain 2DEG generates the rectified current. The electron pumps used by Giblin *etal.* are narrow-channel pump devices and the rectified current is only 1 part in 10^{12} of the pumped current. However, in our devices the rectified current is much larger which swamps any single electron features. Howe *et al.* [52] also researched the rectified current, but he only studied a Hall-bar device with a single gate, which is simpler than the wide-channel electron pump device.

Here we want to research the origin of the rectified current in wide-channel electron pump devices so that we can suppress it to observe pumping current. In this chapter, I present our results from a 4 x 32 multiplexed wide-channel electron pump array and single wide-channel-electron pump devices. Then we develop a model to explain the rectified current in the wide-channel electron-pump device and investigate the

effects of changing the RF frequency, RF amplitude, entrance-gate voltage and DC bias connected between the source and drain.

4.1 4 x 32 multiplexed wide-channel electron pump array

We designed a 4 x 32 multiplexed wide-channel electron pump array using wide channels (shown in Fig. 4.2). These devices were tested in a Bluefors dilution refrigerator at about 30 mK. However, instead of observing a pumping current, we just observed a large rectified current, which was much bigger than the expected pumping current. Figure 4.3 shows the comparison of the current colourmap between no RF and 100 MHz -18 dBm RF applied on the RF gate. The coloured area is the positive current running from the source to the drain. The black area is negative current. We can learn from Fig. 4.3 (a) that with no RF signal applied at V_{exit} = 0 V, 100 nA positive current flows because of the small voltage offset on the current amplifier input terminal. This current is decreasing as more negative voltage V_{exit} is applied and is pinched off for $V_{exit} \approx$ -0.26 V. As the entrance gate does not run across the whole channel (Fig. 4.2 (b)), the entrance gate voltage has almost no effect. From Fig. 4.3 (b) when the RF signal is applied to the entrance gate, there is additional current flowing close to the pinch off voltage of V_{exit}, and the current can be positive or negative depending on the entrance gate voltage $V_{entrance}$. This current is rectified current.

Having observed this behaviour, we want to know whether it is the multiplexer that causes the problem of rectified current or whether it is just the wide-channel electron pump causing the problem. The following measurements were designed to see if we control observe a pumping current in a wide-channel pump design without a multiplexer. If yes then the rectified current could be because of the multiplexer. If not then the wide-channel electron pump design itself could be the cause of the problem and maybe we should use a narrow-channel design for the next steps of developing multiplexed electron pump arrays.

4.2 Single wide-channel electron pump device

We designed and fabricated several sets of wide-channel devices to analyse the effects of changing parameters such as amplitude, frequency and the design of the entrance and exit gates. The design of these devices is shown in Fig. 4.4. The measurement

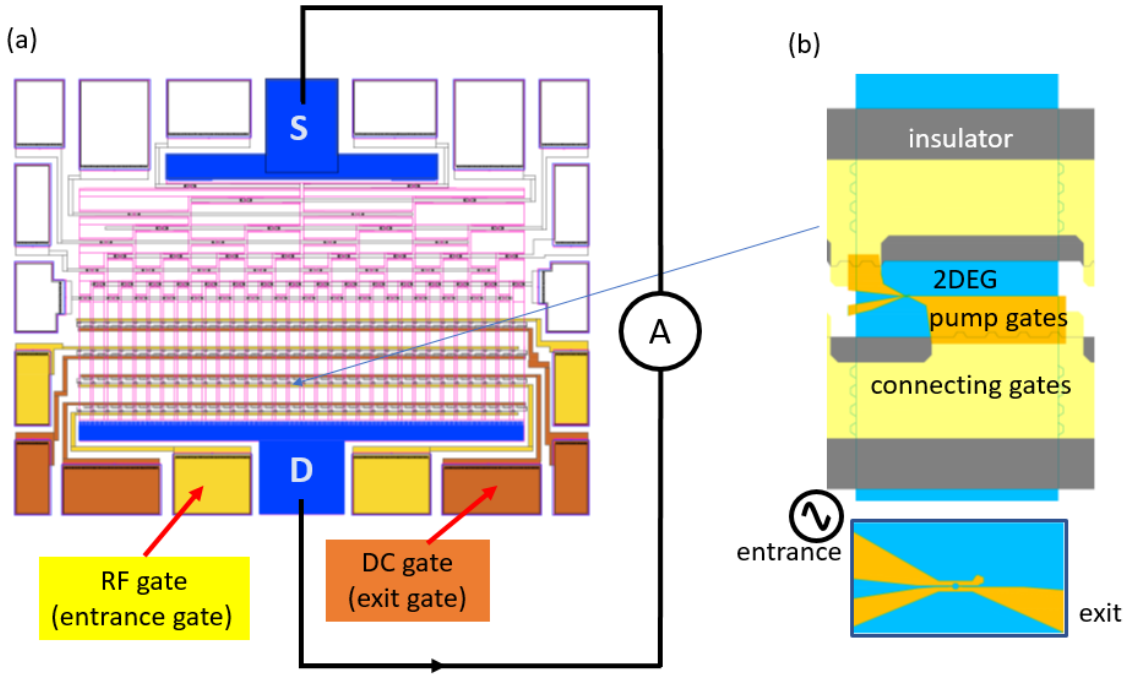

Figure 4.2: A schematic of the 4 x 32 multiplexed wide-channel electron pump array design. (a) The optical mask design. (b) A zoomed in version of the e-beam gates area. The blue is the 2DEG mesa, the yellow parts are the optical gates, the orange parts are the ebeam gates, the grey is the polyimide layer.

setup we use to measure wide-channel electron pump devices is shown in Fig. 4.5. We added some ESD protections such as adjustable dividers and attenuators to protect the devices from voltage spikes; full details are given in the Methods chapter 3. All our devices are fabricated using W0546 GaAs/AlGaAs HEMT wafer. All the measurements were carried out at 4K.

The entrance gate was driven by a sinusoidal signal from an RF source. The output of the RF generator was added to a DC bias and applied to the gate through a room temperature bias-tee. The exit gate was connected to a DC voltage source. The drain lead was connected to a current-to-voltage amplifier. The output of this amplifier was measured by a digital multimeter or a lock-in amplifier.

For each device, firstly we need to make sure the device conducts well both at room temperature and at 4 K. For this the lock-in amplifier is used to measure the low-frequency AC conductance while we are sweeping the gate voltages. After that, we apply an RF signal to the entrance gate and sweep the exit gate voltage from 0 V to -0.8 V for different entrance-gate voltages from 0 V to -0.57 V. The DC current output was measured by the current-to-voltage amplifier with the digital multimeter. Typical

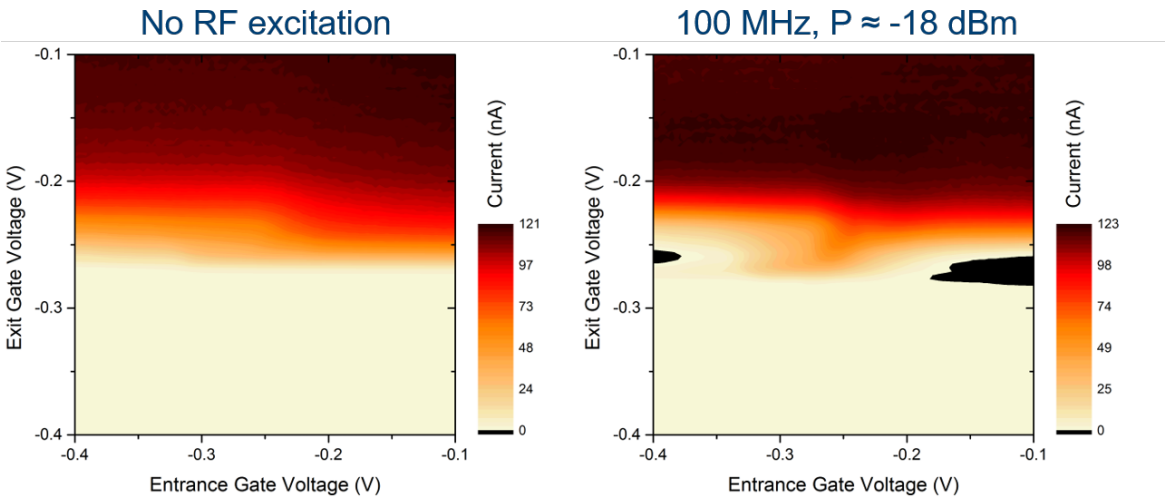

Figure 4.3: Measurement results of the 4 x 32 multiplexed wide-channel electron pump array. (a) The current colourmap of one single pump in the array when no RF excitation is applied. (b) The current colourmap of the same pump when 100 MHz -18 dBm RF is applied. The power applied here is limited by the wiring of the dilution fridge. This figure is drawn by Dr Joanna Waldie.

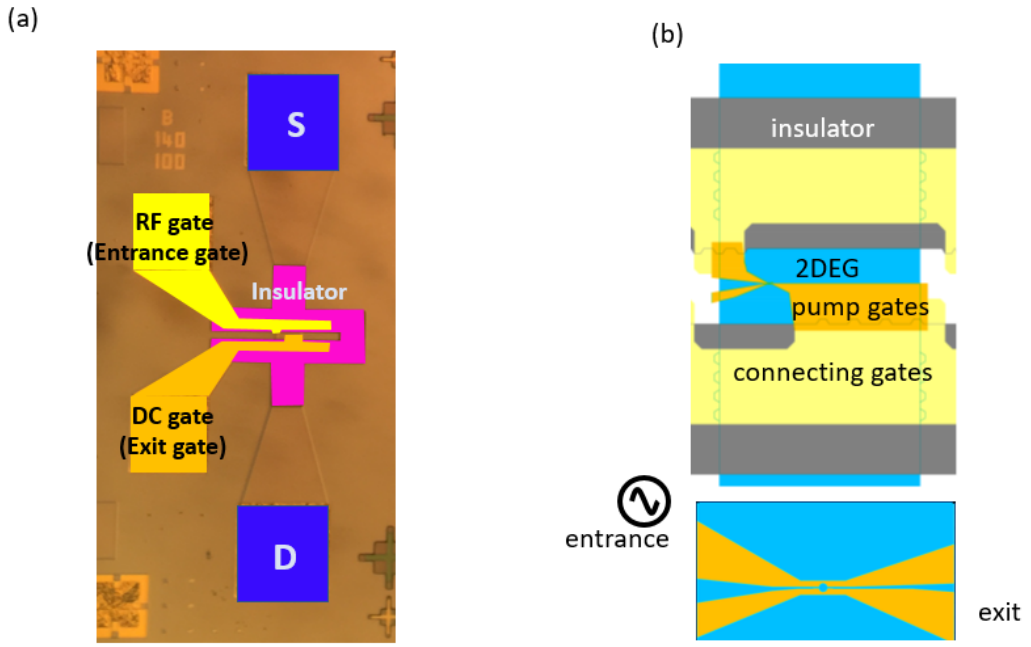

Figure 4.4: A schematic of the-wide channel pump design. (a) The optical microscope image of a device with polyimide, Pattern B. (b) A zoomed in version of the e-beam gates area. The blue is the 2DEG mesa, the yellow part is the optical gate, the orange part is the ebeam gate.

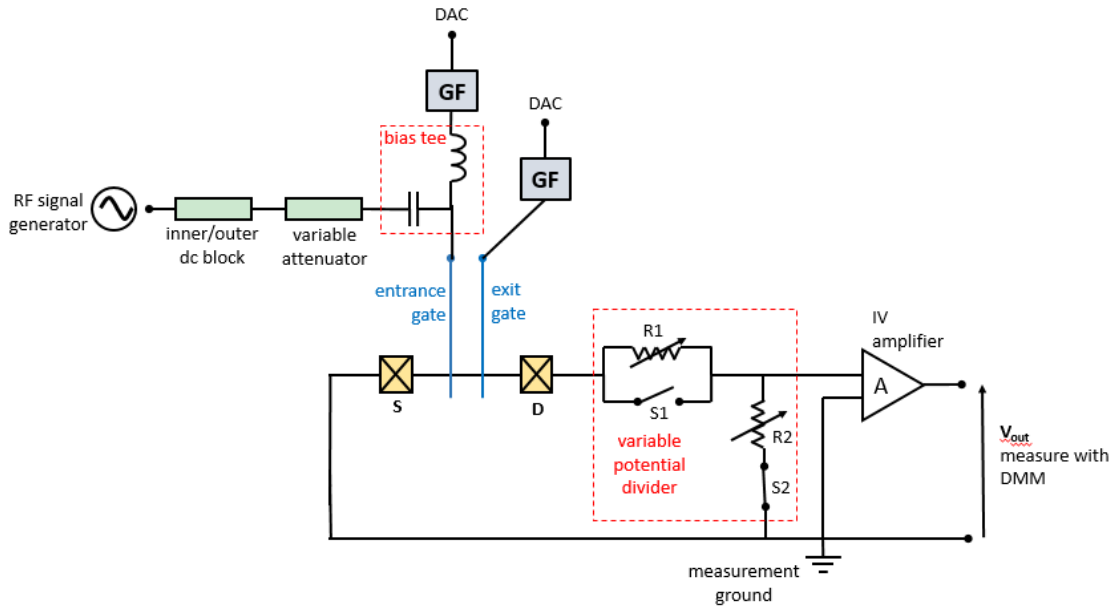

Figure 4.5: A schematic of the measurement setup for wide-channel electron pump devices.

pinch off curves are shown in Fig 4.6. Finally, we vary the power and frequency of the RF signal to study how the amplitude and frequency of the RF signal affect the rectified current.

4.3 Results: measurements of different e-beam patterns of wide-channel electron pumps

The devices we have can be divided into two types, which are devices with polyimide (these devices have the same gate geometry as the pumps in the multiplexed electron pump device) and devices which do not have polyimide.

Both kinds of device have four e-beam designs. For the devices without polyimide, Pattern A is the same design that was on the multiplexed wide-channel pump arrays. In Pattern B we make the entrance gate run all the way across the wide channel. In Pattern C we make the gap between the entrance gate and exit gate near the edge of the channel much smaller in case electrons are being trapped in this region. In the Pattern E designs we move the entrance gate and exit gate further apart (by about 7 μm), to see if this will still produce the rectified current.

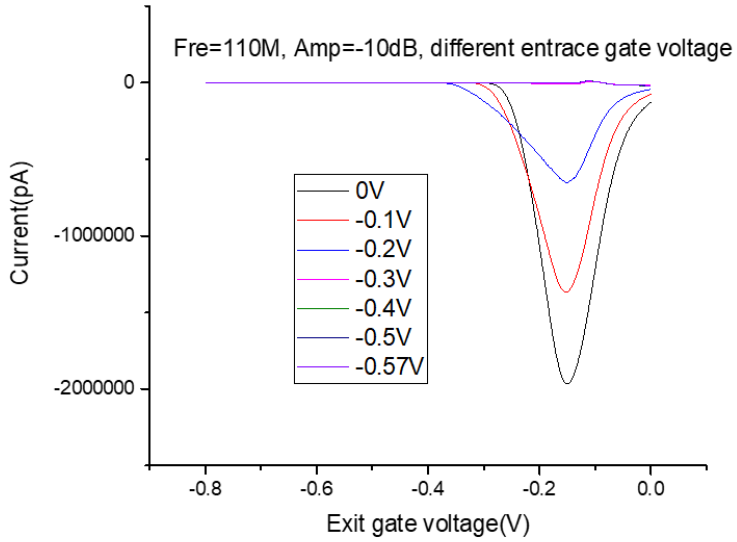

Figure 4.6: Typical plot of current vs gate voltage showing the typical pinch off curves with rectified current. 110 MHz, -10 dBm RF signal is applied and entrance gate voltage is 0V (black), -0.1V (red), -0.2V (blue) and -0.3V or less (other traces).

For the devices with polyimide, Patterns A are very similar to those devices without polyimide. In the devices with polyimide there are connection gates going all the way across the channel on top of polyimide, as in the MUX devices. In the devices without polyimide we do not have this. We also measured a device which has a smaller RF gate, to decrease the capacitance between the gate and the 2DEG to reduce the RF coupling.

We never observed pumping current in these devices, even with RF powers up to -2 dBm (which was sufficient to give pumping in the narrow-channel pumps we present in Chapter 6). Instead we observe rectified current which is much bigger than expected pumping current. Figure 4.7 to 4.11 show typical rectified current colourmaps for devices of each pattern. The measurement results for the devices with polyimide are similar to the devices without polyimide, so here we only present results for a Pattern A device with polyimide in Fig 4.12. For all these devices the rectified current colormaps all look similar: the biggest rectified current happens near the exit gate pinch-off voltage; the rectified current is small with small negative voltage applied to the exit gate; with large negative voltage applied to the entrance gate (even for pattern A and pattern C whose entrance gates do not reach across the channel) the rectified current disappears.

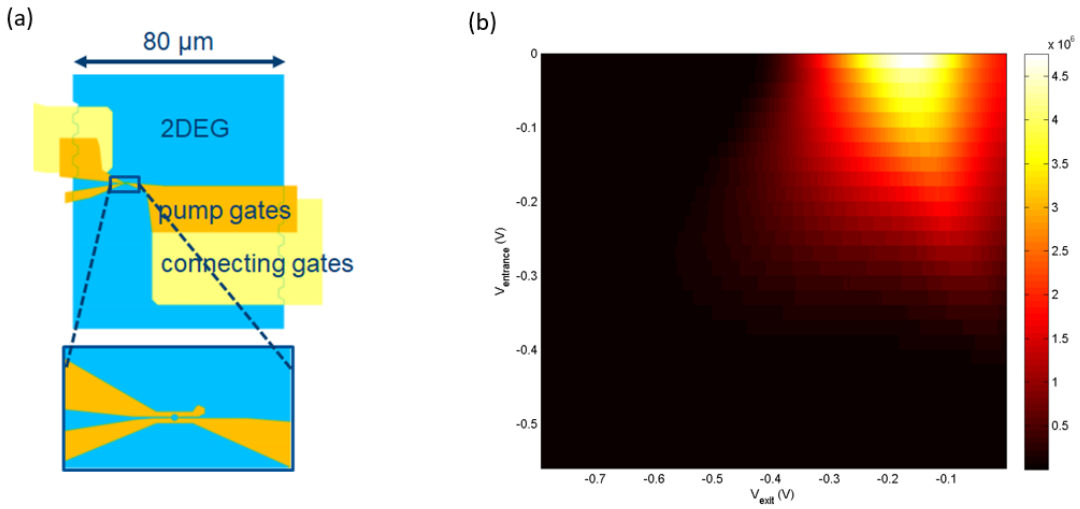

Figure 4.7: Device without polyimide, Pattern A. (a) Device layout. (b) The current colourmap of the current as a function of entrance and exit gate voltage with 110 MHz -5 dBm RF applied to the entrance gate; the unit for current is pA.

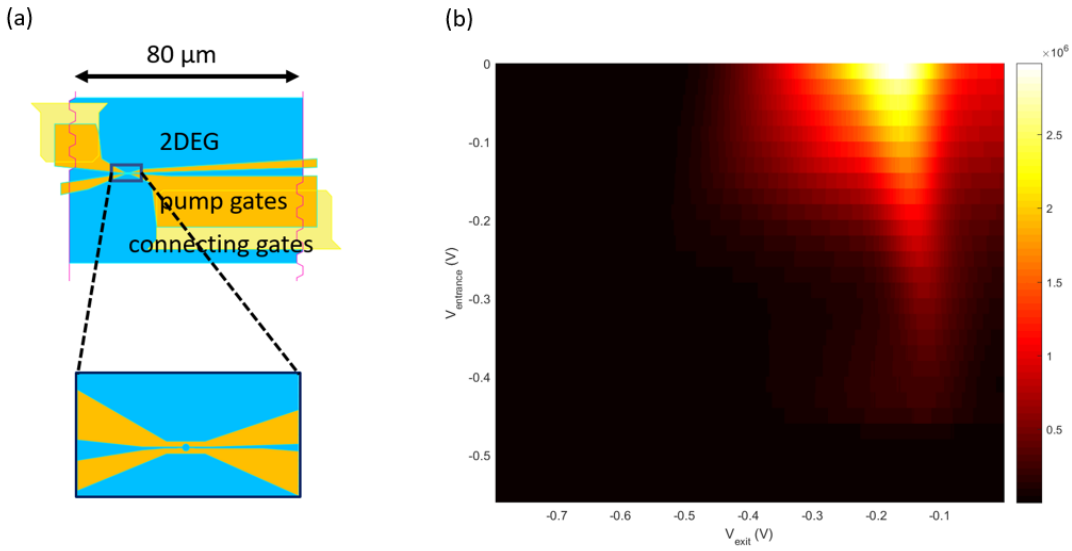

Figure 4.8: Device without polyimide, Pattern B. (a) Device layout. (b) The current colourmap of the current as a function of entrance and exit gate voltage with 110 MHz -5 dBm RF applied to the entrance gate; the unit for current is pA.

From the measurements of Pattern A and Pattern C, we find that the entrance gate does not have to go all the way across the channel to give the rectified current. From Patterns Ei and Eii, we learnt that the rectified current happens no matter how

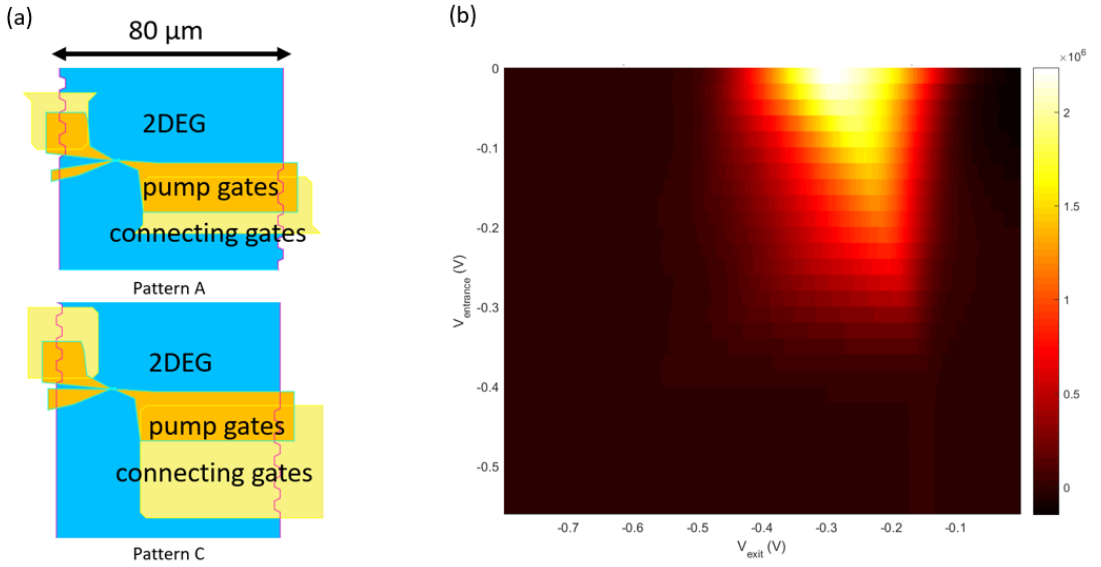

Figure 4.9: Device without polyimide, Pattern C. (a) Device layout. (b) The current colourmap of the current as a function of entrance and exit gate voltage with 110 MHz -5 dBm RF applied to the entrance gate; the unit for current is pA.

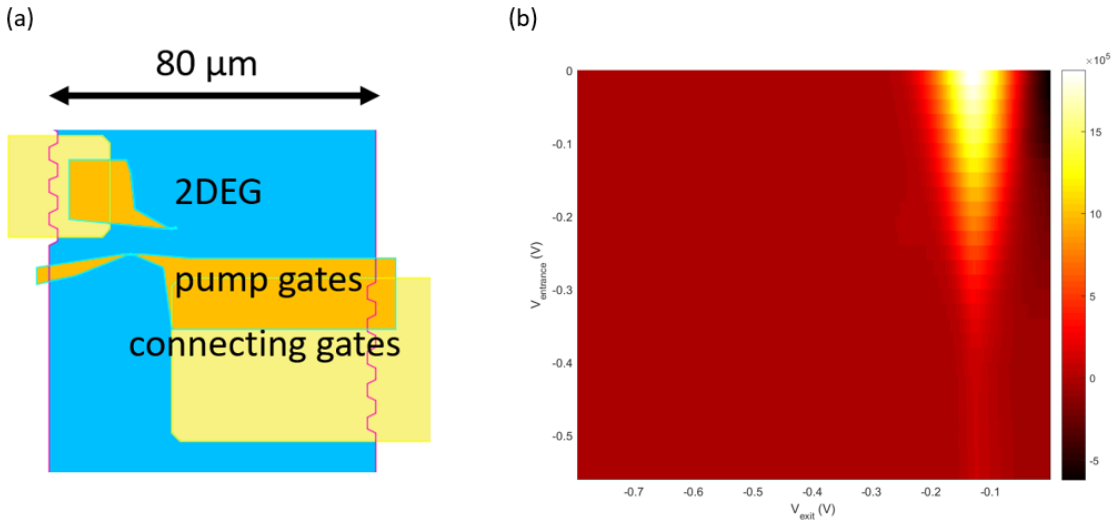

Figure 4.10: Device without polyimide, Pattern Ei. (a) Device layout. (b) The current colourmap of the current as a function of entrance and exit gate voltage with 110 MHz -5 dBm RF applied to the entrance gate; the unit for current is pA.

close together the gates are. This proves that the current cannot be coming from any type of pumping.

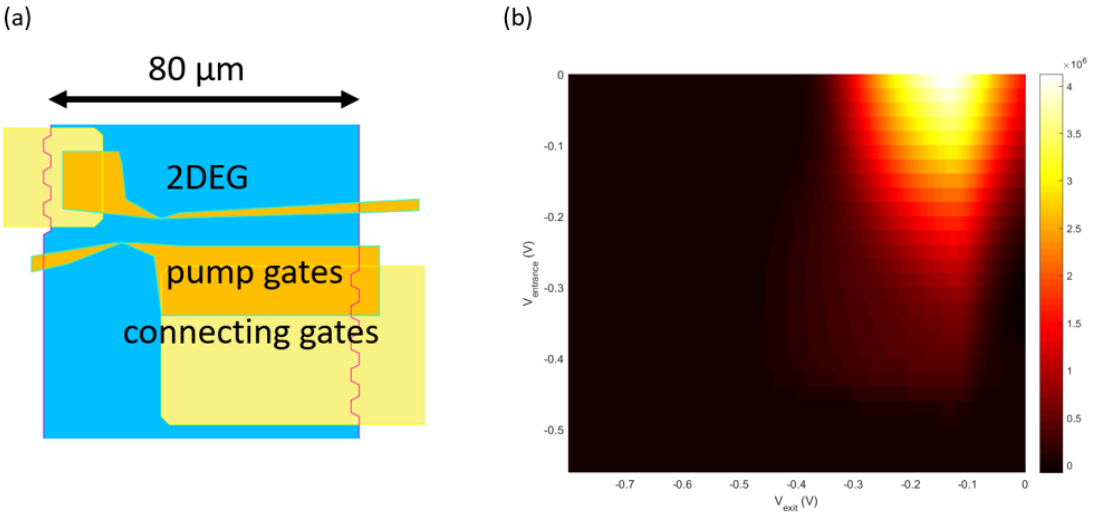

Figure 4.11: Device without polyimide, Pattern Eii. (a) Device layout. (b) The current colourmap of the current as a function of entrance and exit gate voltage with 110 MHz -5 dBm RF applied to the entrance gate.

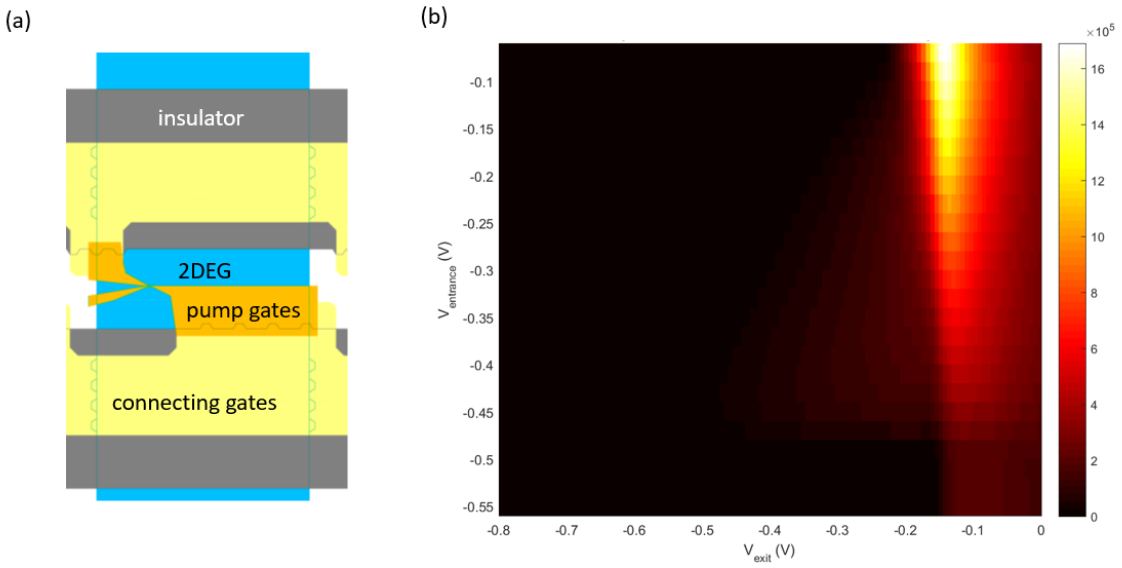

Figure 4.12: Device with polyimide, Pattern A. (a) Device layout. (b) The current colourmap of the current as a function of entrance and exit gate voltage with 110 MHz -5 dBm RF applied to the entrance gate.

4.4 Model of the rectified current

We begin by introducing the rectification model built by Giblin *et al.* [53]. Figure 4.13 describes their narrow-channel (2 μm) bar-gate device and the schematic of

their measurement circuit. The simplified circuit is shown in Fig. 4.14. The 2DEG conductance under the gate $G_{bar}(V_{Gbar})$ is dependent on the gate voltage V_{Gbar}. The DC source-drain voltage V_{B0bar} is caused by the offsets including the pre-amplifier and deliberately applied bias from a voltage source. An AC signal added to a DC voltage was applied to the gate: $V_{Gbar}(t) = V_{G0bar} + V_{ACbar}\sin(2\pi ft)$. Because of the capacitance between the RF gate and the 2DEG, there exists a pick up voltage both on the source and drain sides. There is impedance between source 2DEG or drain 2DEG and ground, and the impedance and capacitance forms a potential divider. But the device is not perfectly symmetric, so the RF voltage reaching the source and drain end is not divided the same. As the AC voltage applied to RF gate the conductance of the 2DEG under the gate is also oscillating. The instantaneous current equals the oscillating voltage times the oscillating conductance, so the instantaneous current in one cycle is asymmetrical, which generates DC rectified current, and the total bias voltage can be described as:

$$V_{Bbar}(t) = V_{B0bar} + kV_{ACbar}\sin(2\pi ft + \Phi) \tag{4.1}$$

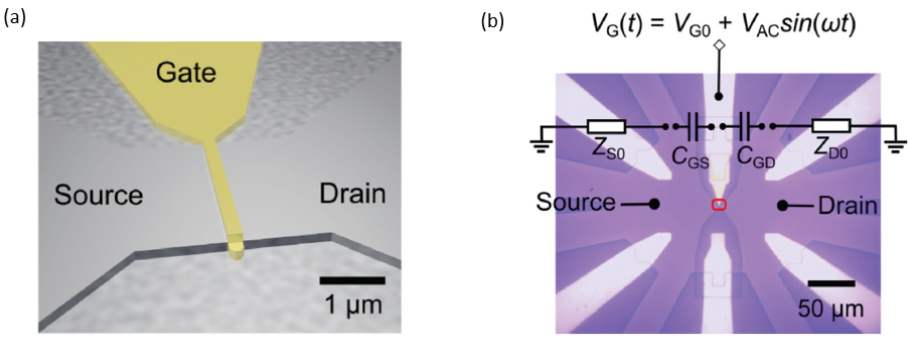

Figure 4.13: (a) Illustration of the narrow-channel bar gate device studied by Giblin *et al.* [53]. (b) Optical microscope image of the device and schematic of the measurement circuit. Taken from [53].

Here k and ϕ are amplitude and phase coupling constants that depend on the frequency. Figure 4.14 (b) describes the conductance as a function of V_{G0bar} with no AC voltage applied. When $V_{G0bar} = -0.3$ V and $V_{ACbar} = 0.1$ V is applied to the gate, the gate voltage change and conductance changes in one AC cycle are as shown in Fig. 4.14 (c) and (d). Assuming $V_{B0} = -100\mu$V and phase coupling constant $\Phi = \pi$,

Fig. 4.14 (e) describes the time-dependent bias voltage. The instantaneous current is plotted in Fig 4.14 (f). The rectified current can be described as:

$$I_{Rbar} = f \int_0^{1/f} V_{Bbar}(t) G_{bar}(t) dt \tag{4.2}$$

Then Eq. 4.1 was substituted into Eq. 4.2, and Eq. 4.2 can be simplified as

$$I_{Rbar} = f \left[\int_0^{1/f} V_{Bbar}(t) G_{bar}(t) dt + V_{ACbar}(t) k cos(\Phi) \int_0^{1/f} G_{bar}(t) sin(2\pi f t) \right] \tag{4.3}$$

Here the term $kcos(\Phi)$ was treated as a fitting parameter, and then the rectified current was simulated to compare with the measurement data. Since both the conductance G_{bar} and the source-drain bias V_{Bbar} are oscillating in time, the average DC current can be positive or negative.

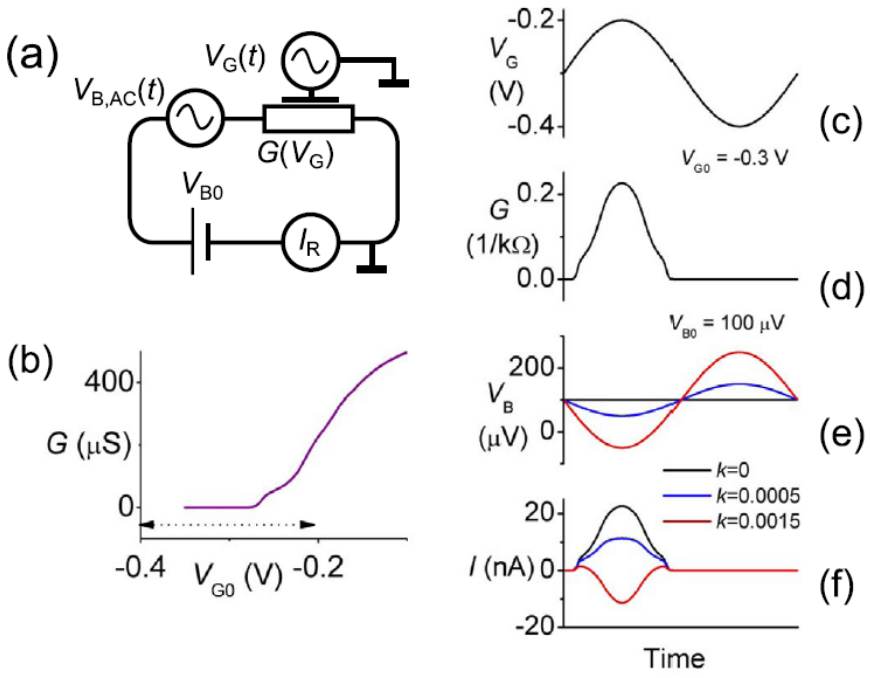

Figure 4.14: (a) The simplified model of the narrow-channel bar gate device studied by Giblin *et al.* [53]. (b) Conductance as a function of gate voltage when no RF is applied. (c) Instantaneous gate voltage change in one cycle when RF is applied. (d) Instantaneous conductance change in one cycle when RF is applied. (e) Instantaneous bias voltage change in one cycle when RF is applied. (f) Instantaneous rectified current change in one cycle when RF is applied. Taken from [53].

Our device is more complex than Giblin's device. Figure 4.15 describes the schematic of the measurement circuit. The entrance gate is connected to a RF signal with a DC offset: $V_{Entrance}(t) = V_{Entrance} + V_{AC}\sin(2\pi f\mathrm{t})$. The pre-amplifier has a DC voltage offset V_{B0} which is about 300 μV. As in Giblin's model, we also have an RF pick-up voltage on the source and drain 2DEG. We can describe time-dependent bias voltage between the source and drain as:

$$V_B(t) = V_{B0} + k_1 V_{AC}\sin(2\pi f\mathrm{t} + \Phi_1) \tag{4.4}$$

where k_1 is the amplitude coupling constant and Φ_1 is the phase coupling constant, which are both dependent on RF frequency f. However, the mechanism of the 2DEG conductance variation under the gates is very different from Giblin's model: the DC voltage applied to the entrance gate will not affect the conductance of the 2DEG much, as when we sweep the entrance gate voltage the conductance only drops by about 5% (Fig 4.16). This is because the entrance gate does not reach across the 2DEG channel. However, the RF signal of the entrance gate couples to the 2DEG under the exit gate which will cause the 2DEG Fermi level to oscillate. The conductance under the exit gate will be determined by the relative voltage difference between the exit gate and 2DEG. The relative voltage difference can be described as

$$V_{Exitdiff}(t) = V_{Exit} + k_2 V_{AC}\sin(2\pi f\mathrm{t} + \Phi_2) \tag{4.5}$$

where V_{Exit} is the DC voltage we apply to the exit gate, k_2 and Φ_2 are the amplitude coupling constant and phase coupling constant of the 2DEG under the exit gate respectively, which are both a function of frequency.

The DC rectified current over one cycle of the applied gate voltage can be calculated from the following equation

$$I_R = f\int_0^{1/f} V_B(t)G(t)dt \tag{4.6}$$

Here $G(t)$ is changing with time depending on $V_{Exitdiff}(t)$. We have tried substituting Eq. (4.4) and Eq. (4.5) into Eq. (4.6) and building the model of our devices quantitatively, but we find it is very difficult to achieve. There are two reasons: first, there are twice as many coupling constants as in Giblin's model, so fitting to the data is much more complex. Second, the impedance between the source/drain 2DEG and ground depends on both frequency and on V_{exit}. From Eq. 4.5 we can learn that the $V_{Exitdiff}$ is dependant on V_{exit} and $V_{Exitdiff}$ will determine the exit gate resistance. Here we make one assumption: we assume the phase constant Φ_1 in Eq. (4.4) and Φ_2

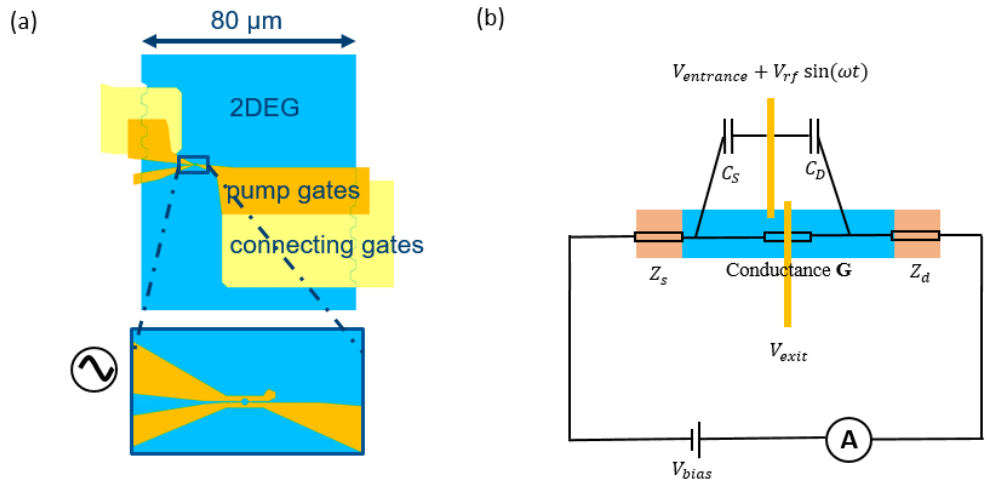

Figure 4.15: Schematic circuit elements used to model rectification. (a) Layout of pattern A device without polyimide. (b) Schematic of the measurement circuit. C_S and C_D are stray capacitances from the source and drain, Z_S and Z_d are impedances from the source and drain leads to ground.

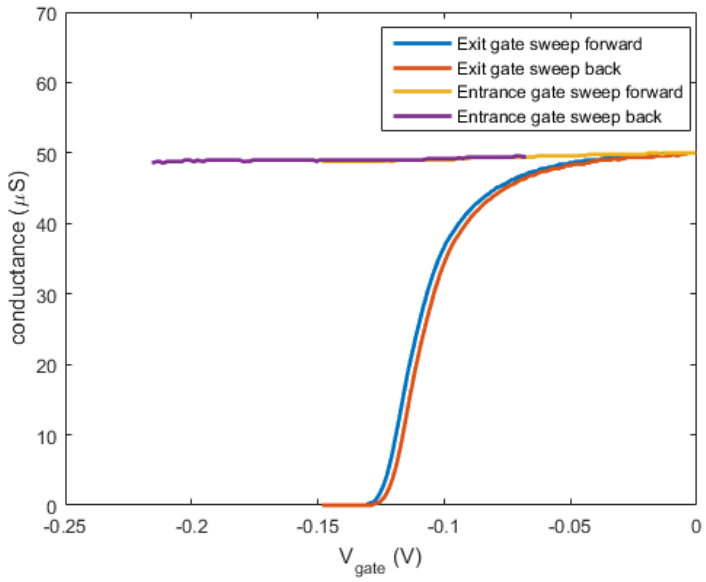

Figure 4.16: Conductance as a function of gate voltage V_{gate}. The conductance only changes by 5 % when sweeping the entrance gate voltage.

in Eq. (4.5) is irrelevant. Because we can learn from Fig. 4.16 the entrance gate does

not affect the conductance so we think that the phase of the pick-up relative to the entrance gate should not matter. Then we can simplify Eq. (4.4) as follows:

$$V_B(t) = V_{B0} + k_1 V_{AC} \sin(2\pi f t) \tag{4.7}$$

The value of k_1 has to be between -1 and 1. Also the value of k_2 in Eq. (4.5) has to be between -1 and 1. Then we substitute Eq. (4.7) and Eq. (4.5) into Eq. (4.6) and build the model to fit the measurement data. The result is as follows:

(a)

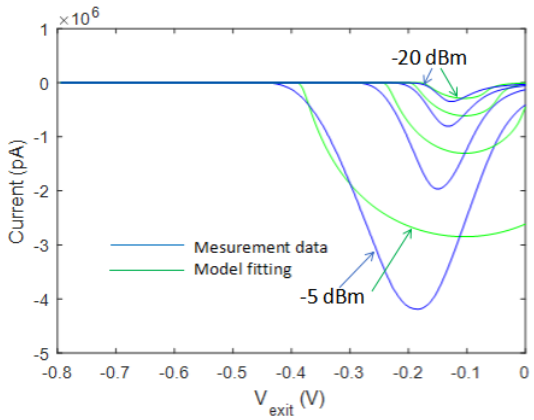

(b)

RF POWER	k_1	k_2
-20 dBm	0.3125	0.8379
-15 dBm	0.3591	0.6379
-10 dBm	0.4168	0.5859
-5 dBm	0.5047	0.7390

Figure 4.17: Comparison of the rectified current measurement data and quantitative model fitting of a device without polyimide, Pattern A. (a) The rectified current as a function of exit gate voltage V_{Exit} for RF amplitude between -20 dBm and -5 dBm, with RF frequency at 110 MHz and entrance gate DC voltage $V_{Entrance} = 0$ V. Blue lines are the measurement data and green lines are the model fitting. (b) The model fitting parameters k_1 and k_2 for RF amplitude between -20 dBm and -5 dBm.

From Fig. 4.17 to Fig. 4.18 we learn that the quantitative model does not fit the measurement data perfectly. This is because in our experiment, on one hand the conductance is dependent on the source-drain bias voltage which is mainly caused by the RF pick-up, and on the other hand, from Eq. (4.7), we can learn that the RF pick-up is also affected by V_{Exit} and the conductance. This will make the perfect quantitative model difficult to build and we choose a qualitative model to explain this rectified current.

In the following part we will explain qualitatively how our model fits the measured results.

We measure the rectified current against exit gate voltage for RF amplitudes between -20 dBm and -5 dBm [Fig 4.19 (a)], at zero source-drain bias and entrance gate DC voltage $V_{Entrance} = 0$ V. We can see that the peak rectified current increases

(a)

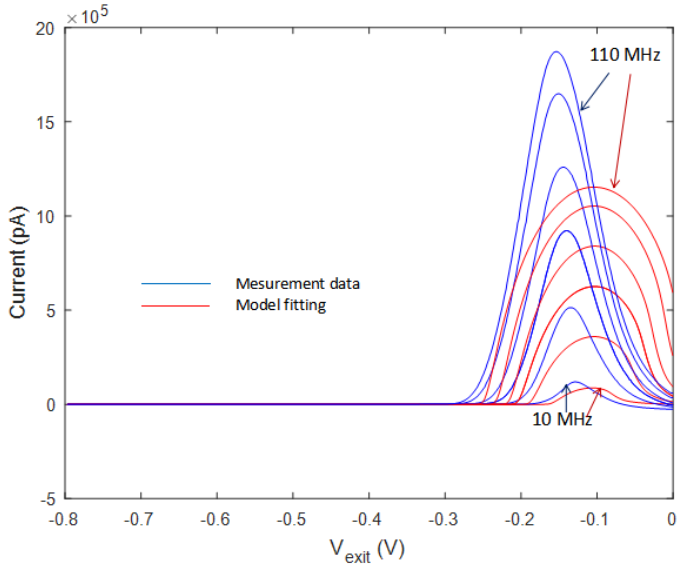

(b)

RF Frequency	k_1	k_2
10 MHz	-0.301	0.2
30 MHz	-0.1192	0.3345
50 MHz	-0.2036	0.4121
70 MHz	-0.2708	0.4700
90 MHz	-0.3366	0.5528
110 MHz	-0.3670	0.6339

Figure 4.18: Comparison of the rectified current measurement data and quantitative model fitting of a device with polyimide, Pattern A. (a) The rectified current as a function of exit gate voltage V_{Exit} for RF frequency of 10 MHz, 50 MHz, 70 MHz and 110 MHz, with RF power at -10 dBm and entrance gate DC voltage $V_{Entrance} = 0$ V. Blue lines are the measurement data and red lines are the model fitting. (b) The model fitting parameters k_1 and k_2 for RF frequency of 10 MHz, 50 MHz, 70 MHz and 110 MHz.

with amplitude, and the peak current happens near pinch-off voltage of the exit gate voltage.

We measure the rectified current against exit-gate voltage for RF frequency at 10 MHz, 50 MHz, 70 MHz, 90 MHz, 110 MHz [Fig 4.19 (b)], for fixed RF amplitude -10 dBm. We took measurements at zero source-drain voltage bias and entrance gate DC voltage $V_{Entrance} = 0$ V. We can see from the graphs that the peak rectified current also increases with frequency, and the peak current happens near pinch-off of the exit gate.

Figure 4.20 describes how our model explains the measurement data. Figure 4.20 (a) presents the schematic of our model: when RF is applied to the entrance gate, the entrance gate to the 2DEG acts like a capacitor. The 2DEG under the exit gate is like a variable resistor depending on the DC voltage applied to the exit gate. The source and drain ohmic contacts act as resistors (several kΩ). The electrometer is connected between the source and drain to measure the current.

When the exit gate is near pinch-off, the 2DEG resistance under the exit gate $R_{ExitGate} \gg R_{SO}$ (source ohmic resistance), the drain ohmic side acts like an open

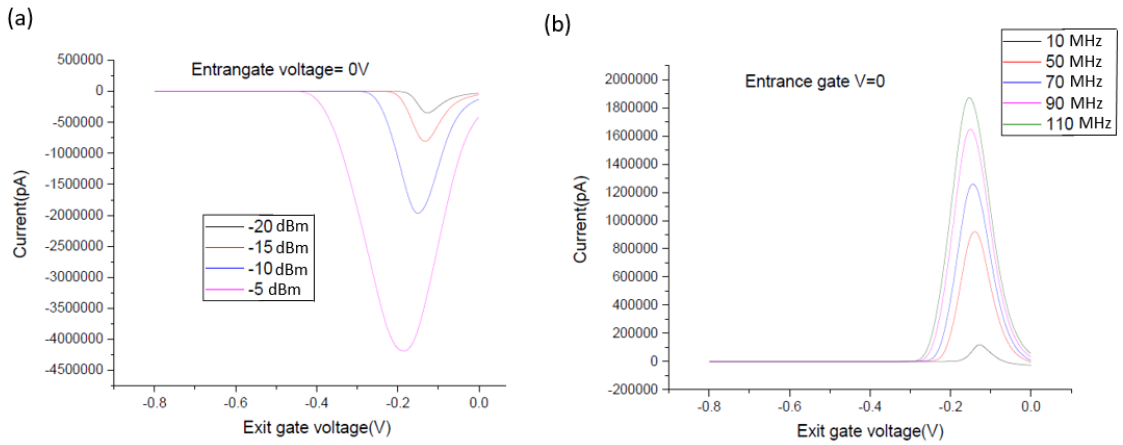

Figure 4.19: (a) The rectified current as a function of exit gate voltage V_{Exit} for RF amplitude between -20 dBm and -5 dBm, with RF frequency at 110 MHz and entrance gate DC voltage $V_{Entrance} = 0$ V. (b) The rectified current as a function of exit gate voltage V_{Exit} for RF frequency between 10 MHz and 110 MHz, with RF amplitude at -10 dBm and entrance gate DC voltage $V_{Entrance} = 0$ V.

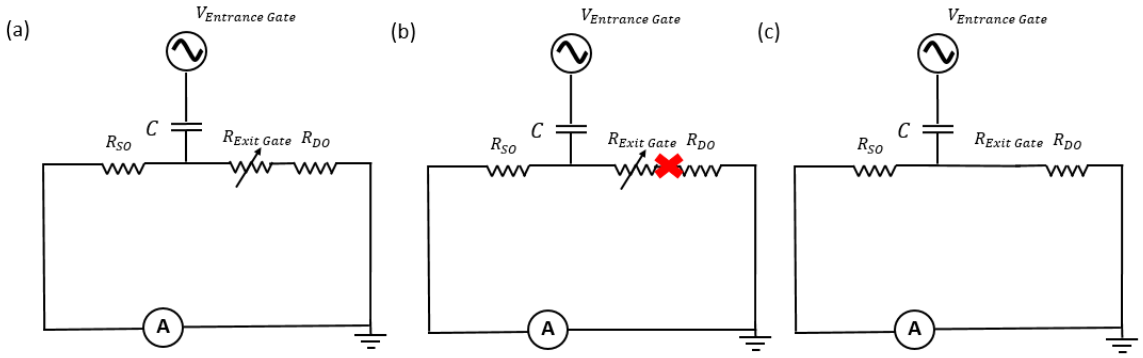

Figure 4.20: (a) Schematic of the measurement circuit. (b) Simplified schematic of measurement circuit when the DC voltage on exit gate is near pinch off voltage. (c) Simplified schematic of measurement circuit when the DC voltage on exit gate is small.

circuit and the RF current will only flow through the source path [Fig 4.20 (b)]. Then the capacitor C and R_{SO} act like a potential divider, and we can write the voltage applied to the source ohmic:

$$V_{source} = V_{RF} \times \frac{R_{SO}}{Z_C + R_{SO}} \tag{4.8}$$

here $Z_C = \frac{1}{2\pi j f C}$ is the impedance of the capacitor. As the frequency f increases, Z_C decreases, so V_{source} increases. This can explain our frequency-dependent measurements

Total conductance (uS)	Total resistance (Ω)	Source and drain resistance (Ω)	Exit gate resistance (Ω)
40	25000	20000	5000
30	33000	20000	13000
20	50000	20000	30000
10	100000	20000	80000

Table 4.1: The total resistance, source and drain resistance, exit gate resistance vs the total conductance. The data is from Fig. 4.16.

well. This model can explain our power dependent measurements well, V_{source} will become larger as V_{RF} increases, causing the rectified current to increase.

When the negative DC voltage added to the exit gate is small, the 2DEG resistance under the exit gate $R_{ExitGate} \ll R_{SO}$ (source ohmic resistance). We can neglect the resistance caused by the exit gate voltage. The RF current will flow through both paths [Fig 4.20 (c)]. The voltage pick up on the source and drain will be similar. The electrometer measures the net DC current travelling through, so the rectified current will be small.

When large negative voltage is applied to the entrance gate, the electrons under the entrance gate will be depleted and there is little capacitance between the RF source and the 2DEG any more. This means RF signal cannot reach the 2DEG, therefore no rectified current will be generated. This explains our observation in Fig. 4.6 that the rectified current is small when $V_{entrance} < -0.3$ V.

Based on this qualitative model, we can also explain why the quantitative model is hard to build. From Fig. 4.16 we can learn that without applying any voltage to the entrance gate, the conductance is about 50 μS. If we assume that the resistances of source and drain are equal, then we can get the resistance of the source or drain as 10000 Ω. When we applied negative voltage to the exit gate, the total resistance of the circuit will be the sum of the resistance of the source, drain and the exit gate. The resistance of the exit gate vs conductance is shown in Table 4.1.

Then we can learn from the circuit in Fig. 4.20 (a) that the parallel resistance of source ohmic resistance and sum of exit gate resistance and drain ohmic resistance can be described as follows:

$$R_{Parallel} = \frac{R_{SO} \times (R_{Exitgate} + R_{DO})}{R_{SO} + (R_{Exitgate} + R_{DO})} \tag{4.9}$$

The capacitor and the parallel resistance act as a voltage divider in Fig. 4.20 (a) , then the voltage connected to the source ohmic can be written as:

$$V_{source} = V_{RF} \times \frac{R_{Parallel}}{Z_C + R_{Parallel}} \tag{4.10}$$

Total conductance (uS)	Entrance gate impedance (Ω)	Parallel resistance (Ω)	k_1
40	3593.8	6000	0.6254
30	3593.8	6970	0.6598
20	3593.8	8000	0.69
10	3593.8	9000	0.7146

Table 4.2: The entrance gate impedance, parallel resistance, ratio of the voltage connected to the source ohmic and RF voltage connected to the entrance gate vs conductance. The data is from Fig. 4.16.

where $Z_C = \frac{1}{2\pi jfC}$ is the impedance of the capacitor, then the capacitance can be calculated as

$$C = \varepsilon A/d, \tag{4.11}$$

Here, $\varepsilon = 12\varepsilon_0$ because of 33 % AlGaAs [10]. The area A can be the obtained from Fig. 4.21 as 176μm^2, and the separation between the surface and 2DEG $d = 90$ nm. Then we can get the capacitance for entrance gate is 2.01×10^{-13} F. When the frequency is 110 MHz, we can get the ratio (which is k_1 in Eq. 4.4) of the voltage connected to the source ohmic and RF voltage connected to the entrance gate in Table 4.2.

In Table 4.2 we can find that the ratio of the voltage connected to the source ohmic and RF voltage connected to the entrance gate is above 0.5, which means even at -20 dBm (peak-to-peak voltage is 63.2 mV) the oscillating source-drain bias will be more than 30 mV. This will cause the exit gate resistance $R_{Exitgate}$ to vary a lot during the RF cycle. This bias is so big that the device will be in the non-linear regime. Then we cannot even use Ohm's law $I = G \times V$ to build the quantitative model. This is another reason that the quantitative model is hard to build.

We learn that in terms of rectification the wide-channel pump device is worse than narrow-channel pump device: in our device (shown in Fig. 4.6) the maximum current is about 2000 nA for an RF power of -10 dBm and frequency 110 MHz, while in Giblin's narrow-channel device the maximum current is about 7 nA for an RF power of -11 dBm and frequency 200 MHz [54]. The rectified current in the wide-channel device is about 1000 times that in Giblin's device. This may be because the overlap area between the 2DEG and the RF gate in our device is much bigger than in Giblin's narrow-channel device. The overlap area in wide-channel device is about $15.03 * 9 + 15.03 * 11/4 = 176.6$ μm^2 (shown in Fig. 4.21) and the narrow-channel device is about $2 * 0.17 = 0.34$ μm^2. This means that the capacitance of wide-channel device is about 520 times bigger than the narrow-channel device and the RF pick-up on the source and drain 2DEG will be much bigger in our device, and explains why the wide-channel devices show so much rectified current.

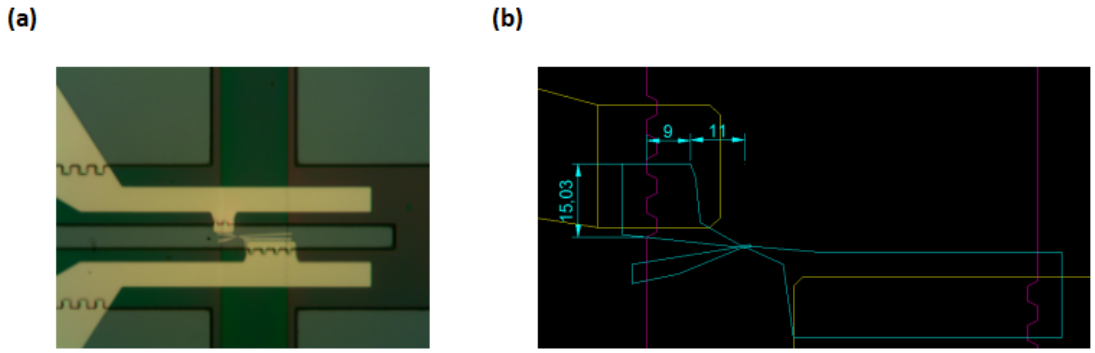

Figure 4.21: Overlap area calculation between the 2DEG and the RF gate in wide-channel device. (a) The optical image of the e-beam gates area. (b) The overlap area dimension.

4.5 Summary

In this chapter, we begin with the reason for designing the wide-channel electron pumps and how we observe rectified current. We present our work on the 4 x 32 multiplexed wide-channel electron-pump array, where instead of observing pumping current we observe rectified current, which is much bigger. We design several different types of single wide-channel electron pump devices and find that it is the single wide-channel electron pump itself that gives rectified current without pumping, and not the multiplexer. From these devices, we learn that the entrance gate does not have to go all the way across the channel to give the rectified current. And no matter how close together are the entrance and exit gate, we can observe rectified current. Then we explain the origins of the rectified current and build a model circuit to explain the measurement data of these devices. For future MUX pump arrays, we need to switch to a narrow-channel electron-pump design to make MUX pump arrays.

5

Transmission of radio-frequency signals through a quantum multiplexer

In this chapter we characterise the transmission of RF voltage signals through the quantum multiplexer using an array of bar gates. And we use multiplexers to do a statistical study of bar gates with different gate widths. Data are obtained from three kinds of devices: two different versions of multiplexed bar gate arrays and a single multiplexer structure to measure the resistance through each path.

5.1 MUX bar-gate devices

To multiplex electron-pump devices, we will need to pass an RF signal of about 100-1000 MHz frequency and peak-to-peak amplitude of at least 0.5 V (measured from Chapter 6) at 4 K through the multiplexer to reach the entrance gate of each electron pump. It will be important to test how an RF signal is transmitted through a multiplexer to the gates of a device. We decided to do relatively simple experiments on multiplexed bar-gate arrays to see if we can get enough RF voltage through the quantum multiplexer on to the entrance gate of the single-electron pump that modulates the 2DEG conductance. We have done both AC measurements and DC measurements to test this. All these

measurements in this section were carried out at 4 K in the Pump Dip Station at Cavendish Lab.

The multiplexed bar gate arrays layout is shown in Fig 5.1 (a). There are two multiplexers on the chip which are located on the bottom and left of the chip. The bottom multiplexer is used to choose 2DEG channel the source-drain current flows through, and the left multiplexer is to choose which row of the bar gate device the RF voltage reaches. Figure 5.1 (b) presents the single bar gate device within the array. There are 256 bar gate devices of 16 different widths on the chip. We fabricated the multiplexed bar gate devices in the order of mesa, ohmic, e-beam gates, polyimide and optical gates [see Fig 5.1 (c)]. This section will introduce the pinch-off voltage analysis, maximum dG/dV_g analysis, AC and DC measurements on a single bar-gate device and rectified current of the MUX bar gate devices in parallel. The bar gate width of each bar gate device is shown in Fig 5.2. The widths of all the bar gates in the same column are equal, and the widths of each column range from 0.1 μm to 2 μm. The length of all bar gate devices is 2.4 μm. The gate width and gate length are described in Fig. 5.1 (d) and Fig. 5.1 (e) respectively.

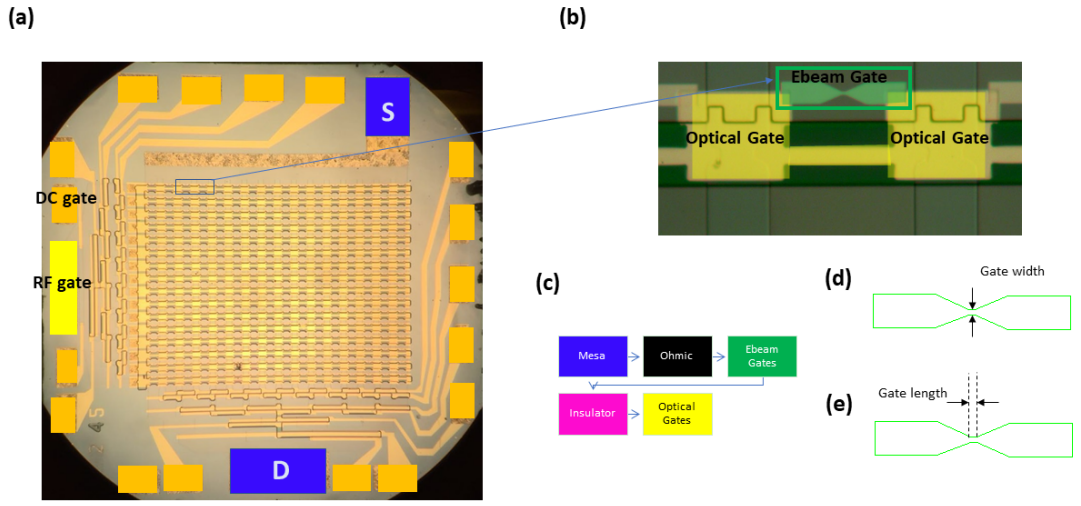

Figure 5.1: Multiplexed bar-gate arrays. (a) Optical image of the multiplexed bar-gate device. (b)Optical image of a single bar-gate device within the array. (c) The fabrication order. (d) The gate width. (e) The gate length.

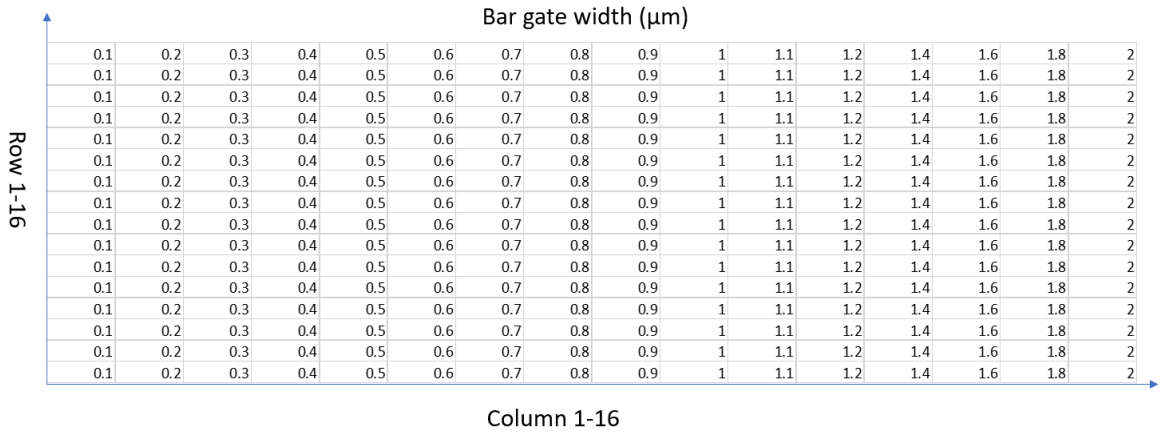

Figure 5.2: The bar gate width of each bar gate device on the multiplexed bar gate arrays.

5.1.1 Pinch-off voltage analysis of all 256 gates

Firstly, the pinch-off voltages of all the 256 gates are measured. Figure 5.3 (a) shows a typical conductance vs voltage trace for a device, here we choose the device in the first column and first row, which is 0.1 μm wide. Figure 5.3 (b) shows a colormap of the pinch-off voltage of all 256 gates. Among the 256 gates, only the first row gate of the 0.2 μm column does not pinch off, all the other 255 gates work. The yield of this chip is 99.6%.

We studied how the pinch-off voltages changes with gate width. Figure 5.4 shows the average pinch-off voltage as a function of the gate width. Table 5.1 shows the mean and error of each width. We estimate our uncertainty to be the standard deviation divided by the square root of the number N = 16 of bar gates we measure, which is sd/sqrt(N).

We can learn from here that there is a big difference between the 0.1 μm and 0.2 μm wide or larger. We need more negative voltage to pinch off 0.1 μm wide bar gates (-0.4 V) than the 0.2 μm wide or larger bar gates (-0.32 V to -0.3 V). This is because for 0.1 μm wide bar gates, the bar gate width is comparable to the distance between the 2DEG and the GaAs surface (90 nm), so the bar gate is not wide enough to make the electric field uniform under the gate. For 0.2 μm wide or larger gates, as the bar gate width is much larger than the 2DEG depth, so the electric field under the gates is uniform. In this case, at the centre part under the gate the electric field would be the same we apply the same voltage to 0.2 μm wide or larger gates. The carrier density of the 2DEG is dependent on the electric field. So for 0.2 μm wide or larger gates, the

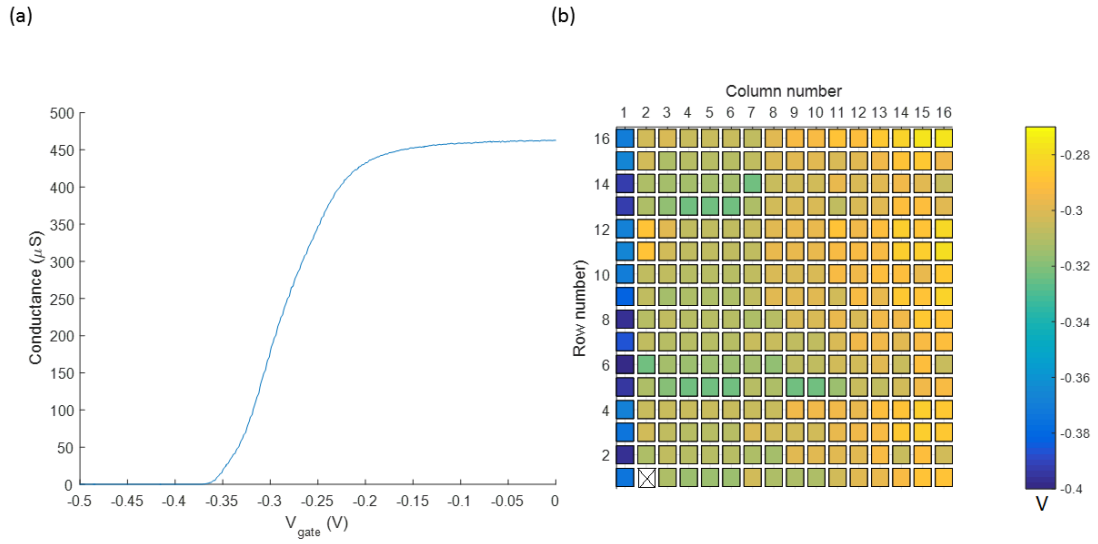

Figure 5.3: (a) Conductance as a function of gate voltage V_g. (b) Pinch-off voltage as a function of device location. The colour scale shows the pinch-off voltage.

pinch off voltages are very similar here. When the same voltage is applied for 0.1 μm wide bar gates the carrier density change of the 2DEG is smaller than that for 0.2 μm wide or larger gates, this is why more negative voltage is needed to pinch off 0.1 μm wide bar gates. Figure 5.5 describes a schematic of these two different electric field cases.

Gate width (μm)	Mean (V)	Error (mV)	Gate width (μm)	Mean (V)	Error (mV)
0.1	-0.4003	2.9	0.9	-0.3049	1.7
0.2	-0.3129	2.0	1.0	-0.3046	1.4
0.3	-0.3138	2.0	1.1	-0.3001	1.5
0.4	-0.3158	1.9	1.2	-0.2989	1.2
0.5	-0.3178	1.6	1.4	-0.2964	1.9
0.6	-0.3174	2.2	1.6	-0.2971	1.9
0.7	-0.3110	2.5	1.8	-0.2961	1.5
0.8	-0.3079	1.4	2.0	-0.2973	1.9

Table 5.1: Mean and error of the pinch-off voltage for bar gate widths from 0.1 to 2 μm.

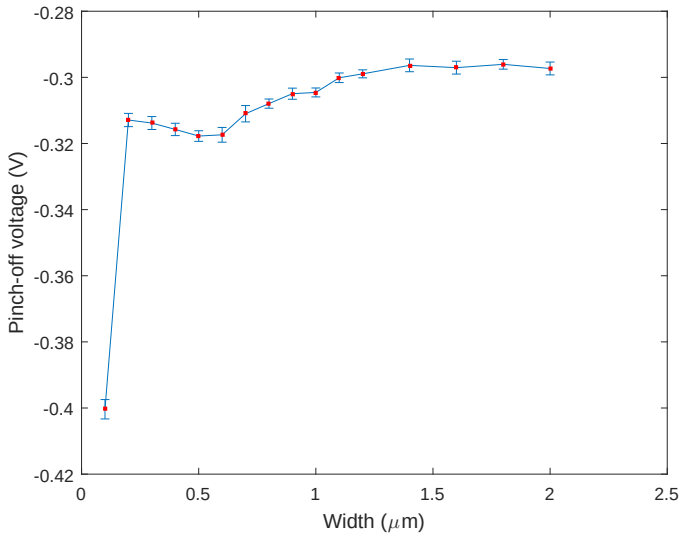

Figure 5.4: Average pinch-off voltage as a function of gate width from 0.1 to 2 μm.

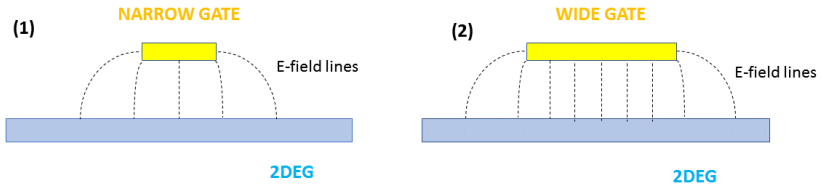

Figure 5.5: The sketch of the electric field for two cases: here 0.1 μm gate is narrow gate, 0.2 μm to 2 μm gate is wide gate

5.1.2 Transconductance with gate voltage (dG/dV_g)

The maximum transconductance value with gate voltage is the biggest dG/dV_g for each device. Figure 5.6 (a) is a dG/dV_g plot for 16 devices in Row 2 and the gate width ranges from 0.1 μm to 2 μm. Here we want to study if there is any correlation between the biggest dG/dV_g and gate width of the devices. Figure 5.6 (b) and Figure 5.7 (b) are the color map and a plot for different gate widths for the maximum dG/dV_g respectively. The maximum dG/dV_g is the point where the conductance depends most

strongly on V_g. We found that for the maximum dG/dV_g analysis, the 0.1 μm wide bar gate gives a smaller value than the other bar gates which are 0.2 μm wide or larger. Also, there are two maximum values for the 0.1 μm wide bar gate [Fig. 5.7 (a)], which is because the wide part of the bar gate [Fig. 5.1 (e)] pinches off the 2DEG firstly and the narrow part pinches off the 2DEG secondly. Besides, we can also learn from Fig 5.7 that the maximum dG/dV_g has an increasing trend as the gate width increase. We believe this is because when the same voltage is applied the electric field strength at the centre of the gates is generally increasing as the bar gate width becomes larger (the electric field at the centre is the superposition of contributions from across the whole width of the bar gate.). This means the conductance trace becomes steeper and has bigger dG/dV_g.

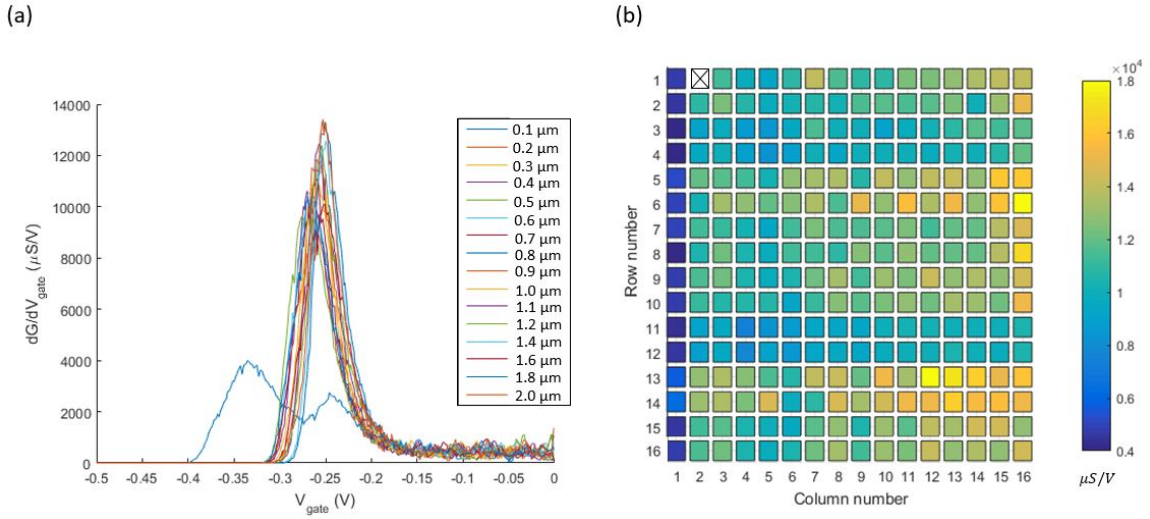

Figure 5.6: Maximum dG/dV_{gate} analysis of the multiplexed bar gate arrays. (a) dG/dV_{gate} as a function of V_{gate} for 16 bar gates from a single row (Row 2), the gate width ranges from 0.1 μm to 2 μm. (b) The maximum dG/dV_{gate} colour map of 256 gates. The colour scale shows the maximum dG/dV_{gate}.

5.1.3 Pinch-off voltage shift of all 256 gates with radio frequency signal added

As you apply an RF signal to the bar gate device, the positive half cycle which is the mid-to-peak amplitude of the AC voltage will increase the conductance. This will cause when RF signal is applied the conductance in the positive half-cycle to be larger than when no RF signal applied. The conductance in the negative half-cycle will be smaller than when no RF signal is applied, and the pinch-off voltage will shift to more

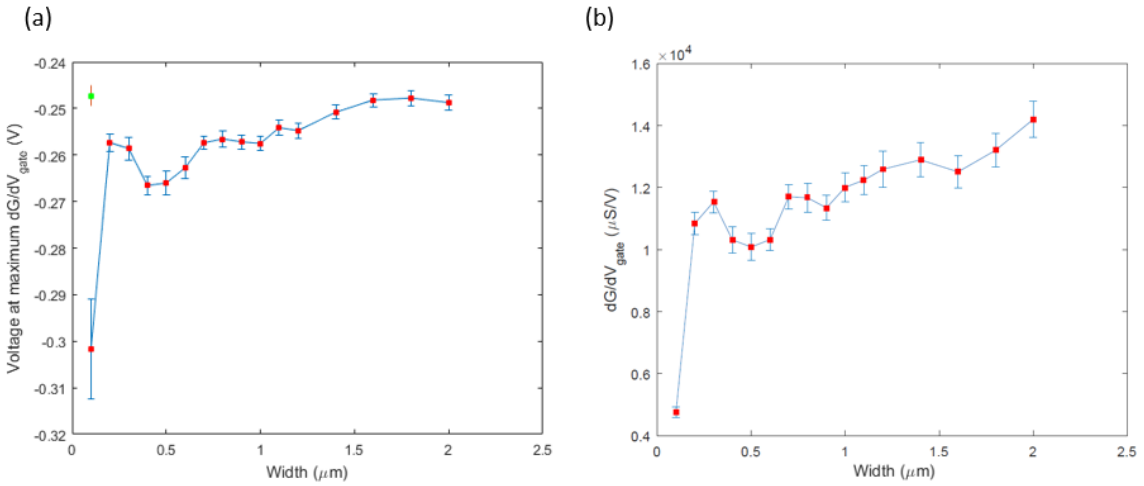

Figure 5.7: Maximum dG/dV_{gate} analysis. (a) The voltage V_{maxdG/dV_g} at maximum dG/dV_g as a function of gate width from 0.1 to 2 μm, the green square is the second maximum dG/dV_g point of 0.1 μm bar gate devices. (b) The maximum dG/dV_g as a function of gate width from 0.1 to 2 μm.

negative values when RF is applied on the bar gate device [53]. The pinch-off shift is the AC amplitude of the RF voltage on the gate. This was explained in Chapter 4. So measuring the pinch-off voltage shift allows us to estimate how much RF voltage is getting to the bar gate. Figure 5.8 shows the schematic of the pinch-off voltage change in one AC cycle of an RF signal.

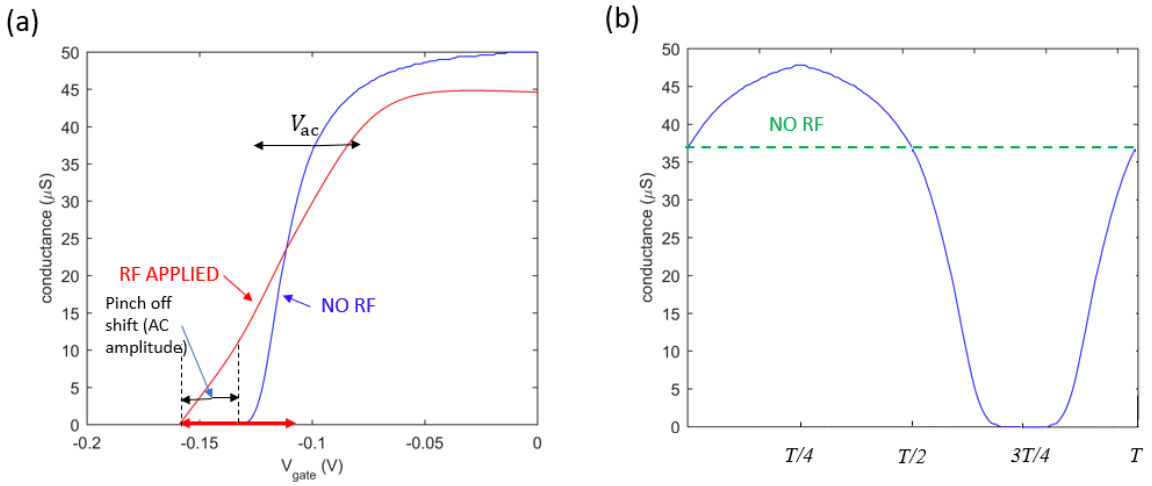

Figure 5.8: Pinch-off voltage change when RF signal applied. (a) The pinch-off voltage change when RF applied. (b) Conductance change through one AC cycle, the green dashed line is the conductance without RF signal applied.

We measured the pinch-off voltage of all 256 gates with two particular RF signals (110 MHz, -10 dBm and 10 kHz, -10 dBm). We compare this to the voltages when no RF signal is added to see the RF transmission throughout the sample.

Figure 5.9 (a) shows the pinch-off voltage change after a 10 kHz, -10dBm RF signal is applied. Figure 5.9 (b) is the average value for different gate widths. We can learn from the measurements that the pinch-off voltage will go about -0.186 V more negative when a 10 kHz, -10dBm RF signal is applied. If we set -10 dBm RF signal on the signal generator, it will deliver 0.1 mW to a 50 Ω load. The peak voltage here is sqrt(2) * sqrt(0.1 mW * 50 Ω) = 0.1 V. As the bar gate device is an open circuit, the AC voltage amplitude reaching the device will be the sum of the incident wave and reflected wave. It increases by factor of 2 because of the standing wave. So in the case of no attenuation the voltage shift here should be -0.2 V. Here 10 kHz RF signal transmits to the bar gates very well (0.186/0.2=93%).

Figure 5.10 shows the pinch-off voltage change after a 110 MHz, -10 dBm RF signal is applied. Figure 5.10 is the average and error plot of the pinch-off voltage change with gate width. We can learn from the measurements that for all the bar gate devices the pinch-off voltage shift is between -0.01 V and -0.08 V when a 110 MHz, -10 dBm RF signal is applied. The voltage signal is attenuated by between 60 % and 95 %. The pinch-off voltage change is much smaller when a 110 MHz, -10 dBm RF signal is applied than when a 10 kHz, -10dBm RF signal is applied.

From the results above, we can prove that the gate multiplexer transmits some RF signal to the bar gates, but there is more attenuation at high frequency. We believe this is because that there is capacitance in the measurement circuit. So at high frequency the attenuation is larger than at low frequency.

5.1.4 AC measurements on a single bar gate device

We wanted to explore whether the attenuation of the RF signal will depend on the position of the bar gate in the array. So we chose four different devices (Column 1, Row 6; Column 1, Row 16; Column 16, Row 12; Column 16, Row 16) which are at different locations on the sample, to do more detailed frequency and amplitude dependence. Figure 5.11 shows the pinch-off voltage as a function of frequency for an RF power of -10 dBm on Column 1 Row 6 (C1R6, 0.1 μm wide) device and Column 1 Row 16 (C1R16, 0.1 μm wide) device respectively. Figure 5.12 shows the pinch-off voltage as a function of frequency for an RF power of -10 dBm on Column 16 Row 12 (C16R12, 2 μm wide) device and Column 16 Row 16 (C16R16, 2 μm wide) device respectively. Here we set the colour scale zero to 1 μS because this will help us to see the pinch off

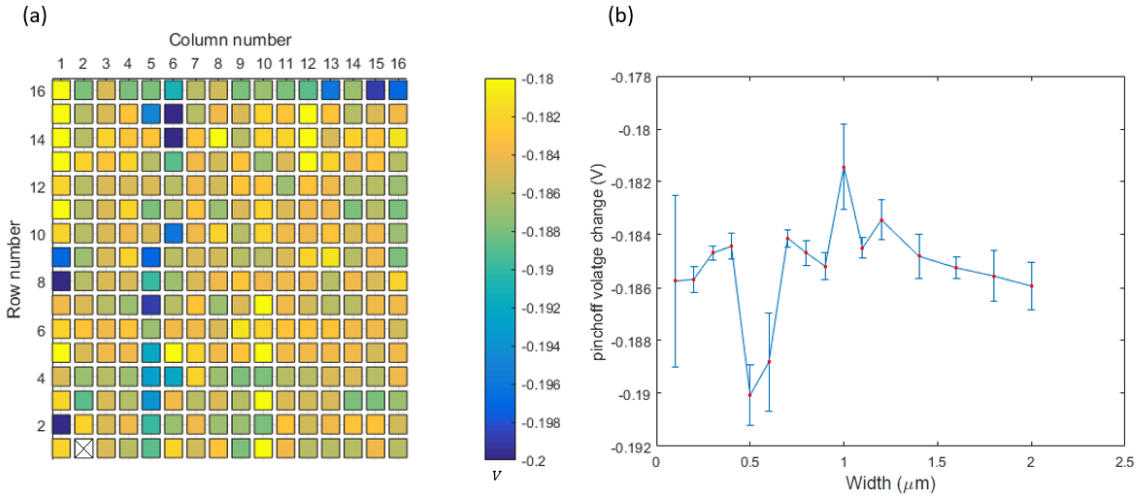

Figure 5.9: Pinch-off voltage change with 10 kHz -10dBm RF applied. (a) The colour map of pinch-off voltage change as a function of device position. (b) The average pinch-off voltage change for different gate widths.

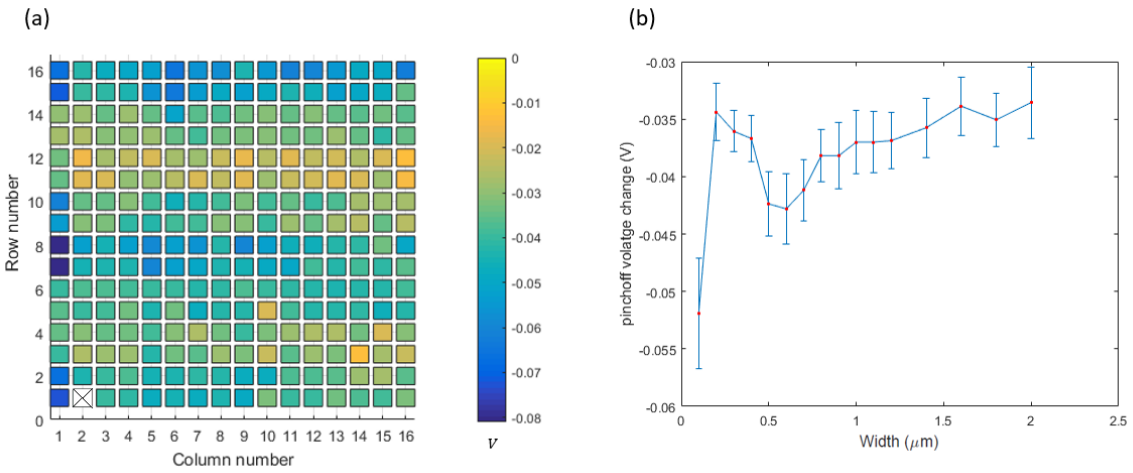

Figure 5.10: Pinch-off voltage change with 110 MHz -10dBm RF applied. (a) The colour map of pinch-off voltage change as a function of device position. (b) The average pinch-off voltage change for different gate widths.

voltage clearly. Figure 5.13 shows pinch-off voltage shift as a function of RF frequency for all the four gates we measured.

From the results, we can learn that the pinch-off voltage shift is heavily dependent on the frequency: At high frequency the pinch-off voltage shift is normally larger than at low frequency. Also the pinch-off voltage change is different for each bar

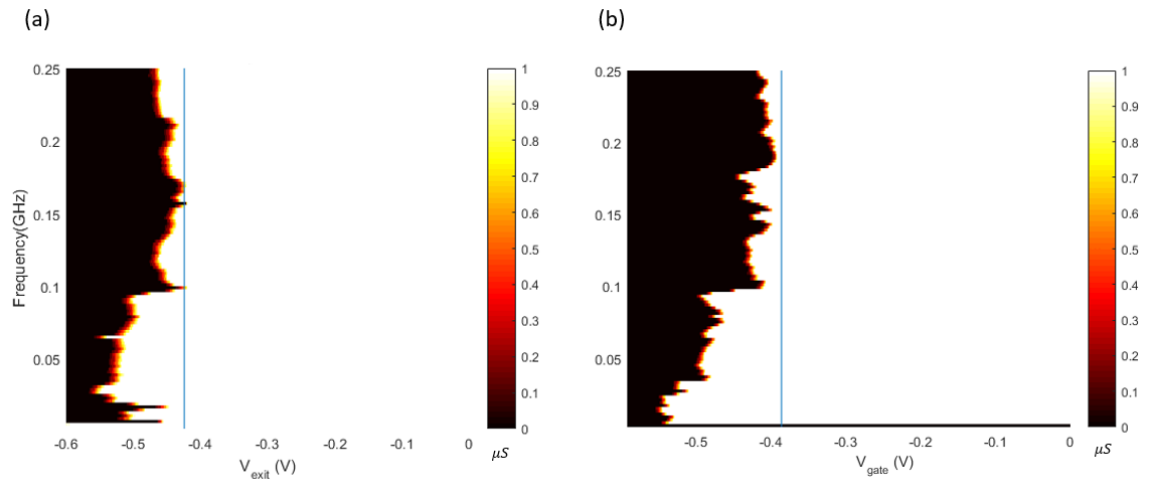

Figure 5.11: Conductance as a function of frequency and voltage when RF is applied at -10 dBm. (a) Column 1 Row 6 Device, 0.1 μm wide. (b) Column 1 Row 16 Device, 0.1 μm wide. The blue line is the pinch-off voltage when no RF signal is applied.

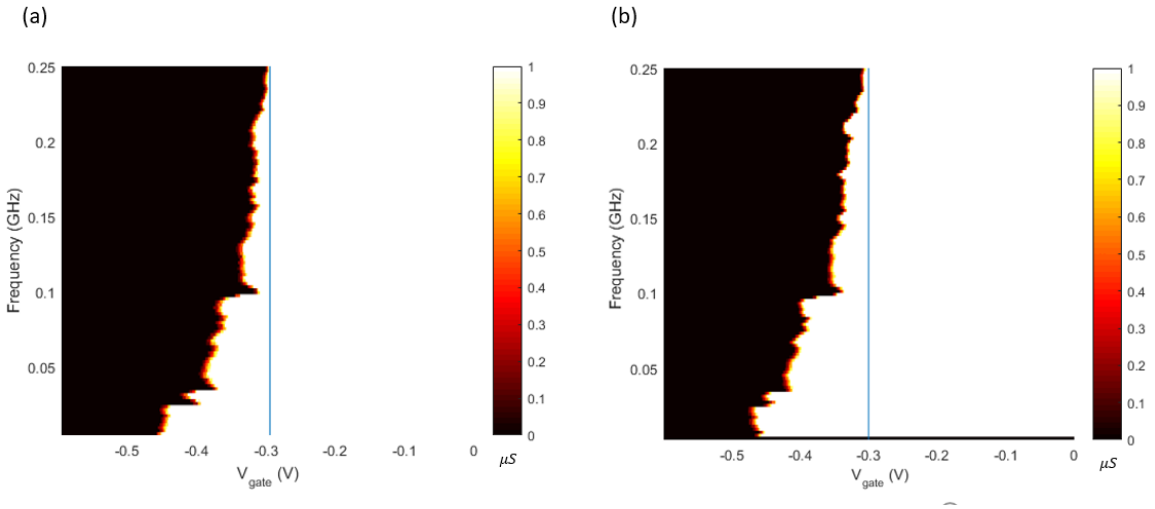

Figure 5.12: Conductance as a function of frequency when RF is applied at -10 dBm. (a) Column 16 Row 12 Device, 2 μm wide. (b) Column 16 Row 16 Device, 2 μm wide. The blue line is the pinch-off voltage when no RF signal is applied.

gate device. However, we cannot see a quantitative relationship between the pinch-off voltage change and device location. There are some very rapid variations of pinch off voltage with frequency (lots of spikes in the traces in Fig. 5.13). This also happens when we measure the pinch-off shift versus frequency in more simple devices. This might be because of multiple reflections in the RF cables.

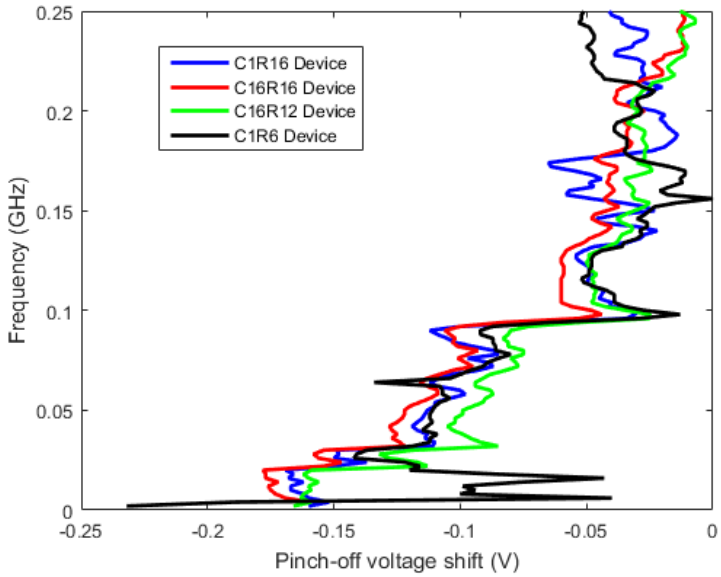

Figure 5.13: Pinch-off voltage shift as a function of RF frequency when -10 dBm RF power signal applied, for four different bar gates from Fig 5.11 and Fig 5.12.

We increase RF power to explore whether we can get enough RF voltage through the multiplexer to the pump devices. We choose the Column 16 Row 16 device to do RF power-dependent measurements at 110 MHz. Figure 5.14 (a) shows how the pinch-off voltage changes as a function of RF power. The red line is the pinch-off voltage without RF applied, and the blue line is the pinch off with different RF powers applied. This indicates that the pinch-off voltage becomes more negative from -15 dBm to -3 dBm, saturates from -3 dBm to 9 dBm and increases to 12 dBm. Figure 5.14 (b) shows the exact pinch-off voltage value at different RF power applied. However, we find that the pinch-off voltage shift is saturating at -3 dBm RF power and the maximum pinch-off voltage shift is about 120 mV which is not enough for the electron pumping. We also tried some other frequency like 10 kHz, and we met a similar situation.

We found this saturation problem is because of how we are controlling the multiplexer. We normally apply some negative voltage (-0.5 V) to the addressing gates to choose a particular 2DEG channel, and keep the other addressing gates grounded. Then when we do measurements, we sweep the addressing gate and input voltage at the same speed to do the DC experiments. Figure 5.15 describes the schematic of how quantum multiplexer works.

For example in Fig 5.15, in DC measurements if we want the input V (for example -0.3 V) to each path 1, normally we need to apply -0.5 V to the addressing gates G2, G4, G6 to pinch off the other paths except path 1. Then we sweep the other addressing

(a)

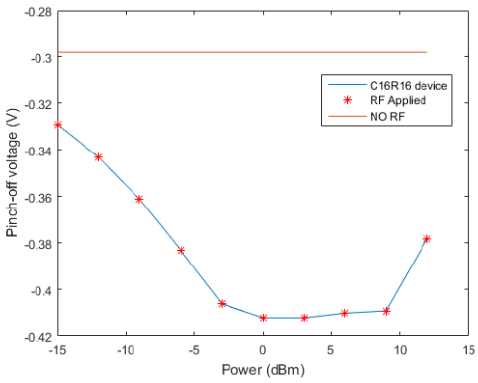

(b)

RF Power (dBm)	Pinch-off Voltage (V)
NO RF	-0.298
-15	-0.329
-12	-0.343
-9	-0.361
-6	-0.383
-3	-0.406
0	-0.412
3	-0.412
6	-0.41
9	-0.409
12	-0.378

Figure 5.14: Power dependence of pinch-off voltages as a function of RF power at 110 MHz. (a) Pinch-off voltage changes as a function of RF power applied. (b) Exact pinch-off voltage value with different RF power applied.

gates (G1, G3, G5) and input V to −0.3 V at a given rate (such as 50 V/hour). At the same time, we sweep further −0.3 V on the addressing gates G2, G4, G6 to −0.8 V (−0.5 V −0.3 V =−0.8 V) at the same rate. Then the input V is connected to path 1. Figure 5.15 (c) describes the voltage change of these gates as a function of time. After measurements are finished, firstly we sweep back input V, G1, G3, G5 gates to 0 V and at the same time sweep G2, G4, G6 gates to −0.5 V. Then we sweep the G2, G4, G6 back to 0 V.

To solve the saturation problem, we find that we need to control the multiplexer differently in the AC measurements. For example, if we want the input V (-0.3 V) + AC (RF) to go to path 1: firstly we need to apply some positive voltage (such as +0.2 V when we want to apply -10 dBm RF signal) to the addressing gates G1, G3, G5. This will ensure the positive half cycle of the RF signal is not pinched off by gates G1, G3, G5 and will reach the device connected to path 1. We can learn from Fig 5.8 that this positive half cycle is the main reason to cause the pinch-off voltage shift. In the positive half cycle, the conductance will be larger than when no RF is applied. The pinch-off voltage becomes more negative, by an amount equal to the AC voltage amplitude. Then we need to apply some negative voltage such as -1 V (this voltage should be large enough to pinch off the AC negative cycle) to the addressing gates G2, G4, G6 to pinch off the other paths except path 1. Then we sweep the other addressing gates (G1, G3, G5) to -0.1 V and input V to -0.3 V at a given rate (such as 50 V/hour). At the same time, we sweep a further -0.3 V on the addressing gates G2, G4, G6 to -1.3 V (-1 V -0.3V = -1.3 V) at the same rate. The input V (-0.3 V)

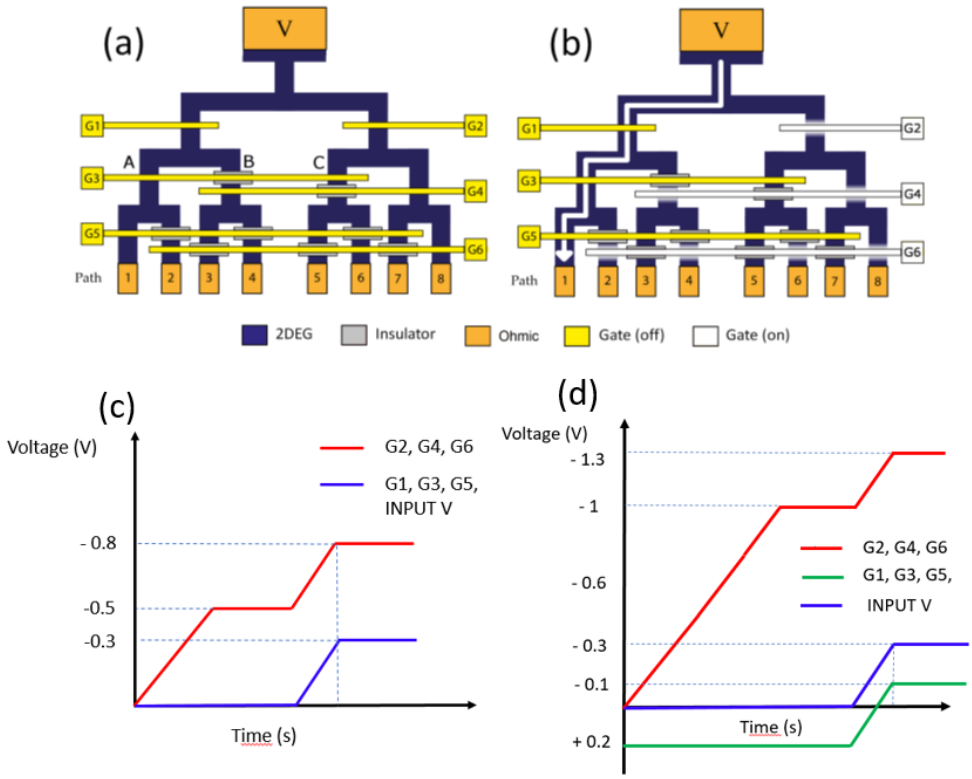

Figure 5.15: A schematic of the quantum multiplexer working principle. (a) Schematic diagram of the multiplexer structure. (b) Negative voltage applied to the addressing gates G2, G4 and G6 to pinch off the other paths except Path 1. (c) The addressing gates' and input voltage change as a function of time during DC measurements. (d) The addressing gates and input voltage change as a function of time for AC measurements. (a) and (b) are from [9].

and AC signal are now applied to the devices connected to path 1. Figure 5.15 (d) describes the voltage change of these gates as a function of time. After measurements are finished, firstly we sweep back input V to 0 V, G1, G3, G5 gates to 0 V (firstly +0.2 V then 0 V) at the same time sweep the G2, G4, G6 gates to -0.5 V. Then we sweep the G2, G4, G6 back to 0 V.

Figure 5.16 shows the pinch-off voltage shift as a function of RF power at 110 MHz after we apply some positive voltage such as +0.2 V or +0.3 V to the addressing gates which are not pinching off the 2DEG. We can learn from Fig. 5.16 that with +0.2 V applied the pinch-off shift saturates about 8 dBm. Compared with no positive voltage applied to the addressing gates (Fig 5.14), the saturating RF power enhance from -3 dBm to 8 dBm. When we increase the positive voltage to +0.3 V, we can find that the pinch-off voltage shift can be enhanced even more.

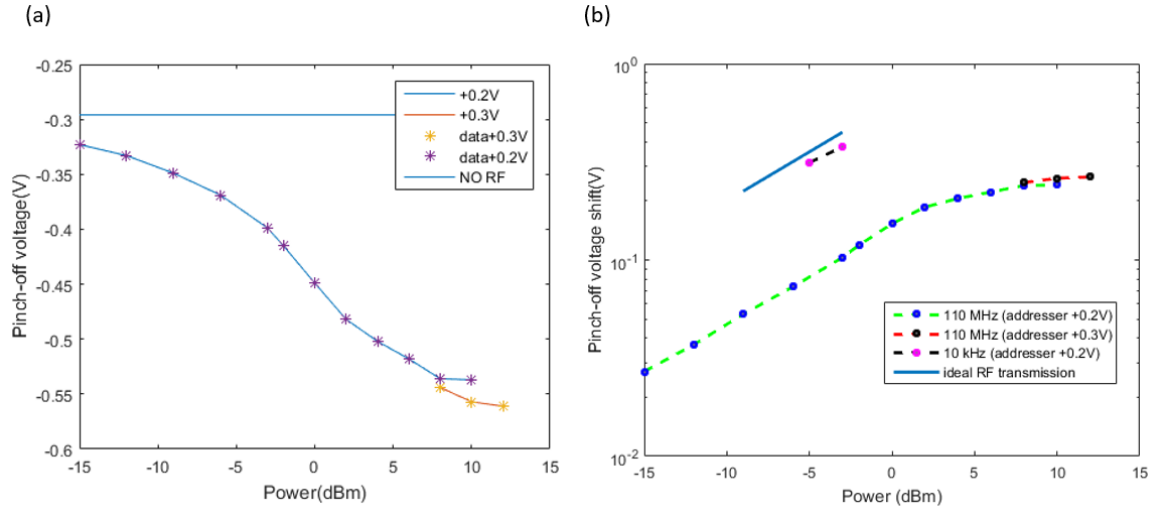

Figure 5.16: Power dependent measurements of pinch-off voltages as a function of RF power at 110 MHz. (a) Pinch-off voltages with RF and without RF applied. (b) Lin-log scale plot of the pinch-off voltage shift when RF is applied.

We do not want to apply too much positive voltage on the addressing gates, and this will cause leakage to the 2DEG. For example if we apply -5 dBm RF signal we would expect the most negative voltage of the AC cycle to be -0.36 V. If we apply +0.5 V to the addressing gates then the addressing gates will be +0.86 V more positive than the 2DEG which will probably damage the device. To protect the device, the maximum positive voltage we apply to the addressing gates is +0.4 V. Using this technique we have got about 300 mV pinch-off voltage shift on the bar gate device (see Fig 5.17). This pinch off shift could be enough to achieve electron pumping.

5.1.5 Rectified current on a single bar gate device

We also did rectified current measurements to see how RF would work with the device which is addressed by the multiplexer. Rectified current measurements are introduced in Chapter 4. We choose two different devices which are Column 16 Row 12 device (2 μm wide) (Fig 5.18) and Column 16 Row 16 device (2 μm wide) (Fig 5.19) to study how the rectified current changes with different RF power and RF frequency signals.

For power dependent measurements, we measured the rectified current against gate voltage for RF amplitudes between -30 dBm and -5 dBm in steps of 5 dBm. We chose a frequency of 110 MHz which we usually use for our pump operation. We took measurements at 0 source-drain voltage bias. Figure 5.18 (a) and Fig 5.19 (a) shows the measured data for RF amplitudes between -20 dBm and -5 dBm. We can see from

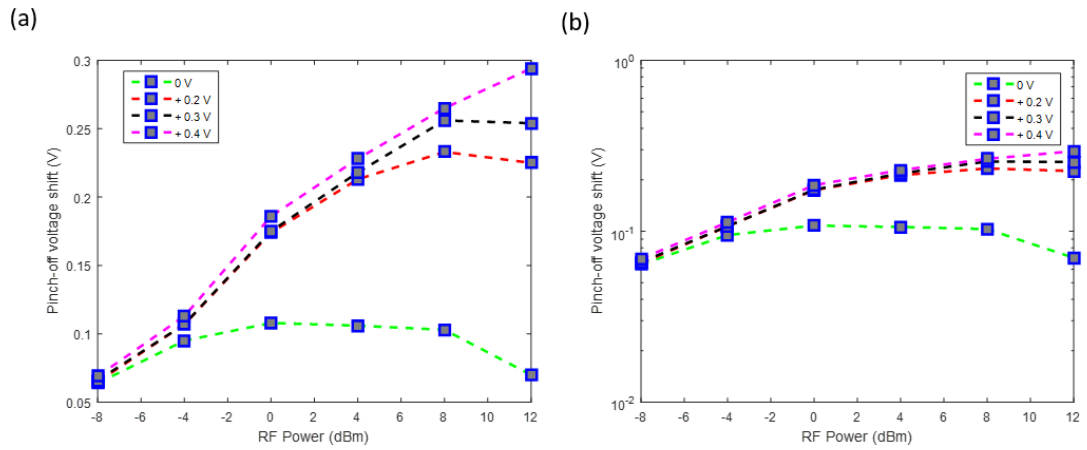

Figure 5.17: The pinch-off shift after 110 MHz RF signal is applied with different RF power. (a) Pinch-off voltage shift with different addressing gate voltages. (b) Lin-log scale plot of the pinch-off voltage shift for different addressing gate voltage applied.

the pictures the data share some features: The rectified current increases with RF power; the pinch-off voltage becomes more negative as the RF power increases; and the rectified current does not change significantly for small RF Power. These features are similar to our results on a single wide-channel electron pump device in Chapter 4.

For frequency dependent measurements, we measured the rectified current against gate voltage for RF frequency from 10 MHz to 110 MHz in steps of 10 MHz. We took measurements at 0 source-drain voltage bias. Figure 5.18 (b) and 5.19 (b) shows the measured data for RF frequency between 10 MHz and 110 MHz. We can see from the pictures the data share some features: The rectified current I_R is not linear with frequency and we believe this is because the attenuation does not change smoothly with frequency (Fig. 5.13). At the frequency such as 90 MHz where the attenuation is small the rectified current is larger.

5.1.6 Rectified current study gates in parallel

We studied the rectified current in parallel bar gate devices. We measured the rectified current in one device for a particular frequency and amplitude (-10 dBm and 110 MHz). Then we use the multiplexer to open a second column so two devices are measured in parallel. Then we open the other channels till 16 channels are open, and we found the rectified current increases as we open more channels (see Fig. 5.20). We also hope that in the future MUX pump array devices we can increase the total pumping current when we open up channels to achieve parallel pumping there. From Fig. 5.20 (b) we

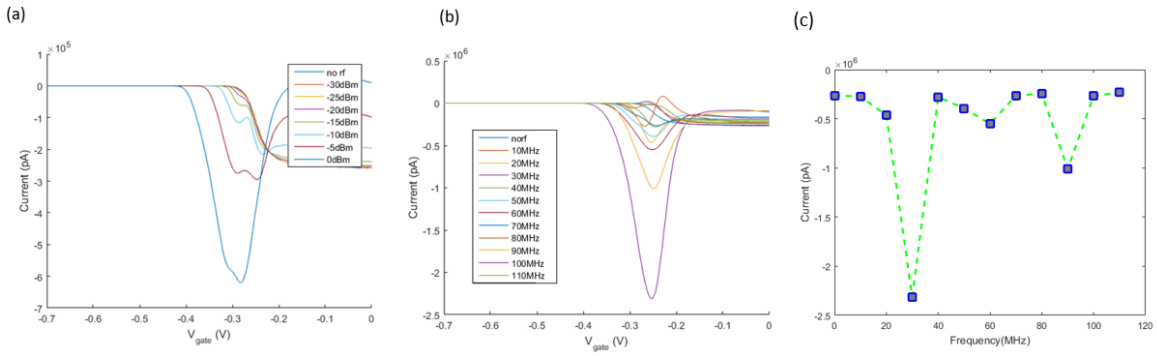

Figure 5.18: Rectified current study on a single bar gate device (Column 16 Row 12) with RF signal applied. (a) Rectified current as a function of gate voltage V_{gate} for different RF power with RF frequency at 110 MHz. (b) Rectified current as a function of gate voltage V_{gate} for different RF frequency with RF power at -10 dBm. (c) The maximum rectified current as a function of frequency with RF power at -10 dBm.

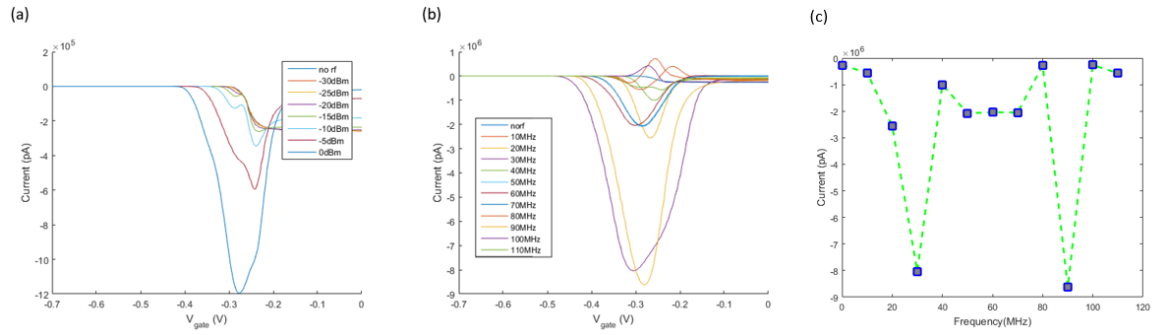

Figure 5.19: Rectified current study on a single bar gate device (Column 16 Row 16) with RF signal applied. (a) Rectified current as a function of gate voltage V_{gate} for different RF power with RF frequency at 110 MHz. (b) Rectified current as a function of gate voltage V_{gate} for different RF frequency with RF power at -10 dBm. (c) The maximum rectified current as a function of frequency with RF power at -10 dBm.

can learn that the rectified current is not proportional to the number of channels that are open.

5.2 New version mux bar gate device

In order to achieve larger pinch-off voltage shifts, we redesigned the multiplexer that modulates the RF signal to reduce the capacitance from the gate to the 2DEG. For the new version MUX bar gate devices we also use wafer W0261, the same wafer as old version MUX bar gate devices. Figure 5.21 shows the comparison between the old version multiplexer and new version multiplexer. In the old multiplexed bar gate

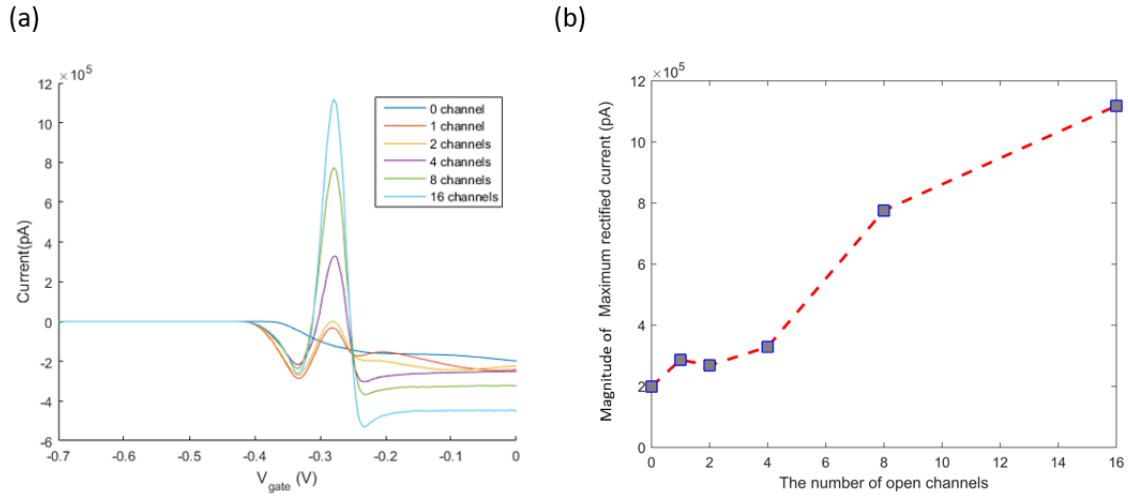

Figure 5.20: Rectified current in parallel in the multiplexed bar gate arrays. (a) Rectified current as a function of gate voltage V_{gate}. (b) The peak rectified current as a function of the number of open channels.

array design, the channel under the addressing gates is 50 μm wide. In the new version multiplexer design, the channel under the addressing gates is reduced to 20 μm wide. The bar gates of different widths are located on the chip (see Fig. 5.22). On this chip we want to study how the pinch-off voltage shift is affected by the distance of the device from the RF source so we have placed bar gates of the same width in different columns.

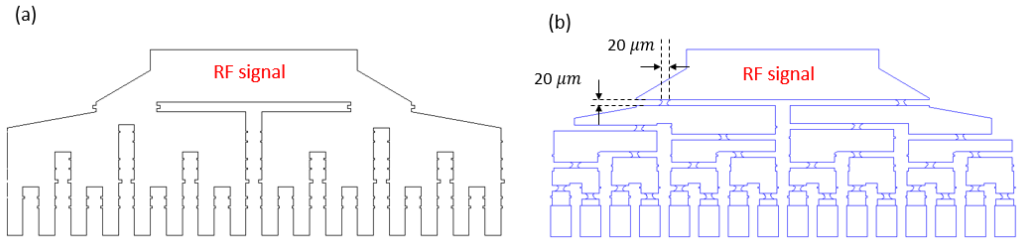

Figure 5.21: Comparison between the old version multiplexer and new version multiplexer. (a) old version multiplexer design, the channel under addressing gates is 50 μm wide. (b) new version multiplexer design, the channel under addressing gates is 20 μm wide.

Bar gate width (μm)

Row 1-16 \ Column 1-16	1	2	3	4	5	6	7	8	9	10	11	12	13	14	15	16
1	0.2	0.3	0.4	0.5	0.6	0.7	0.8	0.9	1	1.1	1.2	1.4	1.6	1.8	2	0.1
2	0.3	0.4	0.5	0.6	0.7	0.8	0.9	1	1.1	1.2	1.4	1.6	1.8	2	0.1	0.2
3	0.4	0.5	0.6	0.7	0.8	0.9	1	1.1	1.2	1.4	1.6	1.8	2	0.1	0.2	0.3
4	0.5	0.6	0.7	0.8	0.9	1	1.1	1.2	1.4	1.6	1.8	2	0.1	0.2	0.3	0.4
5	0.6	0.7	0.8	0.9	1	1.1	1.2	1.4	1.6	1.8	2	0.1	0.2	0.3	0.4	0.5
6	0.7	0.8	0.9	1	1.1	1.2	1.4	1.6	1.8	2	0.1	0.2	0.3	0.4	0.5	0.6
7	0.8	0.9	1	1.1	1.2	1.4	1.6	1.8	2	0.1	0.2	0.3	0.4	0.5	0.6	0.7
8	0.9	1	1.1	1.2	1.4	1.6	1.8	2	0.1	0.2	0.3	0.4	0.5	0.6	0.7	0.8
9	1	1.1	1.2	1.4	1.6	1.8	2	0.1	0.2	0.3	0.4	0.5	0.6	0.7	0.8	0.9
10	1.1	1.2	1.4	1.6	1.8	2	0.1	0.2	0.3	0.4	0.5	0.6	0.7	0.8	0.9	1
11	1.2	1.4	1.6	1.8	2	0.1	0.2	0.3	0.4	0.5	0.6	0.7	0.8	0.9	1	1.1
12	1.4	1.6	1.8	2	0.1	0.2	0.3	0.4	0.5	0.6	0.7	0.8	0.9	1	1.1	1.2
13	1.6	1.8	2	0.1	0.2	0.3	0.4	0.5	0.6	0.7	0.8	0.9	1	1.1	1.2	1.4
14	1.8	2	0.1	0.2	0.3	0.4	0.5	0.6	0.7	0.8	0.9	1	1.1	1.2	1.4	1.6
15	2	0.1	0.2	0.3	0.4	0.5	0.6	0.7	0.8	0.9	1	1.1	1.2	1.4	1.6	1.8
16	0.1	0.2	0.3	0.4	0.5	0.6	0.7	0.8	0.9	1	1.1	1.2	1.4	1.6	1.8	2

Figure 5.22: The bar gate width of each bar gate device on the new multiplexed bar gate arrays.

5.2.1 Pinch-off voltage shift of all 256 gates with radio-frequency signal added

Firstly we measured the pinch-off voltage of the bar gate devices without RF signal and with 110 MHz -10 dBm RF signal applied (see Fig 5.23). The measured pinch-off voltages of the 256 devices are as we expected: the pinch-off voltages of 0.1 μm devices are a bit more negative than the other width devices. The pinch-off voltages of all other devices with 0.2 μm or wider are very similar.

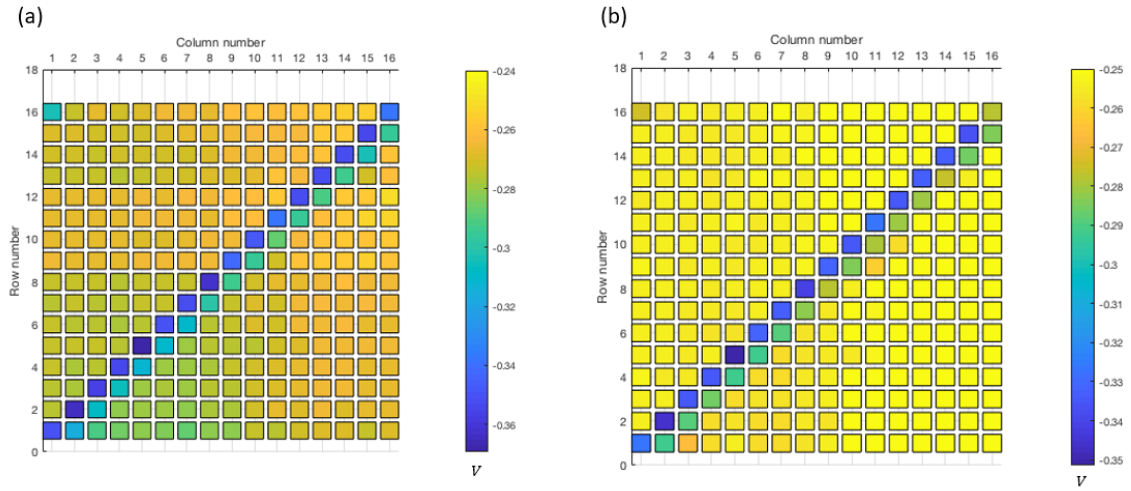

Figure 5.23: (a) Pinch-off voltages of 256 devices with no RF signal applied. (b) Pinch-off voltages of 256 devices with 110 MHz -10 dBm RF signal applied.

We want to study if the distance between the device and the RF source affects the pinch off shift on this new MUX bar gate arrays. Figure 5.24 and Fig. 5.25 show the pinch-off voltage change when 10 kHz -10 dBm RF signal and 110 MHz -10 dBm RF signal is applied respectively. Figure 5.26 shows the pinch off shift for 0.2 μm wide bar gate devices with -10 dBm RF applied on the old and new MUX bar gate arrays. We find there is no clear relationship between the distance and pinch-off shift. The results are very similar for the other width devices which are shown in the Appendix. We can also learn from here that at 110 MHz the pinch off change on the new version MUX bar gate is smaller than that on the old version MUX. This means at high frequency the RF signal is transmitted better in the old version than the new version.

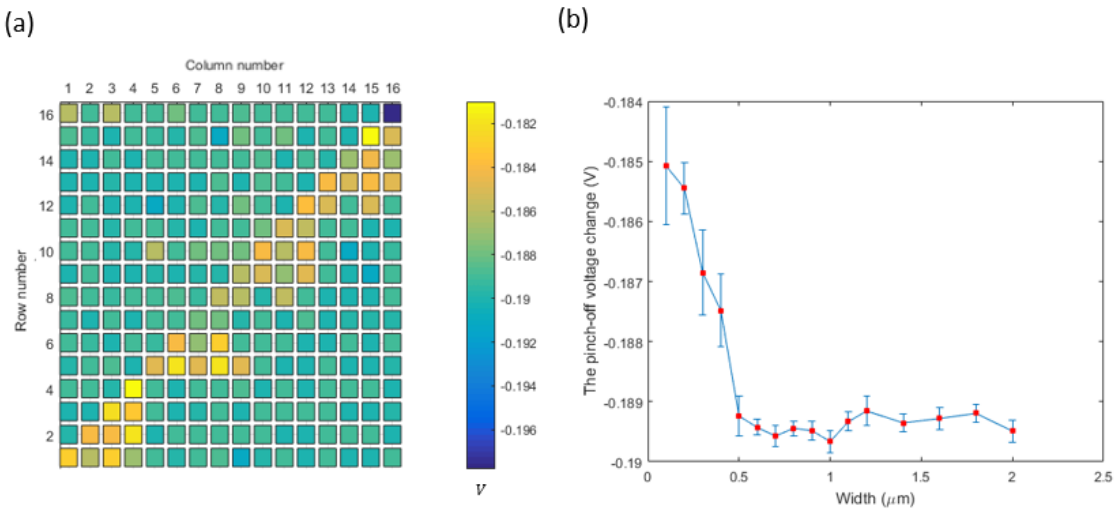

Figure 5.24: Pinch-off voltage change with 10 kHz -10 dBm RF applied on the new MUX bar gate arrays. (a) The colour map of pinch-off voltages change as a function of device position. (b) The average pinch-off voltage change for different gate widths.

We also did frequency-dependent measurements on a single device: -5 dBm RF signal is applied to a 0.1 μm wide bar device (Fig. 5.27). As we expected, the pinch-off shift decreases as the frequency increases. Compared with Fig. 5.11 and Fig. 5.12, we find there are many more dips of the pinch-off shift in the old MUX than the new MUX. It looks like RF transmission in the new MUX does not have as many random variations with frequency as in the old MUX. This may be a benefit of the new MUX design. Also as when we do this measurement, a -3 dBm attenuator was added. This may also reduce the reflections and RF transmission variations.

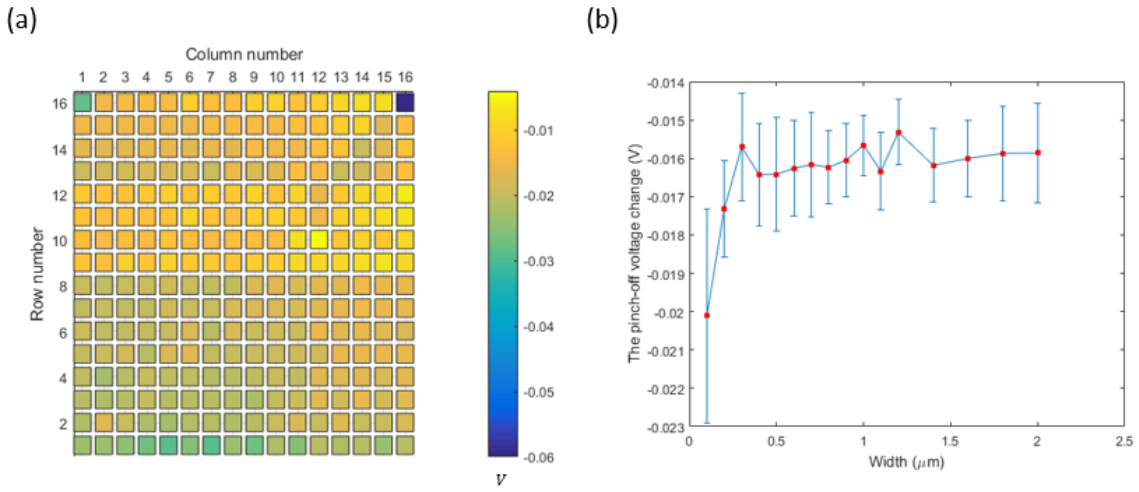

Figure 5.25: Pinch-off voltage change with 110 MHz -10 dBm RF applied on the new MUX bar gate arrays. (a) The colour map of pinch-off voltages change as a function of device position. (b) The average pinch-off voltage change for different gate widths.

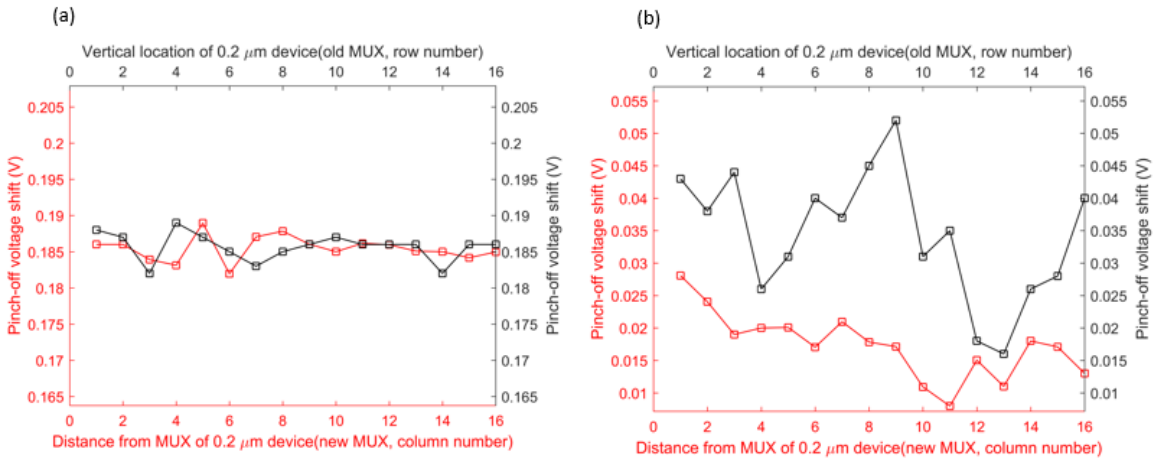

Figure 5.26: Pinch-off voltage change of 0.2 μm wide bar gate devices with -10 dBm RF applied on the old and new MUX bar gate arrays. (a) At 10 kHz frequency. (b) At 110 MHz frequency. The black line is the pinch-off shift as a function of the vertical location of each row on the old MUX bar gate array, the distance between each row is 100 μm. The red line is the pinch-off shift as a function of the distance from RF MUX in the new MUX bar gate array, the distance between each row is 130 μm.

5.2.2 Results: Comparison of the pinch-off voltage shifts between new MUX and old MUX

The most important test of this new version MUX bar gate array is to check the pinch-off voltage shift when we applied RF to see if the RF transmission improves in

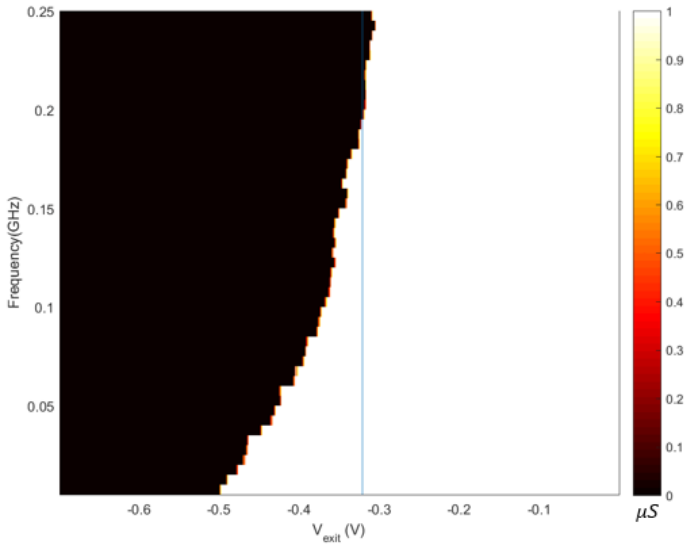

Figure 5.27: Pinch-off voltage as a function of frequency when RF applied at -5 dBm (Column 1 Row 1 device 0.1 μm wide). The blue line is the pinch-off voltage when no RF signal applied.

this new design. Figure 5.28 is the mean pinch-off voltage shift as a function of the bar gate width when -10 dBm RF is applied on the old and new MUX bar gate arrays. The whole 256 devices are similar (see Appendix). We found that the new MUX bar device RF transmission is a bit better than the old bar device at 10 kHz. However, the old device performs better at 110 MHz. We found that the RF transmission of the new design MUX seems does not improve much at high frequency. We will discuss the reason in Subsection 5.2.3.

5.2.3 Discussion: limitations of the new MUX design

On MUX bar gate arrays, the capacitance is mainly made of two parts: the capacitance of the ebeam gates with the 2DEG and the capacitance of the multiplexer addressing gates with the 2DEG. We calculate the ebeam-gate area and multiplexer gate area, which are 1230.3 μm^2 and 200 μm^2 for new MUX (see Fig 5.29). We can see that the area of the e-beam gates is much bigger than the area of the MUX gates on the mesa. There are 16 e-beam gates and 4 multiplexer addressing gates without polyimide in the measurement circuits for one path. So in the new version MUX the total area is $1230.3 * 16 + 200 * 4 = 20485$ μm^2. In the old version MUX design the area of a single multiplexer addressing gate crossing the mesa without polyimide is about 3012.5 μm^2. The ebeam area is the same with the new version MUX. In the old version the

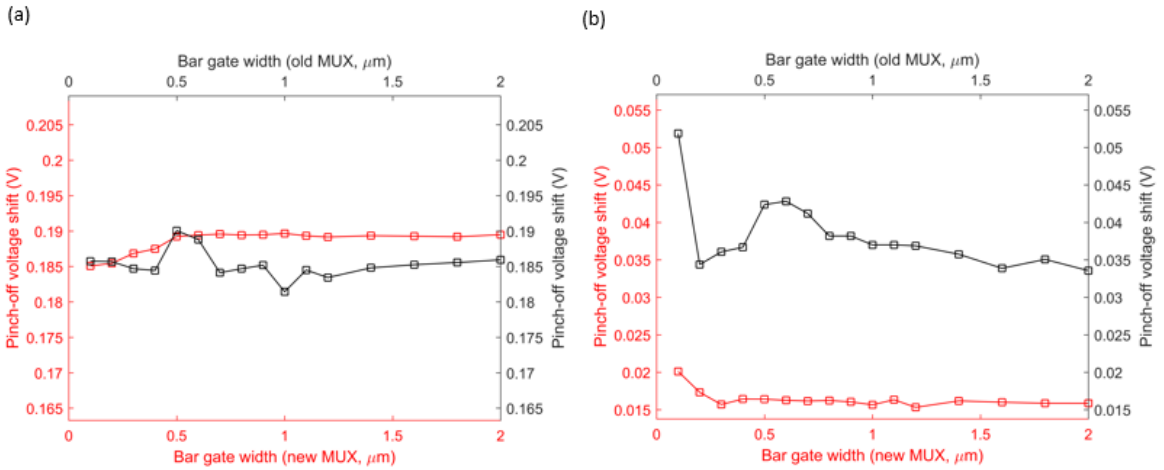

Figure 5.28: The mean pinch-off voltage shift as a function of the bar gate width when -10 dBm RF applied on the old and new MUX bar gate arrays. (a) At 10 kHz frequency. (b) At 110 MHz frequency. The black line is the pinch-off shift on the old MUX bar gate array. The red line is the pinch-off shift on the new MUX bar gate array.

total area is about $1230.3 * 16 + 3012.5 * 4 = 31735\ \mu m^2$. The total area has been decreased by about 35.5% ($(31735 - 20485)/31735 = 35.45\%$). We can see the total area has been decreased a lot, but maybe we need to reduce the total area more in the next version design, particularly in the e-beam gate area. As we decrease the capacitance by reducing the channel width on the MUX where the addressing gates cross, we increase the resistance of 2DEG in the path. This may be another reason why the RF transmission does not improve much.

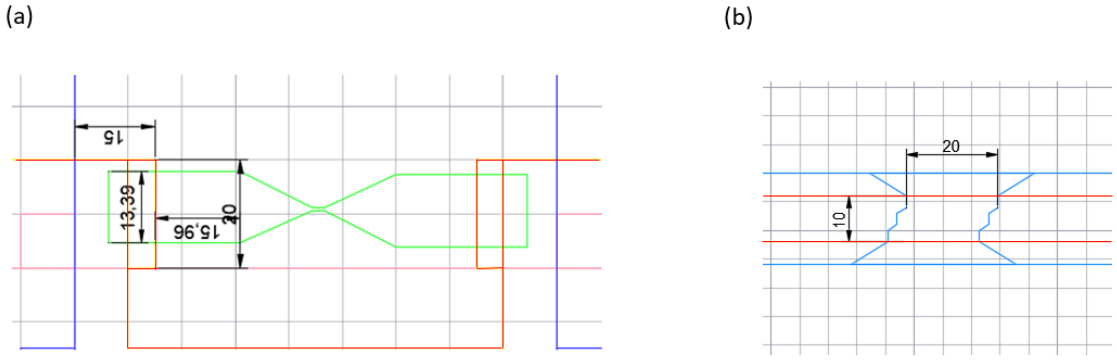

Figure 5.29: Capacitance comparison between ebeam gates and multiplexer gates. (length unit: μm) (a) E-beam gate area. (b) The multiplexer addressing gate area.

5.3 MUX resistance check devices

We also designed the MUX resistance check devices (see Fig 5.30) to check the resistance of some of the paths like when we are using the MUX to choose a particular gate. If we assume the MUX acts as a low pass filter, for this device we can measure the resistance and the RF power transmission through multiplexer to calculate the capacitance of the multiplexer. The MUX resistance check device is exactly the same multiplexer design as we use on the new version MUX bar gate device introduced in the last section.

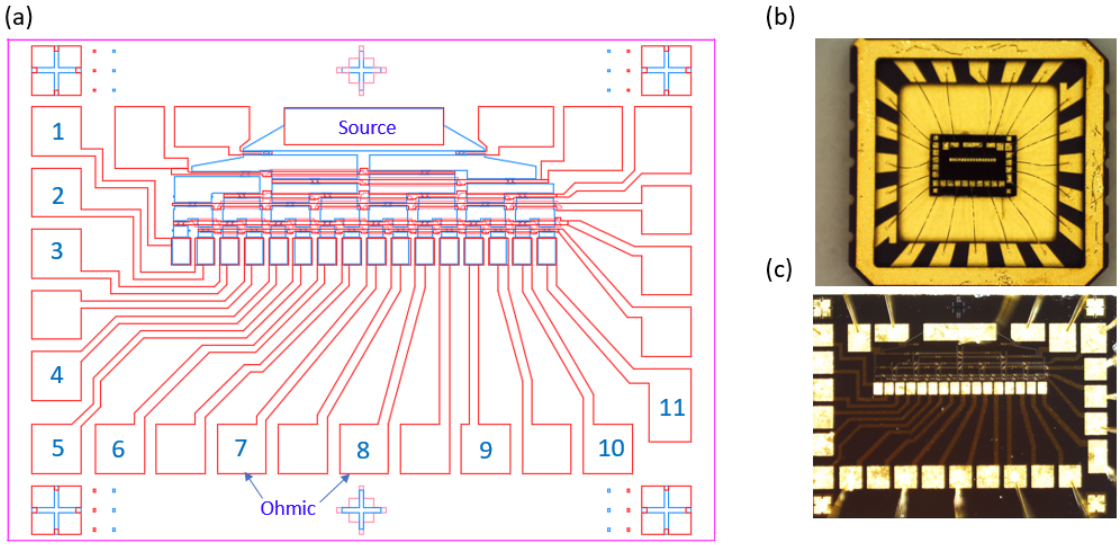

Figure 5.30: MUX resistance check device. (a) The AUTOCAD design mask. The number labelled is the current path we measured. (b) The optical microscope image of the device bonded in an LCC package. (c) The optical microscope image of the device.

Firstly we use the gates to select just one path though the MUX and measure the conductance through that path. Table 5.2 shows the results. Here as the wires of sample holder are limited, we have only measured the conductance of 11 paths. There is one small ohmic contact (Drain) is broken on the first device (Table 5.2).

We think it will be useful to measure the resistance as when we use the MUX to choose a particular gate. We measure the conductance when we biased the four levels of addressing gates one by one. The results are shown in Fig 5.31 (a). We found locking the addressing gate did not make very much difference to the conductance, because the selected path is protected by the polyimide from being depleted by the negative voltage on the addressing gates.

	Conductance (μS)										
Path	1	2	3	4	5	6	7	8	9	10	11
Device 1	1568	1658	919	913	1675	1692	1545	0	1500	1578	1542
Device 2	1513	1511	1610	1173	1034	1200	1440	1531	1288	1311	1186

Table 5.2: Conductance value of MUX resistance check devices, current paths are shown in Fig 5.30. The conductance was measured when the sample bonded with RF sample holder for two devices.

We also bond a sample in the RF sample holder, with the large ohmic contact (Source) and one of the small ohmics contact (Drain) bonded to the RF lines, then we do an S21 measurement using a vector network analyser (S21 is the forward voltage gain of 2-port networks measurement). We measure the S21 with all the gates at 0 V, and then measure it again when we use the gates to bias the MUX addressing gates one level by one level to pinch off all the paths except the one we are measuring [see Fig 5.31 (b)]. This quantifies how the GaAs MUX can transmit RF power.

(a)

Gates locked	Conductance (μS)
No gates	1430
First level gates	1396
Second level gates	1384
Third level gates	1398
Fourth level gate	1390

(b)

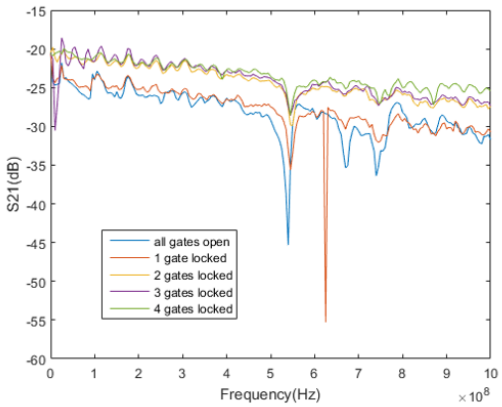

Figure 5.31: MUX resistance check device RF transmission measurements with gates locked one by one. (a) Conductance with gates locked one by one measured using a Lock-in amplifier at 77 Hz. (b) S21 parameter measurements with gates locked one by one measured using a VNA.

From the results, we can learn that locking the addressing does not affect much about the resistance when a path is selected. The transmission is about -21 dB at 100 MHz with 4 gates biased, so about 10% of the voltage amplitude is getting back to the receiving port of the VNA. In all the data (no gates, 1 gate biased, 2 gates biased, 3 gates biased and 4 gates biased) we can see the transmission decreases as the frequency increases. We believe this is because the MUX bar gate device acts like low-pass RC filter. We also found from the S21 with all addressing gates open and 1 addressing gate

biased, that the attenuation is bigger than with more gates biased. This is because when all that addressing gates are open or just one addressing gate is locked, there is still some capacitance between the un-selected paths and the addressing gates, so some RF signal will go to ground through these paths, which are connected to DC measurement wires that have a large capacitance (>100 pF)to ground. However, when we biased the 4 addressing gates, the electrons under these addressing gates will be depleted and the capacitance under them drops to zero, so the RF signal can only go to the selected path.

5.3.1 Capacitance calculation

We model the VNA measurement circuit as in Fig 5.32 [55], where $G(\omega)$ is the transfer function, the source impedance (R_S) and load impedance (R_L) are both 50 Ω. We simplified our MUX resistance check device as a first order RC filter in Fig 5.32 (b), where R_{SO} is the resistance from the source ohmic, R_{2DEG} is the 2DEG resistance through the current path, R_{DO} is the resistance from the drain ohmic, C is the capacitance of the MUX addressing gate.

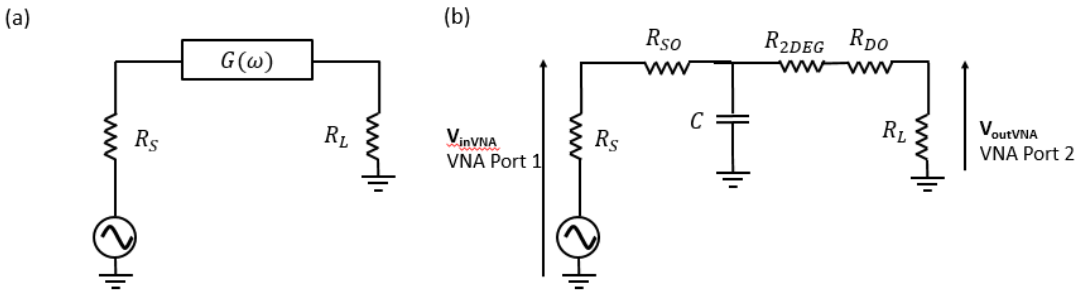

Figure 5.32: Model of the measurement circuits. (a) The MUX resistance check device can be described as transfer function $G(\omega)$ with a load and source impedance. (b) Model when we test RF transmission using VNA on a MUX resistance check device.

The VNA measurement circuits is as Fig 5.32 (b). We can get

$$V(out\text{VNA})/V(in\text{VNA}) = \frac{Z_0}{R_{SO} + R_X + j\omega C R_{SO} R_X} \tag{5.1}$$

Here $Z_0 = R_L = 50$ Ohms is the VNA load impedance, $R_X = R_{2DEG} + R_{DO} + Z_0$. In the VNA measurements, S-parameters describe the input-output relationship between ports in the electrical system and S_{21} in dB can be described as follows

$$S_{21} = 20log(|V(out\text{VNA})/V(in\text{VNA})|) \tag{5.2}$$

We can learn from Fig 5.31 (b), with four addressing gates biased at 10 kHz, $S_{21} = -20.69$dB. We assume at 10 kHz the capacitance in Fig 5.31 (b) has infinite impedance. Then we can get from Equation 5.2, the total resistance $R_{SO} + R_{2DEG} + R_{DO} = 491\ \Omega$. As in the real MUX device, how this total resistance is divided into R_{SO}, R_{2DEG} and R_{DO} divided is very complex, here we just assume the capacitor divide the resistance half by half, so we assume that $R_{SO} = R_{2DEG} + R_{DO} = 419/2 = 209.5\ \Omega$ and $R_X = R_{2DEG} + R_{DO} + Z_0 = 209.5\ \Omega + 50\ \Omega = 259.5\ \Omega$. Then we can put the known R_{SO} and R_X into Equation 5.2, the only unknown variable is the capacitance C. We use Matlab Curve Fitting Tool box to fit this equation with the 4 gate curve in Fig 5.31 (b), we can calculate the capacitance $C = 1.93 * 10^{-12}$ F. Then we insert the calculated capacitance $C = 1.93 * 10^{-12}$ F into Equation 5.2 to model the S_{21} as a function of frequency and compare the simulation with the measurement results in Fig 5.33. We can learn that the simulation S21 fit the measurement data well. We also tried some other ways of dividing the total resistance $R_{Total} = R_{SO} + R_{2DEG} + R_{DO} = 491\ \Omega$ such as the ohmic resistance is inversely proportional to area or the width connected to 2DEG, but we find that what matters is only the total resistance and the way dividing the total resistance does not affect the fitting very much.

Besides, we also calculate the capacitance from the overlap area of the 2DEG and MUX addressing gates. We consider the multiplexer addressing gate as parallel-plate capacitor, then the capacitance can be calculated as

$$C = \varepsilon A/d \tag{5.3}$$

here, $\varepsilon = 12\varepsilon_0$ because of 33 % AlGaAs [10]. The area A can be the get from that $20 \times 10 = 200\mu\text{m}^2$, the separation between the surface and 2DEG is $d = 90$ nm. Then we can get the capacitance for one addressing gate without polyimide is 2.361×10^{-13} F. For our measurement circuits, there are four such capacitors in parallel, and the total capacitance will be $C = 9 \times 10^{-13}$ F. We can learn that this is a bit smaller than we calculated from the VNA measurements. We think this is because in the real measurement circuits, the total capacitance also includes the wire capacitance, probe capacitance and sample holder capacitances.

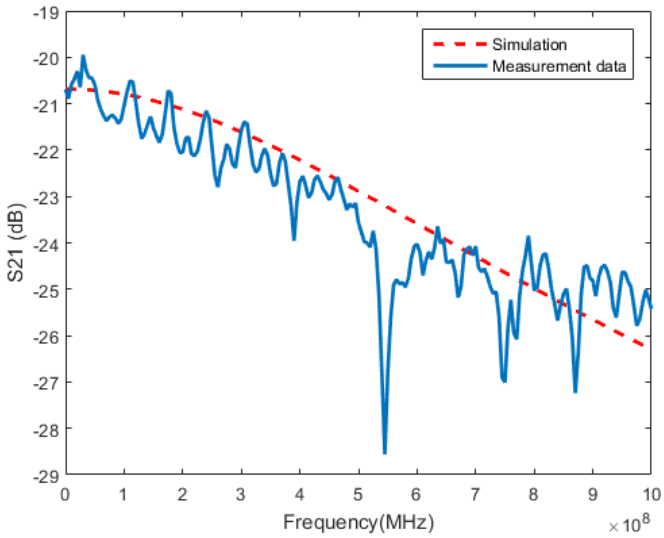

Figure 5.33: Comparison of the measurement data (blue solid line) and simulation (red dashed line) of the VNA measurements.

5.4 Summary

In this chapter, we began with a statistical study of multiplexed bar gates. We have studied the pinch-off voltage and maximum transconductance dG/dV_g of all 256 gates. We find the 0.1 μm wide bar gate is different from the 0.2 μm wide bar gate or wider gates: more negative voltage is needed to pinch off 0.1 μm wide bar gates and for maximum transconductance dG/dV_g, 0.1 μm wide bar gates give a smaller value than the other width devices. This is because 0.1 μm is comparable with the 2DEG depth. With radio frequency signal applied the pinch-off voltage shift of all 256 gates has been analysed. We find that device location on the chip and the distance between the device and RF source do not have a strong correlation with the pinch-off voltage shift. The pinch-off voltage shift represent RF power transmission. Besides, we choose several single devices in the devices array to do AC measurements and DC measurements with RF applied. We obtain about a 300 mV pinch-off voltage shift on the bar gate device. In order to achieve high RF transmission, we need to initially shift the addressing gates to a positive voltage (for example +0.4 V), before we apply zero voltage for DC measurements. Using the advantage of multiplexer we have also studied the rectified current of the bar gate devices in parallel. We demonstrate that the rectified current increases as we open up channels. We redesigned the multiplexer that modulates the RF signal to reduce the capacitance. We compare the RF transmission between the old MUX and new MUX. However, we find that the new MUX does not improve

much at high frequency. We discuss the limitations of the new MUX design and find that the capacitance of the MUX addressing gate is not a limiting factor. Finally, we design MUX resistance check devices to measure the resistance of the multiplexer and calculate the capacitance of the multiplexer assuming the MUX bar gate devices act like a low-pass filter with capacitance of 1.93 pF. For future MUX pump arrays design, it is important to decrease the area of the ebeam gates which makes up a big part of total capacitance.

6

Single-electron pump with MUX-style polyimide

To make multiplexed pump arrays, we need connecting gates reaching across all the mesa channels to the pumping gates of each pump device. When negative voltages are applied to the connecting gates to define the electron pump, these gates have to be insulated from the mesa underneath to avoid pinching off the conduction. Therefore gate insulators are required in the multiplexed electron pump array design, so it is important to demonstrate that they are compatible with the single-electron pump devices.

In this chapter we demonstrate electron pumping in a single-electron pump device in which the gates extend across the entire GaAs channel, and are insulated from the GaAs channel by a polyimide layer as required in the multiplexed design. Also we have studied how the variations in the design of the electron pump, such as dot size, and barrier thickness affects the pumping current.

6.1 Introduction

The semiconductor tunable-barrier quantum-dot single-electron pump was first demonstrated by Blumenthal *et al.* in 2007 [2]. This device was made up of a 500 nm narrow etched quantum wire [Fig. 6.1 (a)] and three metal gates. Negative voltages were applied to the entrance gate marked L and exit gate marked R to define a quantum dot. RF signals $V_L^{a.c.}$ and $V_R^{a.c.}$ were also added to these two gates by bias tees to modulate the dot potential. With the phase difference of the $V_L^{a.c.}$ and $V_R^{a.c.}$ set to π, an integer number of electrons travels through the quantum dot per AC cycle and gigahertz pumping was observed. The potential change of the quantum dot during one AC cycle is described in Fig 6.1 (b). Kaestner *et al.* simplified the pump measurement using two pump gates by just applying negative DC voltage to the exit gate to achieve pumping in 2008 [56]. Since then, only one RF signal is applied to the entrance gate to demonstrate pumping. On these initial GaAs electron-pumping devices, the quantum wires were defined by a sub-micrometer wide and the gates were all straight-line Ti/Au finger gates. Some research groups still keep this device design [57]. However, in order to avoid the sub-micrometer channel etching and increase the device yield, the National Physics Laboratory (NPL) changed the quantum wire etching to 2 μm and used gates to define a quantum dot [3, 58]. An NPL electron pump device is shown in Fig. 6.2.

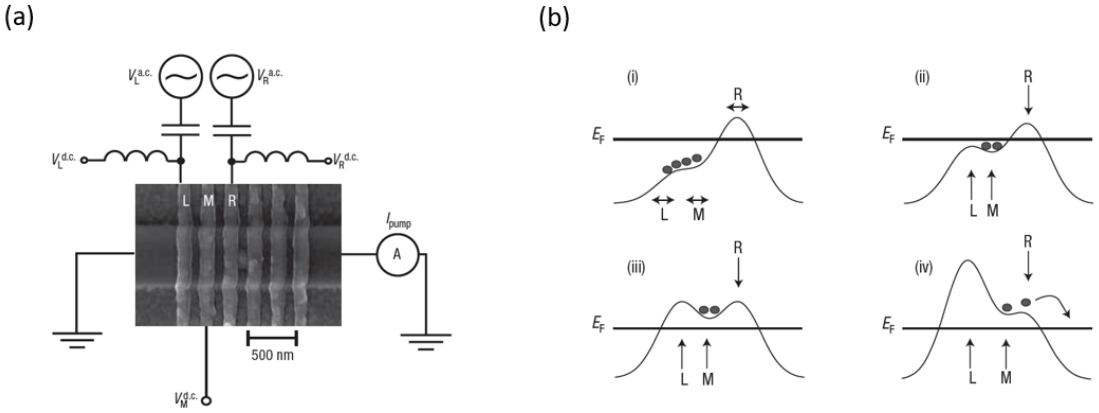

Figure 6.1: (a) SEM image of the tunable-barrier quantum dot single-electron pump demonstrated by Blumenthal *et al.* (b) A schematic of the potential change during one AC cycle. Taken from [2].

Figure 6.3 describes the pumping mechanism. Figure 6.3 (a) presents the pumping current as a function of the entrance gate voltage $V_{entrance}$ and exit gate voltage V_{exit} when RF is applied to the entrance gate [51]. Here n_c is the number of the electrons

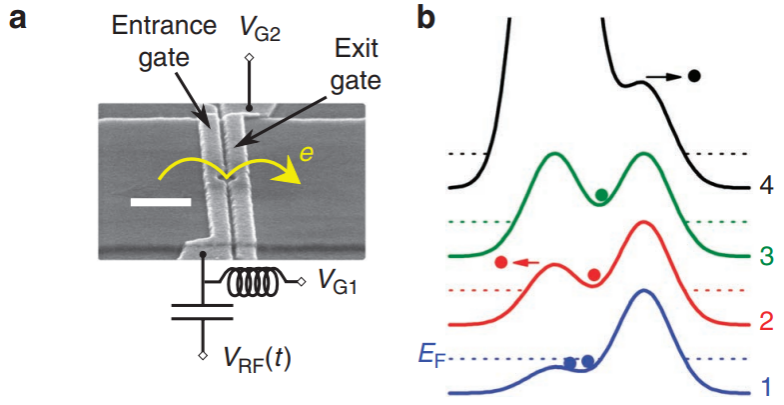

Figure 6.2: (a) SEM image of an NPL single-electron pump. (b) A schematic of the potential change during one AC cycle, only one RF signal was used. Taken from [3].

captured in the quantum dot and n_e is the number ejected to the drain. The plateaus in the pumping current occur at $I = n_e e f$. In region (a), as the DC voltage applied on the entrance gate $V_{entrance}$ is too negative there is always a barrier between the source and quantum dot. No electrons can be captured or ejected in this case [Fig. 6.3 (b) a]. In region (b), the DC voltage on the entrance gate and exit gate are both set so that all the electrons captured from source are ejected in to the drain [Fig. 6.3 (b) b]. In region (c), the negative voltage set on the entrance gate is a bit smaller than the perfect situation, so the electrons captured cannot all be ejected to the drain [Fig. 6.3 (b) c]. In region (d), the DC voltage on the entrance gate is not negative enough. The electrons are captured, but the entrance gate voltage never goes negative enough to push the quantum dot potential above the exit barrier height. One cannot observe pumping in this situation [Fig. 6.3 (b) d]. The dashed lines in Fig 6.3 (a) are the edges between regions where the relationship between n_c and n_e are different.

6.2 Device and electrical setup

As the single-electron pump is sensitive to the wafer selection and design parameters, it is difficult to observe pumping if these are not optimal. We want to test if the quantised pumping could still be observed with a polyimide layer added to isolate the mesa from connecting gates. The polyimide layer is deposited between the wafer surface and connecting gates. Figure 6.4 shows a schematic of the single-electron pump with polyimide added from our design. We begin by designing some pumps with narrow channels which are similar to the NPL single-electron pump design. Figure 6.5 shows the optical image and SEM image of single-electron device with polyimide

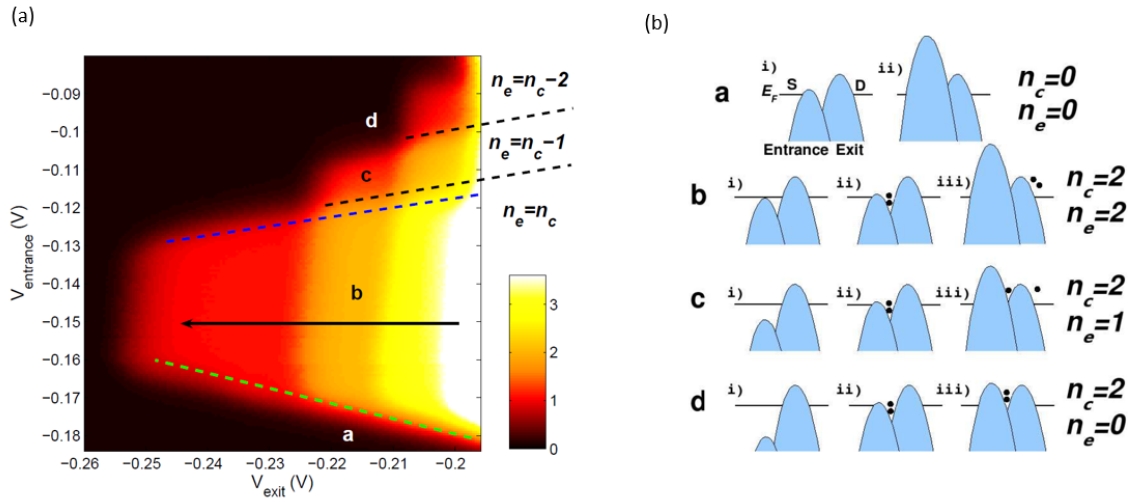

Figure 6.3: (a) Colour map of the pumping current as a function of the entrance gate voltage $V_{entrance}$ and exit gate voltage V_{exit} when RF applied to the entrance . (b) Potential schematic of different regions in pump current map. Taken from [51].

added. The radius of dot size, barrier thickness and gap between the gates are the three most important parameters of the single-electron pump design [Fig 6.5 (c)]. Here we begin with W0546 wafer and design parameters (dot size: 150nm, tunnel barrier: 100 nm, gap: 50 nm) that matched those used previously by Dr Joanna Waldie to observe pumping. We study how the design parameter variations would affect the charge pumping performance.

1. Pump gates design: we have two different sizes of the dot radius (130 nm and 150 nm) and tunnel-barrier width (85 nm and 100 nm). For all devices the gap between the gates is 50 nm. Based on these designs, there are four combinations of pump gate designs.

2. Channel etch design: we have two different channel-etch designs E1 and E2 shown in Fig. 6.6. From NPL's experience of electron-pump design [3], we learn that if the RF gate is too close to the source 2DEG of the pump, the capacitive coupling between the RF gate and the source increased, which affects the accuracy of pumping, especially at high magnetic field. So for the E1 design, we made the distance between the entrance gate and the 2DEG larger, to give better pumping performance. But for this design, we need to increase the channel etch area which makes the channel even narrower. This is a bit risky for etch fabrication, because at the edge of the narrow channel the electrons will be depleted after etching. The narrow channel easily becomes non-conducting if the entrance and exit of channels are too narrow. Therefore we also

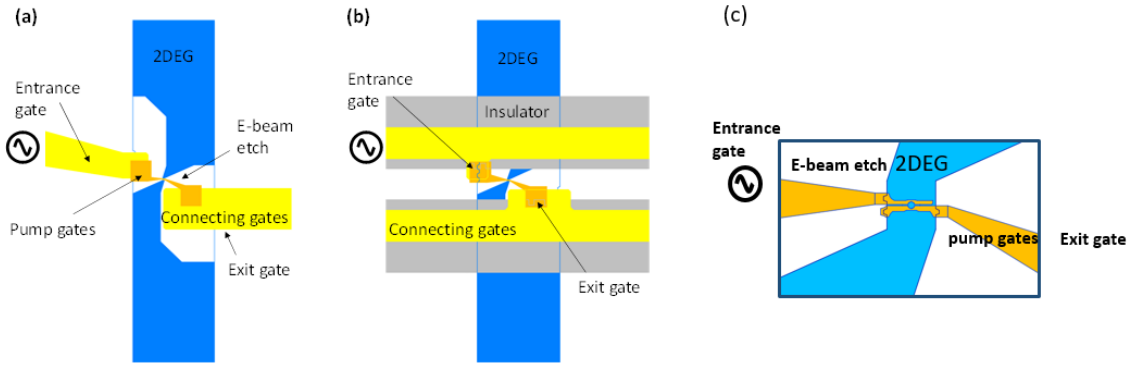

Figure 6.4: (a) Single-electron pump without polyimide. E1 design. (b) Single-electron pump with polyimide added, grey is polyimide. E1 design. (c) Zoom-in view of the narrow-channel area. We apply RF signal and DC voltage to the connecting gates through the multiplexer to reach the pumping gates if we make MUX single-electron pump arrays in the future. The narrow-channel 2DEG is 2 μm. (a) and (b) were drawn by Dr Joanna Waldie.

make an E2 design, whose entrance and exit part of the narrow etching channel are wider, as a comparison.

3. Order of fabrication: for some of the devices we deposit the e-beam gates before spinning the polyimide layer. The fabrication order for these devices is mesa, ohmic contacts, Ebeam etch, Ebeam gates, polyimide and optical connecting gates. We have one concern about this fabrication order: the polyimide needs to be baked in a high-temperature tube furnace (270 °C), and we want to know if this high temperature would damage the e-beam gates or not. For the other devices we deposit the e-beam gates after finishing spinning the polyimide layer and depositing the connecting gates. The fabrication order is mesa, ohmic contacts, Ebeam etch, polyimide, optical connecting gates and Ebeam gates. However, we also have one concern about this fabrication order: with the polyimide (1000-1100 nm thick) already on the surface the PMMA resist for the e-beam gates might not spin uniformly and the quality of the e-beam lithography might be affected. We want to find which is a better fabrication order to make the electron pump with polyimide.

A schematic of the measurement circuit is shown in Fig. 6.7. The measurement methods are described in more detail in chapter 3. All these measurements we carried out at 4 K in the electron-pump dip station at the Cavendish Lab. We tested the measurement uncertainty associated with measurement setup: for example in Fig 6.8 we fix the entrance gate voltage to a certain value in the middle of the first plateau

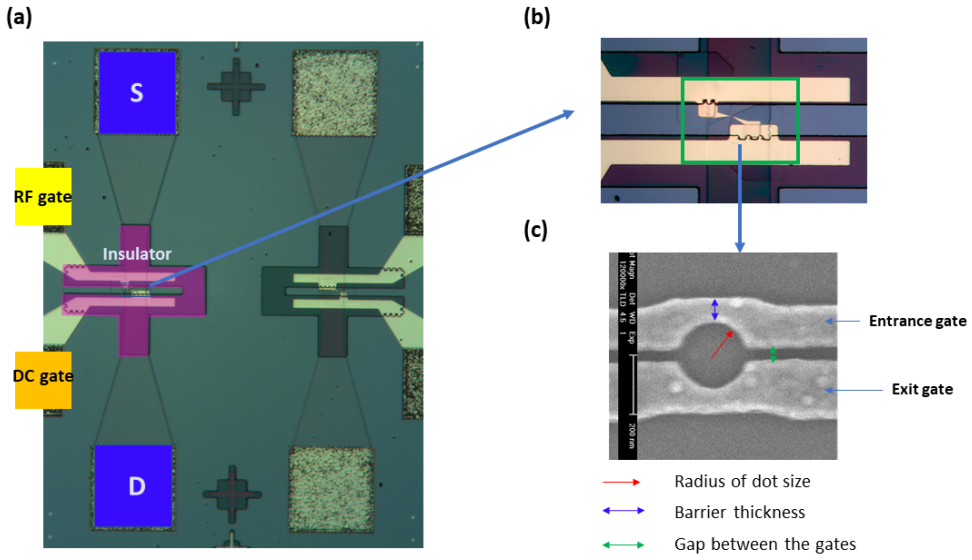

Figure 6.5: Single-electron device with polyimide added. (a) Optical image of the single-electron pump with polyimide devices, the blue area is source and drain, the purple area is insulator, dark yellow area is the exit gate and light yellow area is the Entrance gate. (b) Optical image of the pumping gates area. (c) SEM image of the pump gates. Three most important parameters of a single-electron pump design: radius of dot size, barrier thickness and gap between the gates are labelled. (b) and (c) are taken by Dr Joanna Waldie.

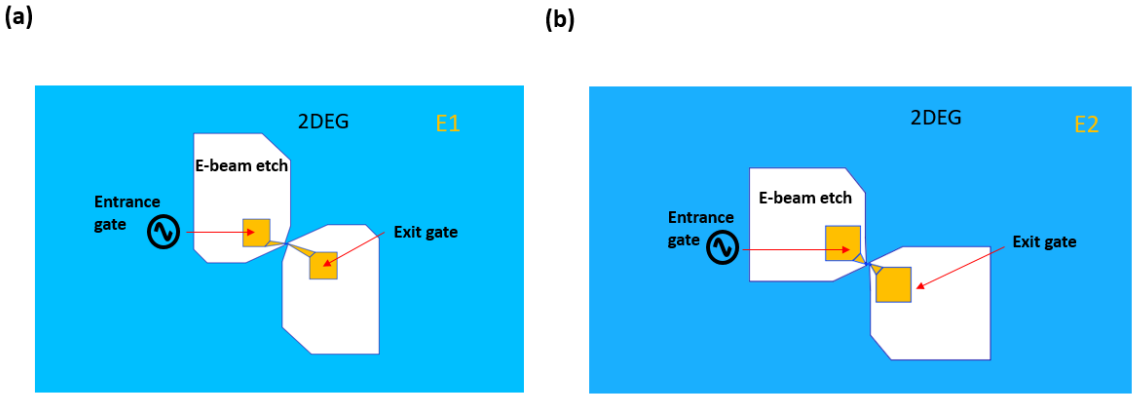

Figure 6.6: The schematic of channel etch design. (a) E1 design. (b) E2 design. The distance between the entrance gate to 2DEG of the E1 design is larger than the E2.

$V_{entrance} = -0.34$ V. Then we change the exit gate voltage V_{exit} from the most negative voltage to the smallest negative voltage in steps of 0.001 V. On each step we stop

for 20 seconds to measure the current (here 47 points are recorded for each V_{exit}). Then we calculate the average current [Fig. 6.7 (b)] and random uncertainty of the average current [Fig 6.7 (c)]. Here we calculate the random uncertainty using the standard deviation of the measured data points (47 points) divided by the square-root of the number of data points. The sources of noise include equipment noise, gate voltage, vibrations [15]. We can learn from Fig. 6.7 (c) that the random uncertainty changes with V_{exit}: in the plateau regions the uncertainty is much lower than in the riser regions. This is because in the plateau regions the pump always transports the same integer number of electrons (such as N). However in the riser regions the number of the pumped electrons vary, for example sometimes it will pump $N-1$ electrons and sometimes it will pump N electrons. We can learn from the in the plateau areas, the current error is ∼0.005 pA. At 110 MHz, the total pumping current is 17.6 pA, and the error rate of this measurement set up is $0.005/17.6 = 2.8409 * 10^{-4}$.

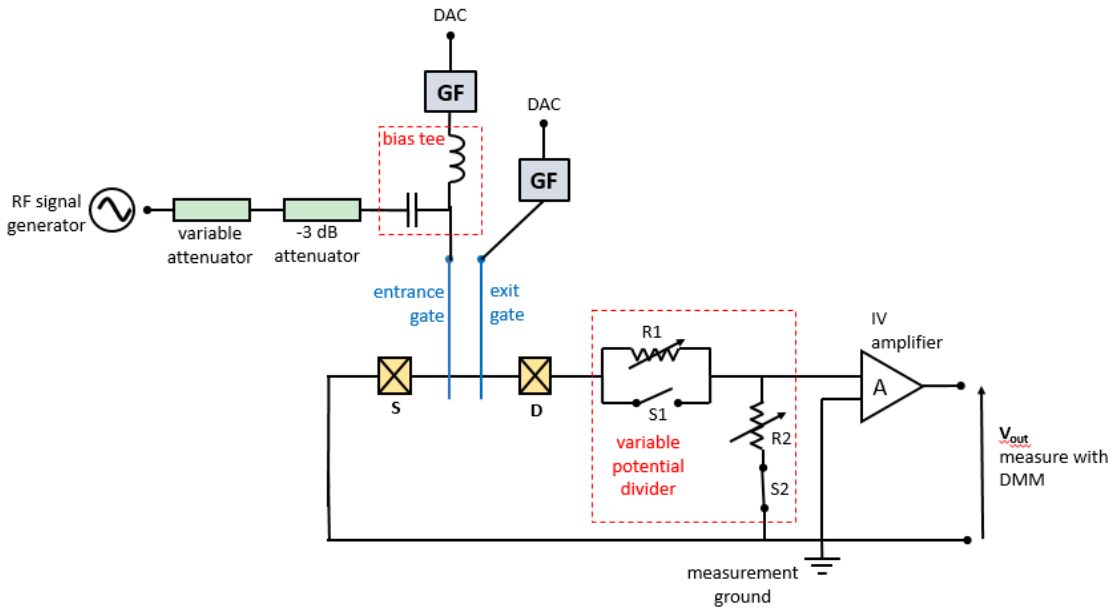

Figure 6.7: A schematic of the measurement setup for a single-electron pump device with polyimide added. GF is a low-pass RC filter with RC = 10 ms to reduce DC voltage spikes, DMM is the digital multimeter to measure the voltage output of the IV amplifier. The 3 dB attenuator is used for part of the measurements.

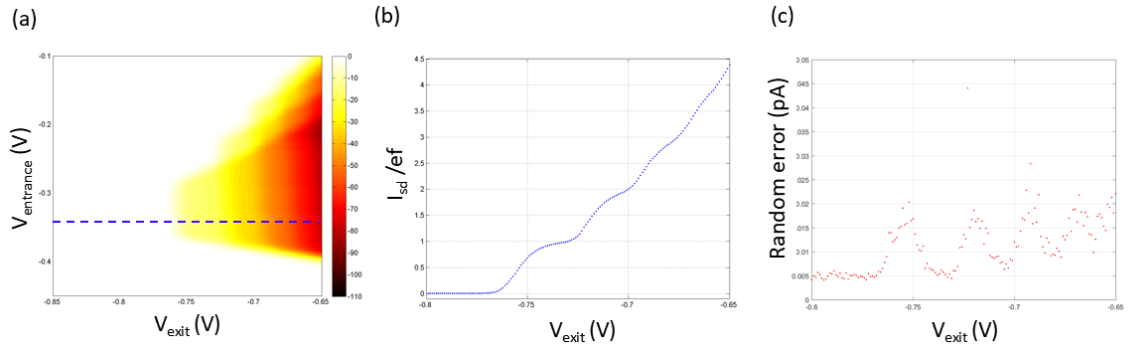

Figure 6.8: (a) The pumping current colour map as a function of $V_{entrance}$ and V_{exit}. (b) The average current with entrance gate voltage fixed in the middle of the first plateau $V_{entrance} = -0.34$ V. (c) The random uncertainty of average current. The device is E1 channel etch, dot radius 130 nm, tunnel barrier width 100 nm and with polyimide deposited after e-beam gates.

6.3 Results: quantised charge pumping with several design variations

In the last section, we presented several design variations of electron-pump designs with polyimide added. In this section, we present the quantised charge-pumping performance with these design variations. We have tested one device without polyimide (the experiment was done by Dr Joanna Waldie). We use this device as a comparison to the devices with polyimide added. We have measured 14 devices with polyimide added, and we observe charge pumping in 7 devices. The pumping yield is therefore 50%. For non-working devices: one device did not conduct at room temperature; two devices did not conduct at 4K while conducting at room temperature; four devices' pump gates did not work, which may have been because of ESD damage during bonding or measuring. The design parameters of the 7 working devices are shown in Table 6.1.

We find that for different pump designs, we need to apply different RF power to observe a clear charge pumping map like that in Fig 6.3 (a). In following part we want to discuss if there is a relation between the required RF power to observe pumping and the design parameters such as dot radius and tunnel barrier width.

Number of Devices	Channel Etch Type	Tunnel Barrier Width (nm)	Dot Radius (nm)	Poly After/Before Ebeam gates
1	E1	85	130	After
2	E1	100	130	After
3	E1	100	150	After
4	E2	100	150	Before
5	E1	100	130	After
6	E2	100	130	Before
7	E2	85	150	Before

Table 6.1: The parameters of the working pump with ployimide devices. Device 1-3 are tested without 3 dB attenuator added to measurement setup. Device 4-7 are measured with 3 dBm attenuator. The measurement setup is shown in 6.7.

6.3.1 Definition of required RF power to observe charge pumping

When we do pumping measurements, after we set the sweeping range of the entrance gate and exit gate, we slowly increase the RF power (normally in steps of 1 dBm) until we observe a clear pumping map. Figure 6.9 shows how the pumping map becomes clearer as the RF power is increased, the RF power in Fig. 6.9 (a) to (d) is -5 dBm, -4 dBm, -3 dBm and -2 dBm. The device has the E1 channel etch, dot radius 130 nm, tunnel barrier width 85 nm and polyimide deposited after e-beam gates. The RF frequency is 110 MHz. The sweeping rate of the exit gate voltage is the same for these four measurements, which means that the resolution of the pumping map will only depend on the performance of the pump and whether is pumping the same number of electrons over a range of voltages. For all four plots, the range of entrance gate voltage is set to -0.25 V to 0.05 V and the range of exit gate voltage is set to -0.75 V to -0.5 V to help comparisons. In Fig 6.9 (a) and (b) it is hard see the pumping plateaus. In Fig 6.9 (c) we can see there are some clear pumping plateaus, but the first plateau area ($I = ef$) is not well defined. In Fig 6.9 (d) the first plateau area is also well defined. In this work we look for the RF power that must be applied so that all the pumping plateaus on the pumping current colour map can first be defined, and we regard this as the 'required RF power' to observe charge pumping.

We want to study whether the RF frequency will affect the required RF power needed to realize charge pumping. Figure 6.10 shows how the pumping maps change as the applied RF frequency increases. Here we fix the RF power at -2 dBm. The pumping plateaus are well defined at 110 MHz in Fig 6.10 (a). As the RF frequency increases, the pumping plateaus become less clear. We believe this is because the transmitted RF power is attenuated as frequency increases, and therefore larger RF power is needed to observe pumping. Figure 6.11 plots the pinch-off voltage for low-

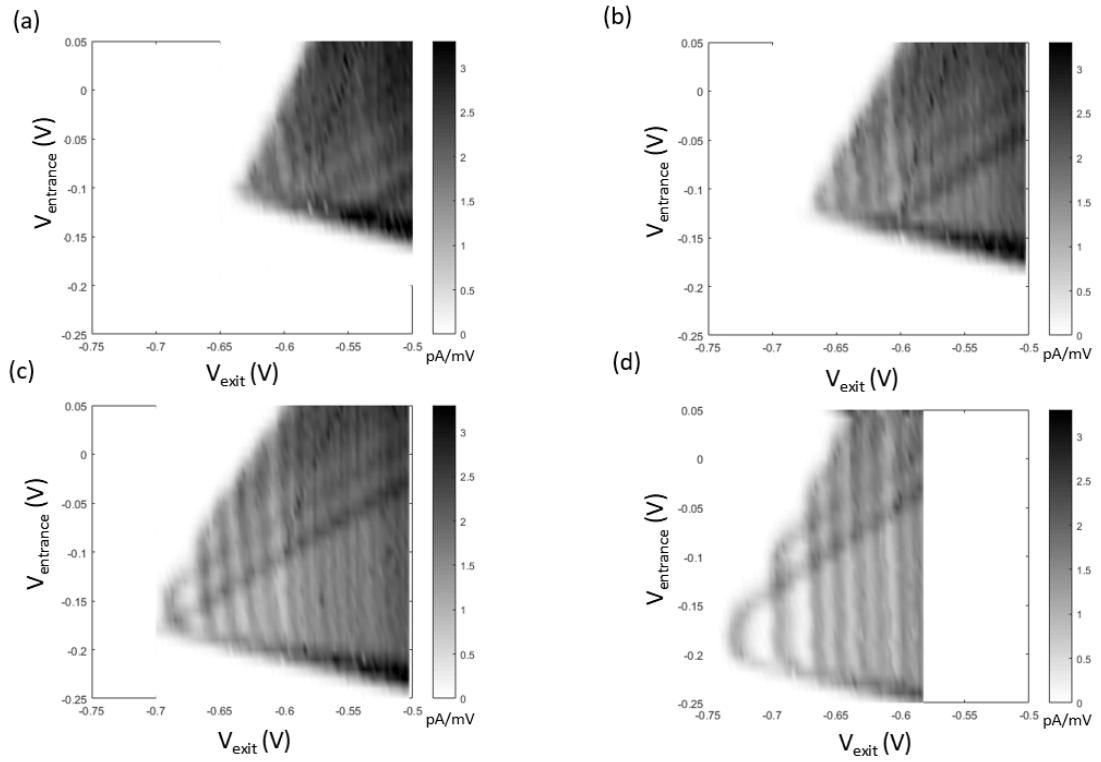

Figure 6.9: The derivative pumping maps change as the applied RF power increase. Here we plot the derivative dI/dV_{exit} to show the plateau regions more clearly. The RF frequency is always 110 MHz. The device is E1 channel etch, dot radius 130 nm, tunnel barrier width 85 nm and with polyimide deposited after e-beam gates. White area is the plateau and gray area is the transition edge of the plateau. The grayscale bar is the pumped electron number per cycle. (a) -5 dBm. (b) -4 dBm. (c) -3 dBm. (d) -2 dBm.

frequency AC conductance as a function of RF frequency for two different devices. We can see the pinch off voltage shift becomes smaller as the frequency increases, which means the transmitted RF power is less. We think the measurement set up affect the power transmission a lot. And the RF power transmission dependent more on the measurement set up than the pumps devices. Therefore in the next sections we keep the RF frequency at 110 MHz to study the required RF power to observe charge pumping.

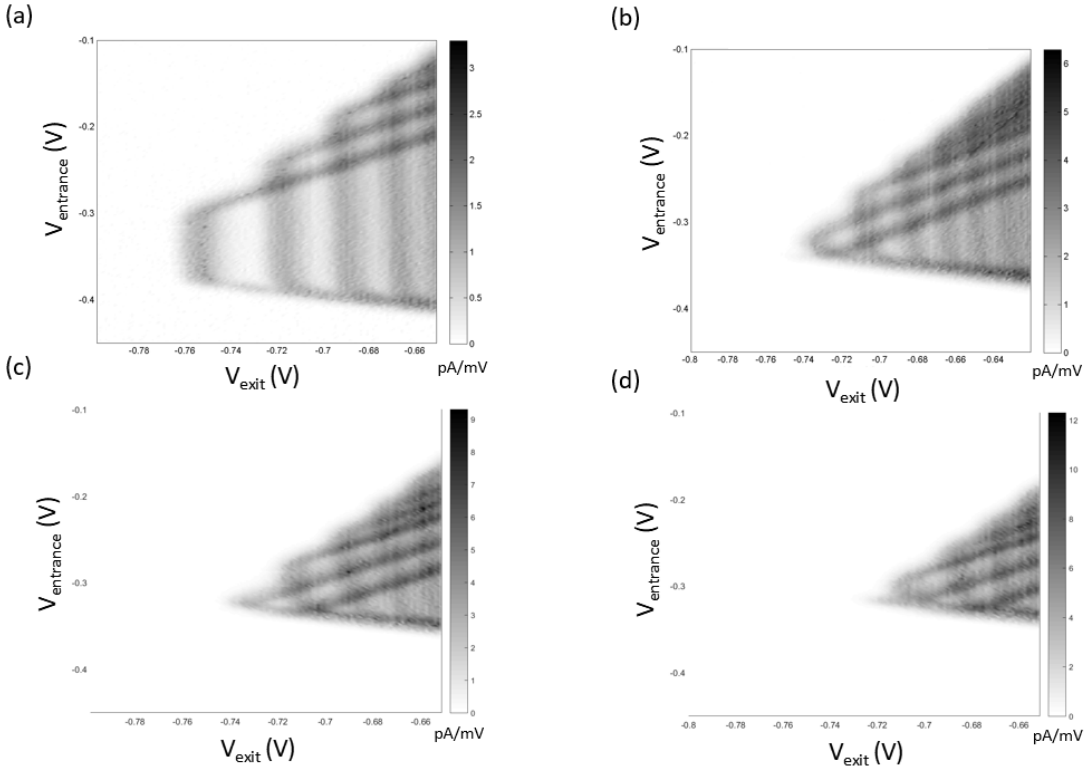

Figure 6.10: The derivative pumping maps changing as the applied RF frequency increases. The RF power is fixed at -2 dBm. The device has E1 channel etch, dot radius 130 nm, tunnel barrier width 100 nm and with polyimide deposited after e-beam gates. White area is the plateau and gray area is the transition edge of the plateau. (a) 110 MHz RF frequency applied. (b) 210 MHz RF frequency applied. (c) 310 MHz RF frequency applied. (d) 410 MHz RF frequency applied.

6.3.2 Comparison of different cool downs with the same device

We want to study whether a different cool down will affect the required RF power to observe clear pumping. We measured one device which has the E1 channel etch, dot radius 130 nm, tunnel barrier width 100 nm and polyimide deposited after e-beam gates in two different cool downs (shown in Fig. 6.12) . We find that in the first cool down we need -2 dBm to observe pumping while -4 dBm is needed to observe pumping in the second cool down. Therefore even for the same device different cool downs will require different RF power to observe pumping. We think this is because the carrier density distribution and disorder of the wafer will change for different cool down leading the pinch off voltage of the pumping gates to change.

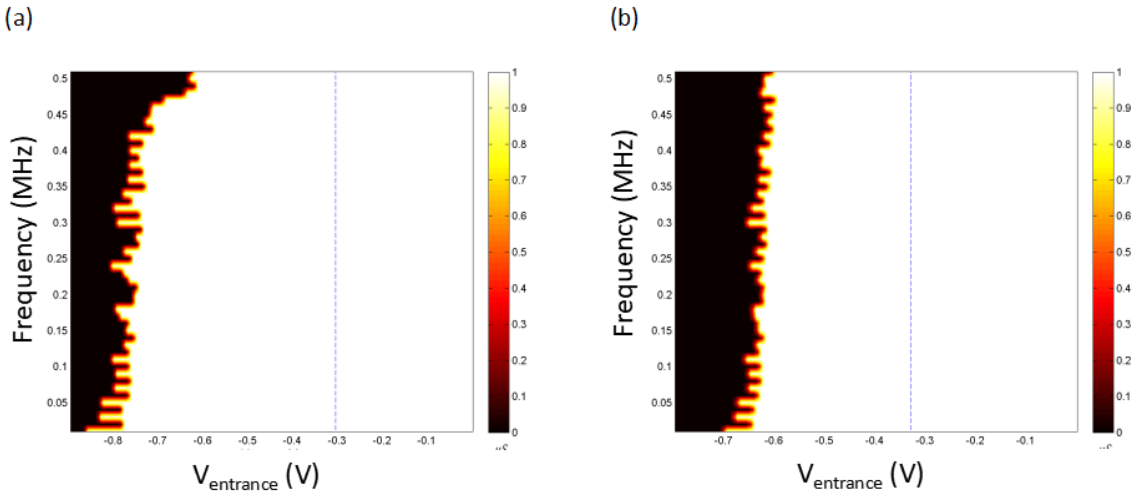

Figure 6.11: Pinch-off of entrance gate voltage for low-frequency AC conductance (measured using a lock-in amplifier at 77 Hz) as a function of RF frequency. (a) The device is E2 channel etch, dot radius 150 nm, tunnel barrier width 100 nm and with polyimide deposited after e-beam gates. The RF power applied is fixed at -1 dBm. (b) The device is E1 channel etch, dot radius 130 nm, tunnel barrier width 85 nm and with polyimide deposited after e-beam gates. The RF power applied is fixed at -4 dBm. The vertical blue dashed lines are the pinch-off voltage with no RF signal applied for each device. The green dashed lines are frequency at 110 MHz, 210 MHz, 310 MHz, 410 MHz and 510 MHz.

6.3.3 Comparison of different devices with the same design parameters

We want to study if the two different devices with the same design parameters required similar RF power to observe clear pumping. We measured two devices which both have E1 channel etch, dot radius 130 nm, tunnel barrier width 100 nm and polyimide deposited after e-beam gates (in Fig 6.13). We find that in the first device we need -2 dBm to observe pumping while 0 dBm is needed to observe pumping in the second device. Therefore devices with the same design parameters require different RF powers to observe pumping. We think this is because the carrier density distribution and disorder were different for the two devices, this will affect the pinch off voltage of the pumping gates. Also the fabrication will cause some random differences on the mesa etching, and gates deposition. This will mean that we need different RF powers to observe pumping.

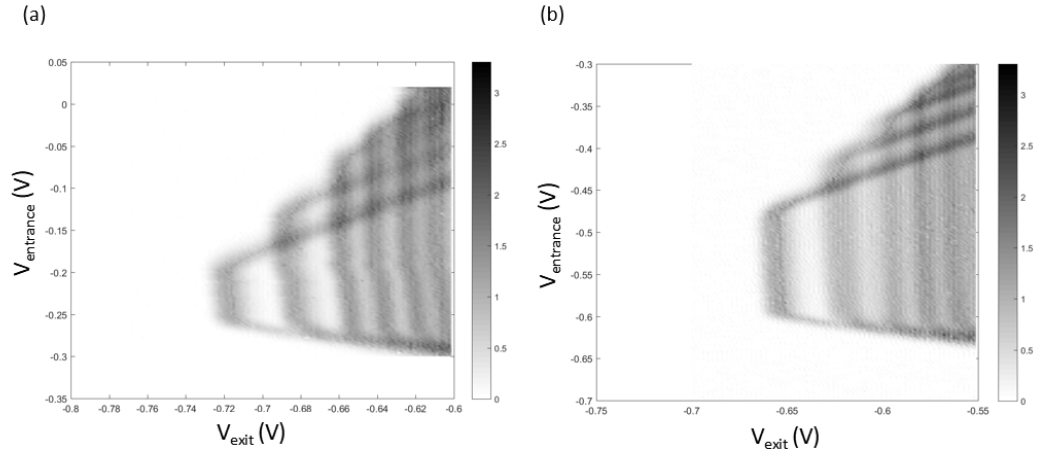

Figure 6.12: Comparison of different cool downs with the same device. (a) First cool down of the device, -2 dBm is required to observe clear pumping map. (b) Second cool down of the device, -4 dBm is required to observe clear pumping map. The device has E1 channel etch, dot radius 130 nm, tunnel barrier width 100 nm and polyimide deposited after e-beam gates. To help comparison, on both (a) and (b) we make the entrance gate voltage range 0.4 V and exit gate voltage 0.2 V.

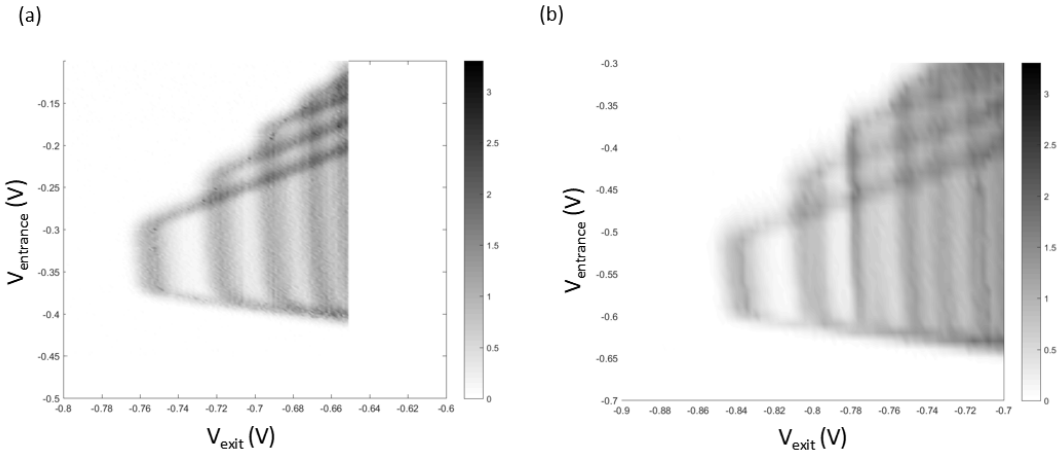

Figure 6.13: Comparison of two devices with the same parameters. (a) First device, -2 dBm is required to observe pumping. (b) Second device, 0 dBm is required to observe pumping. The devices both have E1 channel etch, dot radius 130 nm, tunnel barrier width 100 nm and polyimide deposited after e-beam gates. To help comparison, on both (a) and (b) we make the entrance gate voltage range 0.4 V and exit gate voltage 0.2 V.

6.3.4 Comparison of devices with different quantum-dot radius

We want to study whether the quantum-dot radius has some relationship with required RF power to observe clear pumping. We measured a two sets of two devices whose

design parameters are the same except for the quantum-dot radius. In Fig 6.14, the two devices both have E1 channel etch, tunnel barrier width 100 nm and polyimide deposited after e-beam gates. The dot size of the device in Fig 6.14 (a) is 130 nm and the device in Fig 6.14 (b) is 150 nm. We find that we need more power (2 dBm vs -2 dBm) for the larger dot size in order to observe pumping. The other comparison shown in Fig 6.15 is similar: we need -1 dBm for 150 nm dot radius and -2 dBm for 130 nm dot radius to observe pumping. However, we need to consider that even different cool downs could cause the required RF power to change (Fig. 6.12). This change is sometimes bigger than the change because of the dot size (in Fig. 6.15).

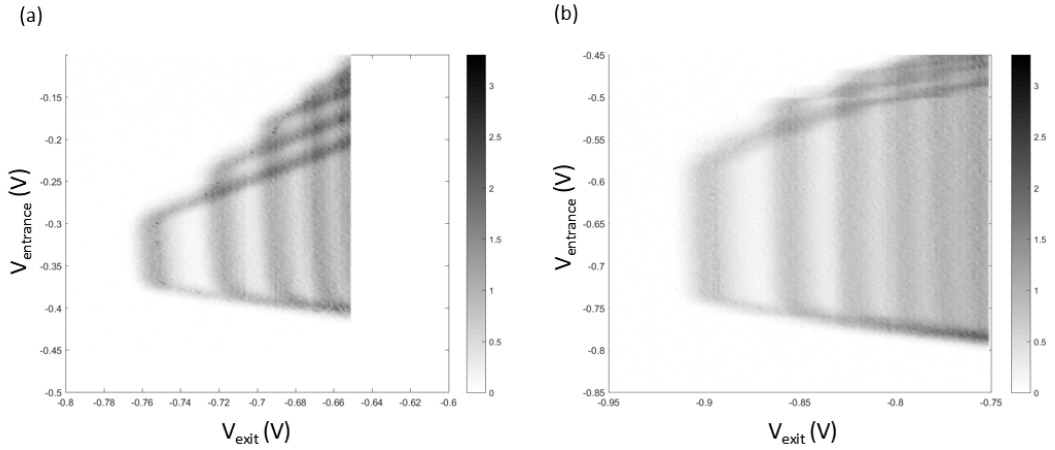

Figure 6.14: Effect of quantum-dot radius on the required RF power. (a) Dot radius: 130 nm, -2 dBm is required to observe a clear pumping map. The device has E1 channel etch, tunnel-barrier width 100 nm and polyimide deposited after e-beam gates. (b) Dot radius: 150 nm, 2 dBm is required to observe a clear pumping map. The device has E1 channel etch, tunnel barrier width 100 nm and polyimide deposited after e-beam gates. To help comparison, on both (a) and (b) we make the entrance gate voltage range 0.4 V and exit gate voltage 0.2 V.

6.3.5 Comparison of devices with different tunnel-barrier widths

We want to study whether the tunnel-barrier width has some relationship with the required RF power to observe clear pumping. We measured two sets of two devices whose design parameters are the same except for the tunnel-barrier width. In Fig. 6.16, the two devices both have E2 channel etch, dot radius 100 nm and polyimide deposited before e-beam gates. The tunnel barrier width of the device in Fig. 6.16 (a) is 85 nm and the device in Fig. 6.16 (b) is 100 nm. We find that we need more power (0 dBm vs -4 dBm) for larger tunnel barrier width to observe pumping. The other set comparison

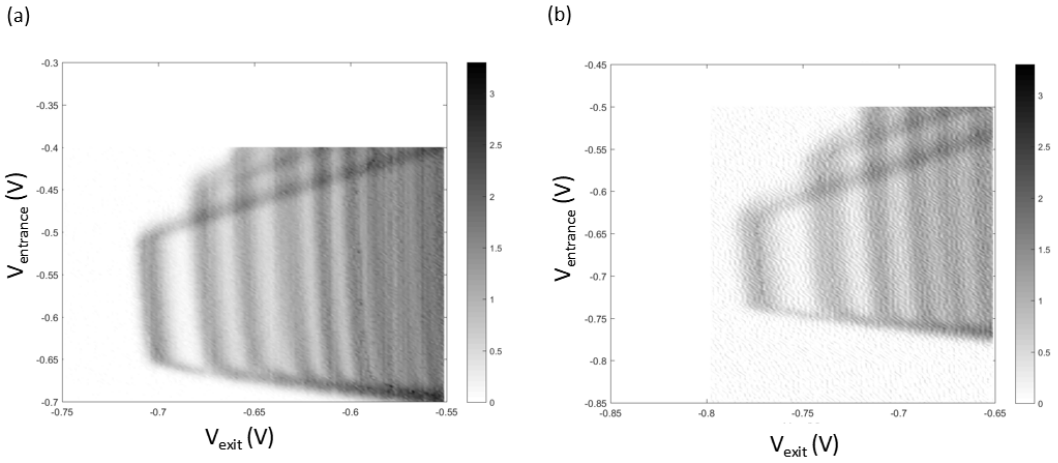

Figure 6.15: Effect of quantum-dot radius on the required RF power. (a) Dot radius: 130 nm, -2 dBm is required to observe a clear pumping map. The device has E2 channel etch, tunnel-barrier width 100 nm and polyimide deposited before e-beam gates. (b) Dot radius: 150 nm, -1 dBm is required to observe a clear pumping map. The device has E2 channel etch, tunnel barrier width 100 nm and polyimide deposited before e-beam gates. To help comparison, on both (a) and (b) we make the entrance gate voltage range 0.4 V and exit gate voltage 0.2 V.

shown the in Fig. 6.17 is similar: we need -3 dBm for the 85 nm barrier and -1 dBm for 100 nm barrier to observe pumping in these devices. We need to remember that even different cool downs could cause the required RF power to change (Fig. 6.12). This change is sometimes bigger than the change because of the dot size (in Fig. 6.15).

6.3.6 Comparison of channel etch design and the order of fabrication

We have two channel etch designs E1 and E2 in Fig. 6.6, and for both designs we have observed pumping. For E1 channel etch, quantum dot size 150 nm, tunnel barrier width 100 nm and with polyimide deposited after e-beam gates shown in Fig. 6.6 (a), 2 dBm RF power is required to observe clear pumping. For the E2 channel etch, quantum dot size 150 nm, tunnel barrier width 100 nm and with polyimide deposited before e-beam gates shown in Fig. 6.6 (b), -1 dBm RF power is required to observe clear pumping. We have observed pumping no matter with polyimide deposited after e-beam gates or with polyimide deposited before e-beam gates. This means we can use either order of fabrication in future for MUX pump array processing.

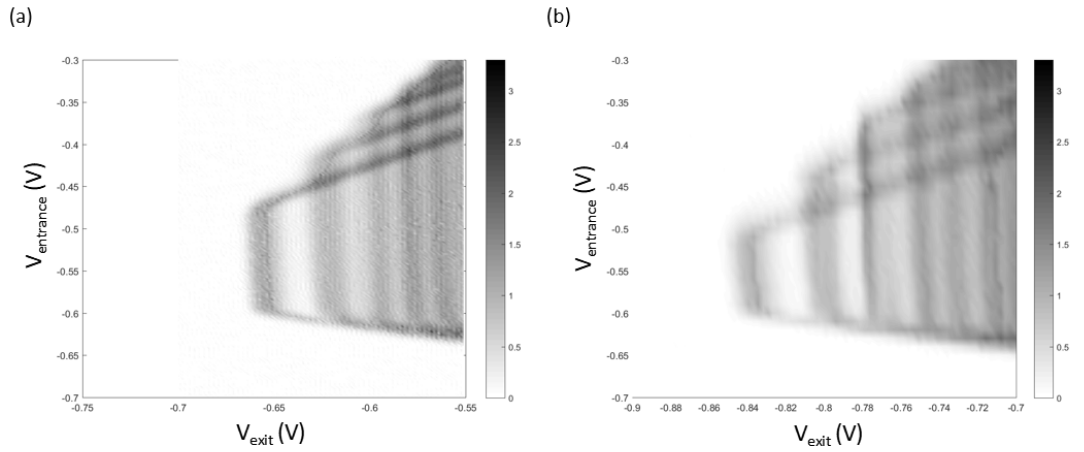

Figure 6.16: Comparison of how tunnel barrier width affects the required RF power. (a) Tunnel barrier width: 85 nm. -4 dBm is required to observe a clear pumping map. The device has E1 channel etch, quantum dot size 130 nm and polyimide deposited after e-beam gates. (b) Tunnel barrier width: 100 nm. 0 dBm is required to observe a clear pumping map. The device has E1 channel etch, quantum dot size 130 nm and polyimide deposited after e-beam gates. To help comparison, on both (a) and (b) we make the entrance gate voltage range 0.4 V and exit gate voltage 0.2 V.

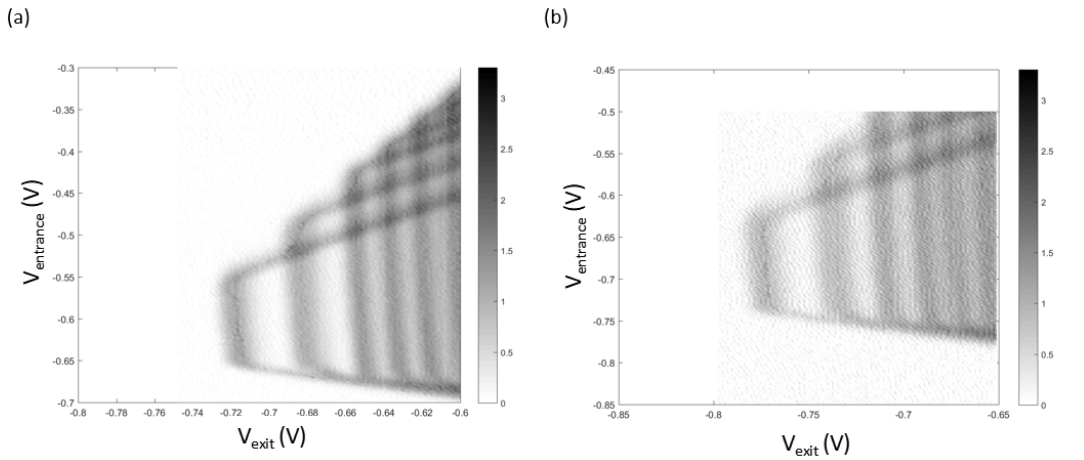

Figure 6.17: Comparison of how tunnel barrier width affects the required RF power. (a) Tunnel barrier width: 85 nm, -3 dBm is required to observe a clear pumping map. The device is E2 channel etch, quantum dot size 150 nm and with polyimide deposited before e-beam gates. (b) Tunnel barrier width: 100 nm, -1 dBm is required to observe a clear pumping map. The device has E1 channel etch, quantum dot size 150 nm and with polyimide deposited before e-beam gates. To help comparison, on both (a) and (b) we make the entrance gate voltage range 0.4 V and exit gate voltage 0.2 V.

6.4 Pumping error mechanisms analysis

6.4.1 Fitting with the decay-cascade model

Many different types of single-electron pumps can be explained by the 'decay cascade' model [59]. We begin by introducing the decay-cascade model built by Kashcheyevs

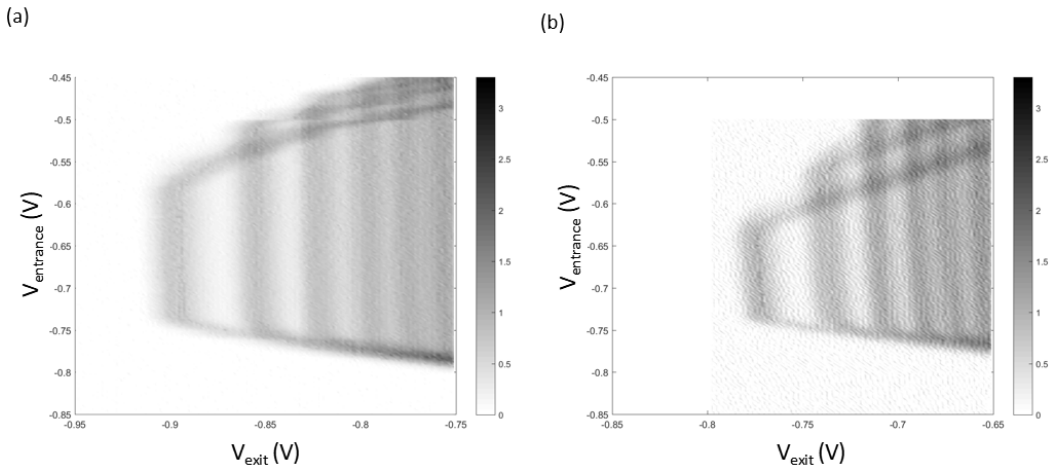

Figure 6.18: Comparison of channel etch designs. (a) E1 design, polyimide after e-beam gates. Quantum-dot size 150 nm, tunnel barrier width 100 nm and with polyimide deposited after e-beam gates, 2 dBm RF power is required to observe clear pumping. (b) E2 design, polyimide before ebeam gates. Quantum dot size 150 nm, tunnel barrier width 100 nm and with polyimide deposited before e-beam gates, -1 dBm RF power is required to observe clear pumping. To help comparison, on both (a) and (b) we make the entrance gate voltage range 0.4 V and exit gate voltage 0.2 V.

et al. [59] In this model, single-electron pumps operate in a regime which can be defined by three inequalities as follows [60]:

$$k_B T \ll E_C = \frac{e^2}{C_\Sigma}. \tag{6.1}$$

$$R_K \ll R. \tag{6.2}$$

$$f \ll \Gamma. \tag{6.3}$$

Here k_B is Boltzmann's constant, T is temperature, E_C is the Coulomb gap energy of the pump islands, C_Σ is the capacitance of the pump islands, $R_K = h/e^2$ is the resistance quantum, R is the resistance of the tunnel barriers, f is the radio frequency applied to the entrance gate and Γ is the electrons' tunnelling rate from source to the quantum dot defined by the gates. Eq. 6.1 shows that thermal fluctuations would not affect the number of electrons on each island. Eq. 6.2 says the quantum fluctuations would not affect the number of electrons on the island. Eq. 6.3 states that the energy of each island is manipulated (by the radio frequency applied to the entrance gate)

slowly enough that the pumping can be always attained at each point in the pumping cycle.

In the capture phase the entrance barrier change with the driving RF signal applied on the entrance gate, which will traps a number of electrons $n(t)$ in the quantum dot. The electrons in the quantum dot are in states separated by E_C. The higher-n states have higher energy and so have a higher possibility of tunneling back to the source. The electrons in the source and drain can tunnel into the quantum dot from a thermal distribution in the leads which would increase the number of electrons in the dot. The decay-cascade model assumes this tunneling is negligible during the back-tunneling phase of the pumping cycle. We only consider electrons that tunnel from the quantum dot into the leads, so the number of electrons in the quantum dot can only decrease in this case. In the zero temperature limit, the rate equation can be described as follows:

$$\mathrm{d}P_n/\mathrm{d}t = \Gamma_n(t)P_n \tag{6.4}$$

where P_n is the probability that there are n electrons in the quantum dot. When the energy of the n-electron state is above the Fermi level, $\Gamma_n(t)$ represents the time-dependent escape rate after $t = t_n$ which is the time when the n-electron state crossed the Fermi level. Then P_n which is the trapping probability at a time t can be described as follows:

$$P_n(t) = \exp[-\int_{t_n}^{t} \Gamma_n(\tau)d\tau] \tag{6.5}$$

The small overlap between the tunneling of different electron number states will affect pumping accuracy. For example, one electron escapes from the $n+1$-electron state which would increase the probability of the n-electron state P_n. And one electron escapes from the n-electron state which would decrease the probability of the n-electron state P_n. When $n = 1$, the normalised number of pumped electrons is given by

$$I_P/ef = (P_n - P_{n+1}) + 2P_{n+1} = P_{n+1} + P_n \tag{6.6}$$

Here I_P is the pumping current, and f is the pumping frequency. If we make Γ_{n+1} much faster than Γ_n which would cause decay cascade, then the pump accuracy would be improved.

For most experimental results that gate-defined tunnel barrier can be modelled to have a parabolic shape. We describe the time-dependent escape rate as follows in the capture phase:

$$\Gamma_n(t) = \Gamma_a \exp[-U_n(t)/k_B T_0] \ (T < T_0) \tag{6.7}$$

where $U_n(t) = U_0(t) - nE_C$ is the time-dependant barrier height of the quantum dot and Γ_a is a constant. T_0 is the crossover temperature of thermal hopping and tunnelling. Then P_n can be described with an exponential with Γ_n from Eq. 6.5. Normally the tuning voltage V_G on the entrance gate would be introduced to compare the experimental data, and then the pumping current would be described as a function of tuning voltage as follows:

$$\frac{I_P}{ef} = \sum_{n=1}^{\infty} \exp\left[-\exp\left(-\delta_n \frac{V_G - V_n}{V_{n+1} - V_n}\right)\right] \tag{6.8}$$

Here δ_n is a fitting parameter, which can be related to a ratio of tunnel rates. V_n is the onset voltage of the n-th current plateau on the pumping map, and $V_{n+1} - V_n = E_C/\alpha_G = e/C_G$, C_G is the capacitance of the quantum dot to the exit gate. Normally for high accuracy pumping measurements over the range $0<I_P/ef<1.5$ only the first two summation terms of Eq. 6.8 have been fitted, and the parameter δ_n has been used to represent the pumping accuracy: larger δ_n means a flatter plateau. Several studies [3] [61] have used Eq. 6.8 to estimate pumping accuracy.

Figure 6.19 to Fig. 6.21 the red lines describe how the decay cascade model fits our measurement data. We see that fitting parameter δ_1 is not as large as in several studies [3] [61] before. Ref. [3] reported $\delta = 20$ at $f = 945$ MHz and Ref. [61] reported $\delta = 22$ at $f = 6.5$ GHz. These δs are bigger than our experiment and we think that the reason is that we do not apply any magnetic field like in Ref. [3]. And our quantum dot is much bigger than in Ref. [61], so the charging energy will be larger. From the decay-cascade model fitting, the capacitance between the exit gate and the dot is 4.4 aF, 5.4 aF and 4.4 aF respectively for the three devices (from Fig.6.19 to Fig. 6.21) we modelled here.

6.4.2 Fitting with the thermal capture model

In this section we fit our measurement data using the thermal capture model. We begin by introducing the thermal capture model [60]. The thermal capture regime describes the electrons are exchanged between the leads and the quantum dot during

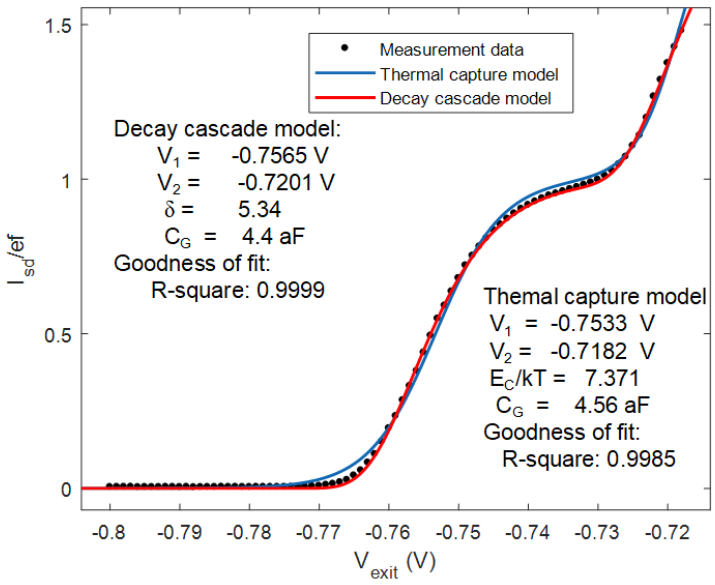

Figure 6.19: Comparison of the measurement data and model fitting using the decay cascade model and thermal capture model. The red line is the decay cascade model and the blue line is the thermal capture model. The device is E1 channel etch, dot radius 130 nm, tunnel barrier width 100 nm and with polyimide deposited after e-beam gates. 110 MHz -2 dBm RF is applied to the entrance gate.

the initialisation process because of thermal fluctuation, then the average number of captured electrons given by Coulomb blockade theory can be described as:

$$\frac{I_P}{ef} = \sum_{n=1}^{\infty} n \left[\frac{\exp[-(E_n - n\alpha_G V_G)/k_B T]}{\sum_{n=1}^{\infty} \exp[-(E_n - n\alpha_G V_G)/k_B T]} \right] \sim \sum_{n=1}^{\infty} \left[1 + \exp\left(-\frac{E_C}{k_B T} \frac{V_G - V_n}{V_{n+1} - V_n} \right) \right]^{-1} \tag{6.9}$$

where V_n is the onset voltage of the n-th current plateau on the pumping map, and $V_{n+1} - V_n = E_C/\alpha_G = e/C_G$, C_G is the capacitance of the quantum dot to the entrance gate, and $\alpha_G = eC_G/C_\Sigma$,$E_n = n^2 E_C/2$. Then the thermal-equilibrium parameter $E_C/k_B T$ can be used to describe the pumping accuracy [8] [62].

Figure 6.19 to Fig. 6.21 the blue lines describe how the thermal capture model fits our measurement data. We see that thermal capture model also fits the measurement data well which means that the temperature can also affect the pumping accuracy in our measurements. From the thermal capture model fitting, the capacitance between the exit gate and the dot is 4.5 aF, 5.5 aF and 4.5 aF respectively for the three devices we modelled here.

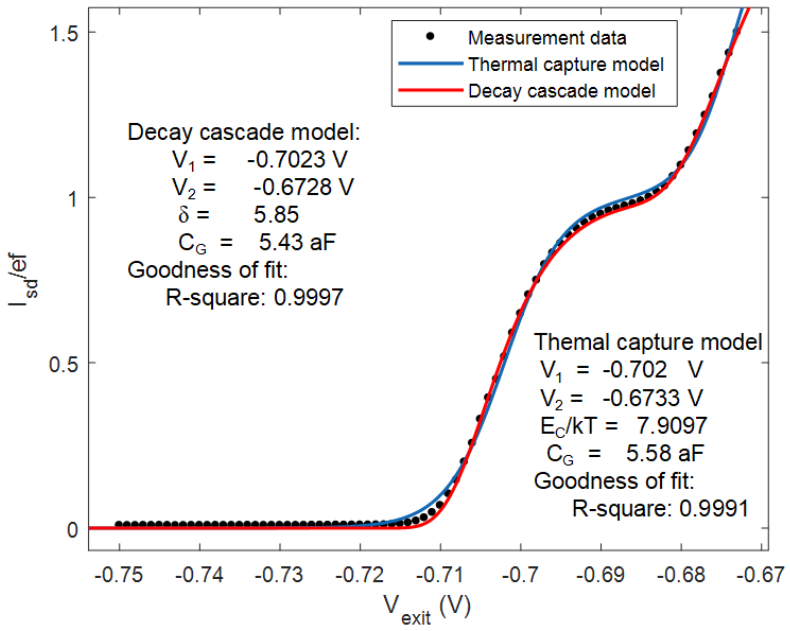

Figure 6.20: Comparison of the measurement data and model fitting using the decay cascade model and thermal capture model. The red line is the decay cascade model and the blue line is the thermal capture model. The device is E2 channel etch, dot radius 130 nm, tunnel barrier width 100 nm and with polyimide deposited before e-beam gates. 110 MHz -3 dBm RF is applied to the entrance gate.

We can learn that measurement data fits both decay cascade model and thermal capture model well, we think the electrons tunnelling back from quantum dot to the source and thermal fluctuations both occur together. On the other side, when we compare the decay cascade model fitting and thermal capture model, we find that the decay cascade model fits the measurement data slightly better. We make this judgement based on two present evidence: firstly, we can observe visually that the red curves fits slightly better than the blue curves from Figure 6.19 to Fig. 6.21. Secondly, for the R-square coefficient for each pair fitting comparison, the decay cascade model is always bigger than the thermal capture model. Thus we think maybe the pumping error of measurements mainly comes from the electrons tunnelling back from the quantum dot to the source, rather than the thermal fluctuations.

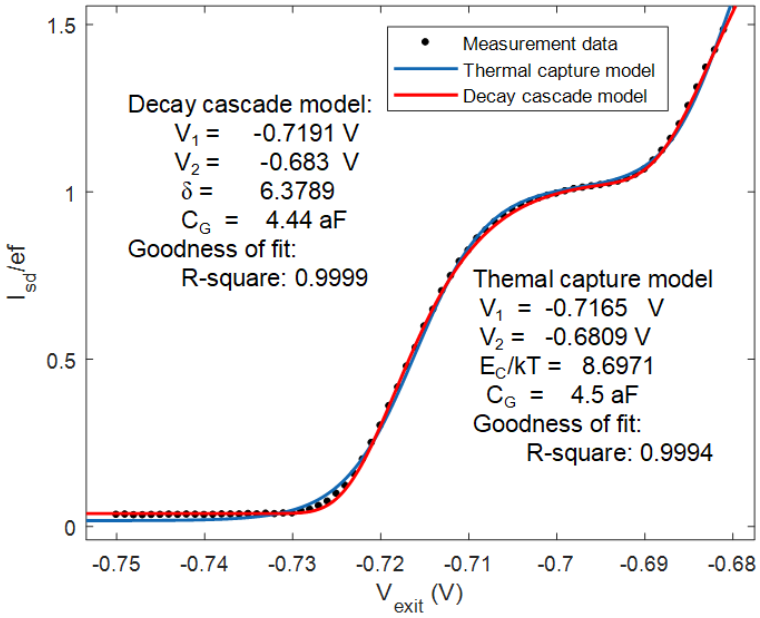

Figure 6.21: Comparison of the measurement data and model fitting using the decay cascade model and thermal capture model. The device is E2 channel etch, dot radius 150 nm, tunnel barrier width 85 nm and with polyimide deposited before e-beam gates. 110 MHz -3 dBm RF is applied to the entrance gate.

6.5 Conclusion

Adding polyimide between the contacting gates and GaAs wafer surface is not a problem for the single-electron pump, and is a necessary step towards making MUX pump arrays.

In this chapter, we began by demonstrating that a single-electron pump with MUX-style polyimide can realize pumping. We present the definition of required RF power to observe a clear pumping map. We also presented our design of single-electron pump with polyimide added with several design variations such as the dot radius (130 nm and 150 nm), the tunnel barrier width (85 nm and 100 nm), the channel etch design and the order of fabrication. We find that all these designs can realize quantised charge pumping but there is a difference in the required RF power needed on the entrance gate to observe a clear pumping map. In two separate cool-downs of the same device, different RF powers (-2 dBm and -4 dBm) were required to observe pumping. Two different devices with the same design required different RF powers (-2 dBm and 0 dBm) to observe pumping. For quantum dot radius 130 nm and 150 nm, -2 dBm and 2 dBm or -3 dBm and -1 dBm RF power were required for different devices which have

same parameters except dot radius. For tunnel barrier width 85 nm and 100 nm, -4 dBm and 0 dBm or -3 dBm and -1 dBm are required for two different devices which had the same parameters except tunnel barrier width. We have learnt even separate cool downs could change the required RF power to observe a clear pumping map. These gate design variations seem to be too small to affect the pump performance very much compared to the random variations. We observed pumping in devices with polyimide deposited after e-beam gates or with polyimide deposited before e-beam gates, which means that we can use any either order of fabrication in the future MUX pump array processing.

We learn from Dr Patrick See that the best pump the gate design for a new wafer is normally based on empirical evidence. Even for the wafers with the same carrier density, the best pumping gate designs are normally different. This may be because the mobility of wafers is different. For example, when a new wafer with carrier density 2×10^{15} m^{-2} is used for single-electron pump measurements, the process to get the best pump gate design is as follows: from previous experience, for the same carrier density the best design is a dot size of 150 nm, tunnel-barrier width 100 nm and a gap of 50 nm. Then several design variations of individual single-electron pumps (such as dot sizes of 130 nm, 150 nm and 175 nm, tunnel-barrier width: 80 nm, 100 nm and 120 nm, gap: 50 nm, 75 nm and 100 nm) are measured in separate cool-downs to find the best pump design. Future MUX single-electron pump arrays have many benefits to simplify this process: for example for this wafer we can make the dot radius range from 50 nm to 250 nm in steps of 20 nm and tunnel-barrier width from 50 nm to 200 nm in steps of 10 nm to make many pump gates design combinations to find the best design. This will save the time taken for different cool downs and also avoid different cool downs while causing the pump map to change. Besides, since the MUX pump array is able to include large number of different parameter pump designs, the best design parameters could be found more precisely than previous standard process.

We fit measurement data using both decay cascade model and thermal capture model, and we find both models fit well. Thus we think the pumping error comes from both the electrons tunnelling back from the quantum dot to the source and thermal fluctuations. Based on the evidence the decay cascade fits slight better, we guess the pumping error mainly comes from the the electrons tunnelling from the quantum dot to the source. In the decay cascade model, we calculate the capacitance between the exit gate and dot is 4.4 aF, 5.4 aF and 4.4 aF respectively for the three devices we modelled here. In the thermal capture model, we calculate the capacitance between the exit gate and dot is 4.5 aF, 5.5 aF and 4.5 aF respectively.

7

Conclusions and future work

7.1 Conclusions

In this thesis, we have studied the rectified current in wide-channel electron pump devices, transmission of radio-frequency signals through a quantum multiplexer and single-electron pumps with an insulator layer (polyimide) which is necessary to make multiplexed single-electron-pump arrays based on a GaAs/AlGaAs heterostructure.

Rectified current in wide-channel electron pump devices. We have measured a 4 x 32 multiplexed wide-channel electron pump array. We observed rectified current (about 100 μA) instead of pumping current (which could be 18 pA at 110 MHz). We measured individual wide-channel single-electron pumps and also observed rectified current, showing that the rectified current is caused by the wide-channel pumps, not the multiplexer. We showed that the pump entrance gate, to which the RF signal is applied, does not need to go all the way across the channel to give the rectified current. We also showed that no matter how close together the entrance gate with exit gate are, rectified current can still be observed, and the peak rectified current happens near the exit gate pinch off voltage. We have found that the rectified current becomes bigger as RF frequency increases (10 MHz to 110 MHz) or RF amplitude increases (-20 dBm to -5 dBm). We have developed a model to qualitatively explain the origin

of rectified current in the wide-channel electron-pump devices. We need to switch to narrow-channel electron pump devices to make GaAs electron pump arrays because of the smaller rectified current [3].

Transmission of radio-frequency signals through a quantum multiplexer. We have characterised the transmission of RF voltage signals through the quantum multiplexer (MUX) using an array of bar gates. We found that RF signal up to an amplitude ∼300 mV AC amplitude voltage can be transmitted to the bar gate, which may be enough for electron pumping. We also presented a statistical study of multiplexed bar gate devices: we measured the pinch-off voltage and maximum transconductance dG/dV_g of all 256 gates. We find that because 0.1 μm is comparable with the 2DEG depth (90 nm), more negative voltage is needed to pinch off 0.1 μm wide bar gates as compared to wider gates. The maximum transconductance dG/dV_g, in 0.1 μm wide bar gates is smaller than in wider devices. We studied how the RF transmission changes with the distance from the multiplexer. We explained how we used the pinch-off shift (the pinch-off voltage will be more negative when we apply an RF signal to bar gate, and we call the voltage change the pinch-off shift), to determine the RF power transmission. We found that the device location on the chip and the distance between the bar gate and RF source do not have a strong relation with the pinch-off voltage shift. We resigned the multiplexer to reduce the capacitance of the addressing gates to the 2DEG and compared the RF transmission between the old MUX and new MUX designs. However, we find that at high frequency the RF transmission of the new MUX does not improve much. We found this is because there are two parts to the capacitance (addressing gates with 2DEG and bar gates with 2DEG) and the bar gates part is much bigger. We have also designed devices to measure the multiplexer resistance in order to calculate the capacitance of the addressing gates with 2DEG, which is about 1.93 pF, giving a 3 dB frequency of 500 MHz. In future MUX pump designs, we need to decrease the gate area connecting the array of bar gates which makes a bigger contribution to the total capacitance than the addressing gates, to improve the RF transmission.

Single-electron pump with multiplexer-style polyimide. We have demonstrated electron pumping in a single-electron pump device in which the gates extend across the entire GaAs channel, and are insulated from the GaAs channel by a polyimide layer as required for a multiplexed electron-pump design. We also studied several variations of pump gates designs, namely dot radius (130 nm and 150 nm), the tunnel barrier width (85 nm and 100 nm), the channel etch design and the order of fabrication,

and how they will affect the RF power required to observe clear quantised pumping. In summary:

• In two separate cool-downs of the same device, different RF powers (-2 dBm and -4 dBm) were required to observe pumping.

• Two different devices with the same design required different RF power (-2 dBm and 0 dBm) to observe pumping.

• For quantum-dot radius 130 nm and 150 nm, -2 dBm and 2 dBm or -3 dBm and -1 dBm RF power are required for different devices which have same parameters except dot radius.

• For tunnel barrier widths 85 nm and 100 nm, -4 dBm and 0 dBm or -3 dBm and -1 dBm are required for different devices which have same parameters except tunnel barrier width.

These gate design variations seem to be too small to affect the pump performance very much compared to the random variations. We also observed pumping in devices with polyimide deposited after e-beam gates or with polyimide deposited before ebeam gates, which means that we can use any either order of fabrication in processing future MUX pump arrays.

7.2 New multiplexed pump array design

Constant modification and improvements of the GaAs multiplexed single-electron pump arrays design have been made at each step of this thesis. We have progressed from the design of multiplexed wide-channel single-electron pump arrays, individual wide-channel single-electron pumps, multiplexed bar gate devices to individual single-electron pumps with polyimide added. At present a new design of the multiplexed single-electron pump array has been fabricated and is ready to test. The design is shown in Fig. 7.1. There are 16 source and drain channels which can be controlled by the multiplexer. There are 4 pairs of contacting pump gates. One pair defines 1 pump on one channel, the second pair defines 2 pumps on two channels, the third pair defines 8 pumps on eight channels, the fourth pair defines 16 pumps on 16 channels. Since the narrow-channel etching could cause a channel to become non-conducting, therefore for this design we try to avoid many pumps in series in one single channel. Some interesting experiments could be carried out on the chip:

• Since we can measure several narrow-channel pumps in a single cool down, we can design and measure different gate designs to find the design giving the best pumping performance.

• As we learnt from Chapter 6, even separate cool-downs could change the required RF power to observe a clear pumping map. On this MUX pump array we can get rid of the cool-down variable and explore if there is any relationship between the required RF power and quantum dot-radius or tunnel barrier width.

• By controlling the addressing gates and pump gates, we can try to use this MUX pump array to realize parallel pumping.

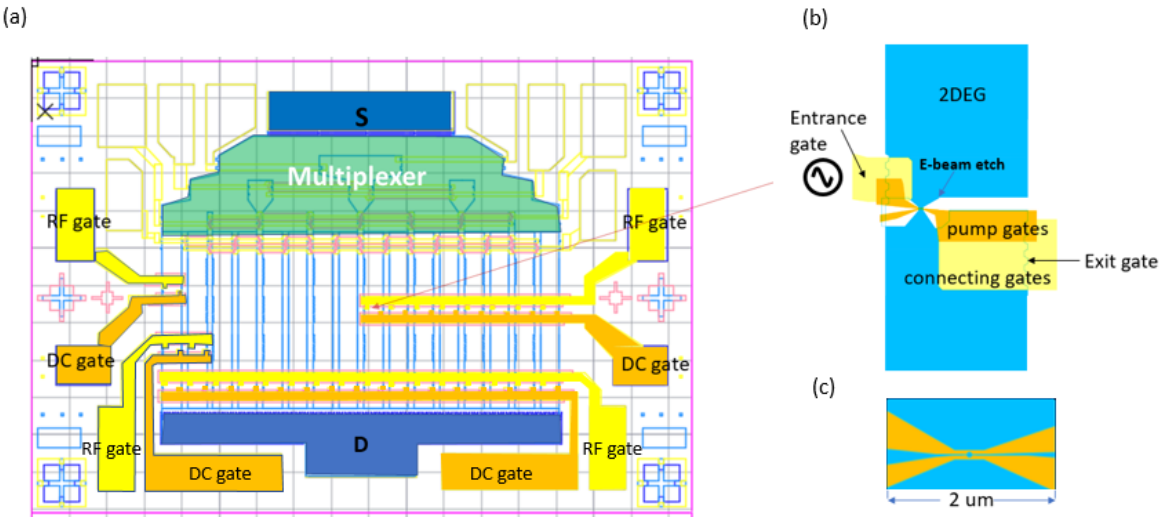

Figure 7.1: (a) Schematic of the new MUX single-electron pump arrays. The blue area is the source and drain, the green area is the multiplexer, dark yellow indicates exit gates, and light yellow indicates entrance gates. (b) Individual electron pump. Grey indicates the polyimide insulator, the blue is 2DEG. (c) Zoom-in of the pump gates.

In future MUX pump arrays, we will also multiplex the gate voltage signals. The capacitance associated with the e-beam gates of the pumps will be much smaller than in MUX bar gate devices because the narrow channel etch removes the 2DEG from underneath most of the gates area. This should improve the RF transmission.

References

[1] SI BIPM. The international system of units (si). *Bureau international des poids et mesures*, 2006.

[2] MD Blumenthal, B Kaestner, L Li, S Giblin, TJBM Janssen, M Pepper, D Anderson, G Jones, and DA Ritchie. Gigahertz quantized charge pumping. *Nature Physics*, 3(5):343, 2007.

[3] SP Giblin, M Kataoka, JD Fletcher, P See, TJBM Janssen, JP Griffiths, GAC Jones, I Farrer, and DA Ritchie. Towards a quantum representation of the ampere using single electron pumps. *Nature communications*, 3:930, 2012.

[4] Friederike Stein, Dietmar Drung, Lukas Fricke, Hansjörg Scherer, Frank Hohls, Christoph Leicht, Martin Götz, Christian Krause, Ralf Behr, and Eckart Pesel. Validation of a quantized-current source with 0.2 ppm uncertainty. *Applied Physics Letters*, 107(10):103501, 2015.

[5] Jukka P Pekola, Olli-Pentti Saira, Ville F Maisi, Antti Kemppinen, Mikko Möttönen, Yuri A Pashkin, and Dmitri V Averin. Single-electron current sources: Toward a refined definition of the ampere. *Reviews of Modern Physics*, 85(4):1421, 2013.

[6] Clark A Hamilton. Josephson voltage standards. *Review of scientific instruments*, 71(10):3611–3623, 2000.

[7] F Stein, H Scherer, T Gerster, R Behr, M Götz, E Pesel, C Leicht, N Ubbelohde, T Weimann, K Pierz, et al. Robustness of single-electron pumps at sub-ppm current accuracy level. *Metrologia*, 54(1):S1, 2016.

[8] R Zhao, Alessandro Rossi, SP Giblin, JD Fletcher, FE Hudson, Mikko Möttönen, M Kataoka, and AS Dzurak. Thermal-error regime in high-accuracy gigahertz single-electron pumping. *Physical Review Applied*, 8(4):044021, 2017.

[9] H Al-Taie, LW Smith, B Xu, P See, JP Griffiths, HE Beere, GAC Jones, DA Ritchie, MJ Kelly, and CG Smith. Cryogenic on-chip multiplexer for the study of quantum transport in 256 split-gate devices. *Applied Physics Letters*, 102(24):243102, 2013.

[10] LW Smith, H Al-Taie, AAJ Lesage, F Sfigakis, P See, JP Griffiths, Harvey Edward Beere, GAC Jones, David Alastair Ritchie, AR Hamilton, et al. Dependence of the 0.7 anomaly on the curvature of the potential barrier in quantum wires. *Physical Review B*, 91(23):235402, 2015.

[11] RK Puddy, LW Smith, H Al-Taie, CH Chong, Ian Farrer, JP Griffiths, David Alastair Ritchie, Michael Joseph Kelly, M Pepper, and Charles Gordon Smith. Multiplexed charge-locking device for large arrays of quantum devices. *Applied Physics Letters*, 107(14):143501, 2015.

[12] P Mirovsky, B Kaestner, C Leicht, AC Welker, T Weimann, K Pierz, and HW Schumacher. Synchronized single electron emission from dynamical quantum dots. *Applied Physics Letters*, 97(25):252104, 2010.

[13] Ville F Maisi, Yuri A Pashkin, Sergey Kafanov, Jaw-Shen Tsai, and Jukka P Pekola. Parallel pumping of electrons. *New Journal of Physics*, 11(11):113057, 2009.

[14] John H Davies. *The physics of low-dimensional semiconductors: an introduction*. Cambridge University Press, 1998.

[15] Joanna Waldie. *Electrical current at single electron level*. PhD thesis, University of Cambridge, 2015.

[16] TJ Thornton, M Pepper, H Ahmed, D Andrews, and GJ Davies. One-dimensional conduction in the 2d electron gas of a gaas-algaas heterojunction. *Physical Review Letters*, 56(11):1198, 1986.

[17] Keith Barnham and Dimitri Vvedensky. *Low-dimensional semiconductor structures: Fundamentals and device applications*. Cambridge University Press, 2008.

[18] Paul Harrison and Alex Valavanis. *Quantum wells, wires and dots: theoretical and computational physics of semiconductor nanostructures*. John Wiley & Sons, 2016.

[19] Eoin O'Reilly. *Quantum theory of solids*. CRC Press, 2014.

[20] Marc A Kastner. The single-electron transistor. *Reviews of Modern Physics*, 64(3):849, 1992.

[21] Leo P Kouwenhoven, Charles M Marcus, Paul L McEuen, Seigo Tarucha, Robert M Westervelt, and Ned S Wingreen. Electron transport in quantum dots. In *Mesoscopic Electron Transport*, pages 105–214. Springer, 1997.

[22] Leo P Kouwenhoven, DG Austing, and Seigo Tarucha. Few-electron quantum dots. *Reports on Progress in Physics*, 64(6):701, 2001.

[23] Michel H Devoret, Daniel Esteve, and Cristian Urbina. Single-electron transfer in metallic nanostructures. *Nature*, 360(6404):547, 1992.

[24] Mark Blumenthal. *Gigahertz quantised charge pumping*. PhD thesis, University of Cambridge, 2007.

[25] R OIML. Organisation internationale de métrologie légale. *Bureau Internationale De Metrologie Legale*, 11, 2015.

[26] F Piquemal and G Genevès. Argument for a direct realization of the quantum metrological triangle. *Metrologia*, 37(3):207, 2000.

[27] KK Likharev and AB Zorin. Theory of the bloch-wave oscillations in small josephson junctions. *Journal of Low Temperature Physics*, 59(3-4):347–382, 1985.

[28] Mark W Keller. Current status of the quantum metrology triangle. *Metrologia*, 45(1):102, 2008.

[29] Brian David Josephson. Possible new effects in superconductive tunnelling. *Physics letters*, 1(7):251–253, 1962.

[30] K v Klitzing, Gerhard Dorda, and Michael Pepper. New method for high-accuracy determination of the fine-structure constant based on quantized hall resistance. *Physical Review Letters*, 45(6):494, 1980.

[31] LJ Geerligs, VF Anderegg, PAM Holweg, JE Mooij, H Pothier, D Esteve, C Urbina, and MH Devoret. Frequency-locked turnstile device for single electrons. *Physical Review Letters*, 64(22):2691, 1990.

[32] H Pothier, P Lafarge, C Urbina, D Esteve, and MH Devoret. Single-electron pump based on charging effects. *EPL (Europhysics Letters)*, 17(3):249, 1992.

[33] LP Kouwenhoven, AT Johnson, NC Van der Vaart, CJPM Harmans, and Cf T Foxon. Quantized current in a quantum-dot turnstile using oscillating tunnel barriers. *Physical Review Letters*, 67(12):1626, 1991.

[34] Akira Fujiwara, Neil M Zimmerman, Yukinori Ono, and Yasuo Takahashi. Current quantization due to single-electron transfer in si-wire charge-coupled devices. *Applied Physics Letters*, 84(8):1323–1325, 2004.

[35] MR Connolly, KL Chiu, SP Giblin, M Kataoka, JD Fletcher, C Chua, JP Griffiths, GAC Jones, VI Fal'Ko, CG Smith, et al. Gigahertz quantized charge pumping in graphene quantum dots. *Nature Nanotechnology*, 8(6):417, 2013.

[36] Jukka P Pekola, Juha J Vartiainen, Mikko Möttönen, Olli-Pentti Saira, Matthias Meschke, and Dmitri V Averin. Hybrid single-electron transistor as a source of quantized electric current. *Nature Physics*, 4(2):120, 2008.

[37] SJ Chorley, J Frake, CG Smith, GAC Jones, and MR Buitelaar. Quantized charge pumping through a carbon nanotube double quantum dot. *Applied Physics Letters*, 100(14):143104, 2012.

[38] SJ Wright, MD Blumenthal, M Pepper, D Anderson, GAC Jones, CA Nicoll, and DA Ritchie. Parallel quantized charge pumping. *Physical Review B*, 80(11):113303, 2009.

[39] JM Shilton, DR Mace, VI Talyanskii, MY Simmons, M Pepper, AC Churchill, and DA Ritchie. Experimental study of the acoustoelectric effects in gaas-algaas heterostructures. *Journal of Physics: Condensed Matter*, 7(39):7675, 1995.

[40] JM Shilton, DR Mace, VI Talyanskii, Yu Galperin, MY Simmons, M Pepper, and DA Ritchie. On the acoustoelectric current in a one-dimensional channel. *Journal of Physics: Condensed Matter*, 8(24):L337, 1996.

[41] John H Davies, Ivan A Larkin, and EV Sukhorukov. Modeling the patterned two-dimensional electron gas: Electrostatics. *Journal of Applied Physics*, 77(9):4504–4512, 1995.

[42] J Ebbecke, NE Fletcher, TJBM Janssen, FJ Ahlers, M Pepper, HE Beere, and DA Ritchie. Quantized charge pumping through a quantum dot by surface acoustic waves. *Applied Physics Letters*, 84(21):4319–4321, 2004.

[43] NE Fletcher, J Ebbecke, TJBM Janssen, FJ Ahlers, M Pepper, HE Beere, and DA Ritchie. Quantized acoustoelectric current transport through a static quantum dot using a surface acoustic wave. *Physical Review B*, 68(24):245310, 2003.

[44] Erwann Bocquillon, Vincent Freulon, François D Parmentier, Jean-Marc Berroir, Bernard Plaçais, Claire Wahl, Jérome Rech, Thibaut Jonckheere, Thierry Martin, Charles Grenier, et al. Electron quantum optics in ballistic chiral conductors. *Annalen der Physik*, 526(1-2):1–30, 2014.

[45] Wikipedia. Multiplexer — Wikipedia, the free encyclopedia. http://en.wikipedia.org/w/index.php?title=Multiplexer&oldid=866824832, 2018. [Online; accessed 15-November-2018].

[46] Haider Al-Taie, Luke W Smith, Reuben K Puddy, Patrick See, Jonathan P Griffiths, Ian Farrer, Geb AC Jones, David A Ritchie, Charles G Smith, and Michael J Kelly. Threshold tuning method for arrays of split-gate nanostructure transistors in series. In *Nanotechnology (IEEE-NANO), 2014 IEEE 14th International Conference on*, pages 490–493. IEEE, 2014.

[47] H Al-Taie, LW Smith, AAJ Lesage, P See, JP Griffiths, HE Beere, GAC Jones, DA Ritchie, MJ Kelly, and CG Smith. Spatial mapping and statistical reproducibility of an array of 256 one-dimensional quantum wires. *Journal of Applied Physics*, 118(7):075703, 2015.

[48] LW Smith, H Al-Taie, F Sfigakis, P See, AAJ Lesage, B Xu, JP Griffiths, Harvey Edward Beere, GAC Jones, and David Alastair Ritchie. Statistical study of conductance properties in one-dimensional quantum wires focusing on the 0.7 anomaly. *Physical Review B*, 90(4):045426, 2014.

[49] LW Smith, H Al-Taie, AAJ Lesage, KJ Thomas, F Sfigakis, P See, JP Griffiths, I Farrer, GAC Jones, David Alastair Ritchie, et al. Effect of split gate size on the electrostatic potential and 0.7 anomaly within quantum wires on a modulation-doped gaas/algaas heterostructure. *Physical Review Applied*, 5(4):044015, 2016.

[50] AAJ Lesage, Luke William Smith, H Al-Taie, P See, JP Griffiths, Ian Farrer, GAC Jones, David Alastair Ritchie, Michael Joseph Kelly, and Charles Gordon Smith. Assisted extraction of the energy level spacings and lever arms in direct current bias measurements of one-dimensional quantum wires, using an image recognition routine. *Journal of Applied Physics*, 117(1):015704, 2015.

[51] SJ Wright. *Quantised charge pumping in a perpendicular magnetic field*. PhD thesis, University of Cambridge, 2012.

[52] Hume Howe. *Amplitude, temperature, and frequency dependence of quantum pumps in semiconductor heterostructures*. PhD thesis, University College London, 2015.

[53] SP Giblin, SJ Wright, JD Fletcher, M Kataoka, M Pepper, TJBM Janssen, DA Ritchie, CA Nicoll, D Anderson, and GAC Jones. An accurate high-speed single-electron quantum dot pump. *New Journal of Physics*, 12(7):073013, 2010.

[54] SP Giblin, M Kataoka, JD Fletcher, P See, TJBM Janssen, JP Griffiths, GAC Jones, I Farrer, and DA Ritchie. Rectification in mesoscopic alternating current-gated semiconductor devices. *Journal of Applied Physics*, 114(16):164505, 2013.

[55] Ryan Hurley. Design considerations for esd/emi filters: I. *AND8200/D, ON Semiconductor Application Note*, pages 1–18, 2005.

[56] B Kaestner, V Kashcheyevs, S Amakawa, MD Blumenthal, L Li, TJBM Janssen, G Hein, K Pierz, T Weimann, U Siegner, et al. Single-parameter nonadiabatic quantized charge pumping. *Physical Review B*, 77(15):153301, 2008.

[57] Lukas Fricke, Michael Wulf, Bernd Kaestner, Frank Hohls, Philipp Mirovsky, Brigitte Mackrodt, Ralf Dolata, Thomas Weimann, Klaus Pierz, Uwe Siegner, et al. Self-referenced single-electron quantized current source. *Physical Review Letters*, 112(22):226803, 2014.

[58] M Kataoka, JD Fletcher, P See, SP Giblin, TJBM Janssen, JP Griffiths, GAC Jones, I Farrer, and DA Ritchie. Tunable nonadiabatic excitation in a single-electron quantum dot. *Physical Review Letters*, 106(12):126801, 2011.

[59] Vyacheslavs Kashcheyevs and Bernd Kaestner. Universal decay cascade model for dynamic quantum dot initialization. *Physical review letters*, 104(18):186805, 2010.

[60] Stephen Giblin, Akira Fujiwara, Gento Yamahata, Myung-Ho Bae, Nam Kim, Alessandro Rossi, Mikko Möttönen, and Masaya Kataoka. Evidence for universality of tunable-barrier electron pumps. *Metrologia*, 2019.

[61] Gento Yamahata, Stephen P Giblin, Masaya Kataoka, Takeshi Karasawa, and Akira Fujiwara. Gigahertz single-electron pumping in silicon with an accuracy better than 9.2 parts in 107. *Applied Physics Letters*, 109(1):013101, 2016.

[62] Gento Yamahata, Katsuhiko Nishiguchi, and Akira Fujiwara. Accuracy evaluation and mechanism crossover of single-electron transfer in si tunable-barrier turnstiles. *Physical Review B*, 89(16):165302, 2014.

A

Appendix

In this appendix we study for a certain width bar gate devices (for example 0.2 μm), how the pinch-off shift is affected by the distance from RF MUX in the new MUX bar gate array. There are 16 such same width devices on both the old and new MUX bar gate arrays. And we also want to learn how the pinch-off shift is affected by the vertical location of each row on the old MUX bar gate array. Besides, we compare the pinch-off shift for the 16 different width devices from the old MUX and new MUX.

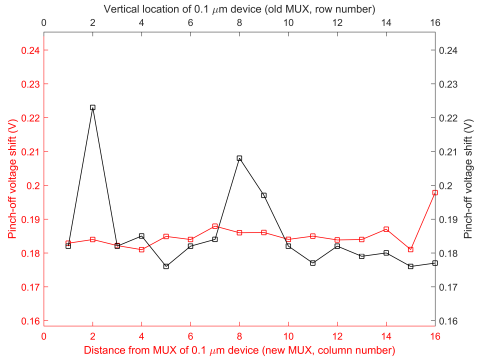

(a) 0.1 μm bar gate.

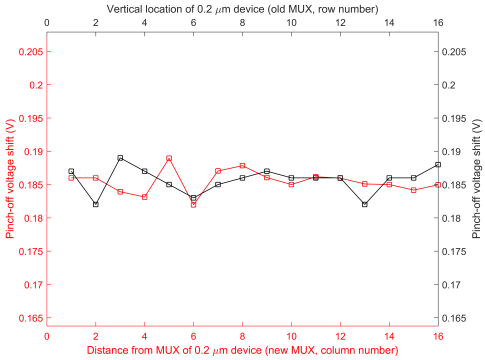

(b) 0.2 μm bar gate.

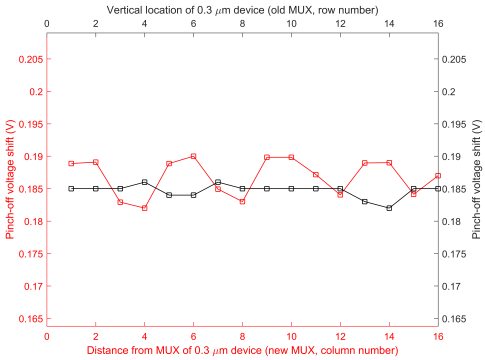

(c) 0.3 μm bar gate.

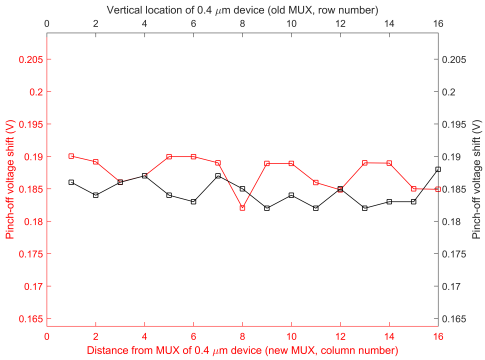

(d) 0.4 μm bar gate.

Figure A.1: Pinch-off voltage change of a certain width bar gate devices with 10 kHz, -10 dBm RF applied on the old and new MUX bar gate arrays. The black line is the pinch-off shift as a function of the vertical location of each row on the old MUX bar gate array, the distance between each row is 100 μm. The red line is the pinch-off shift as a function of the distance from RF MUX in the new MUX bar gate array, the distance between each row is 130 μm.

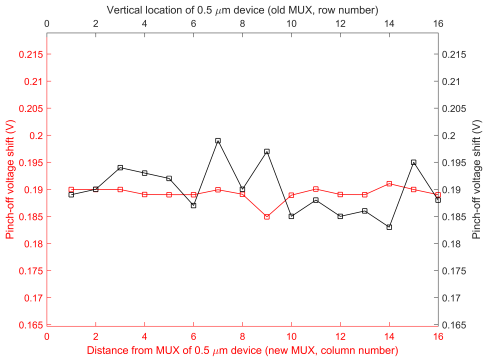

(a) 0.5 μm bar gate.

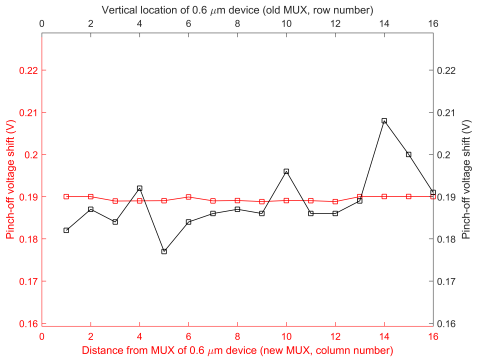

(b) 0.6 μm bar gate.

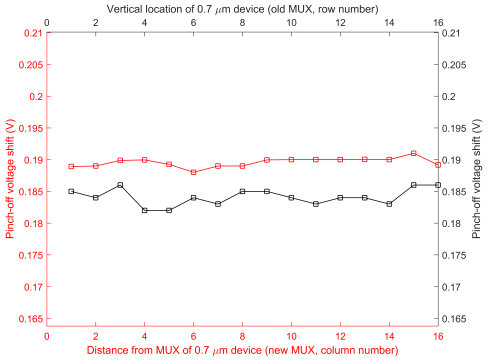

(c) 0.7 μm bar gate.

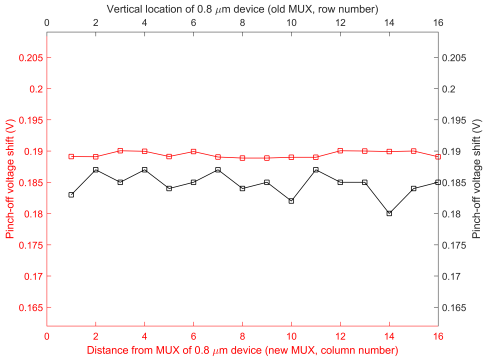

(d) 0.8 μm bar gate.

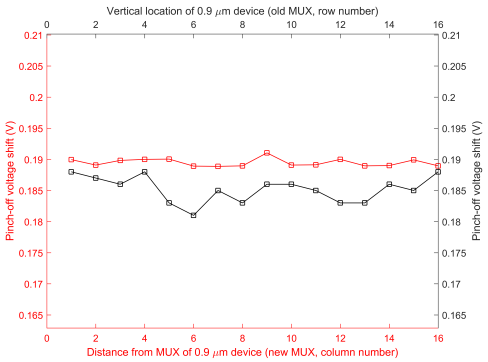

(e) 0.9 μm bar gate.

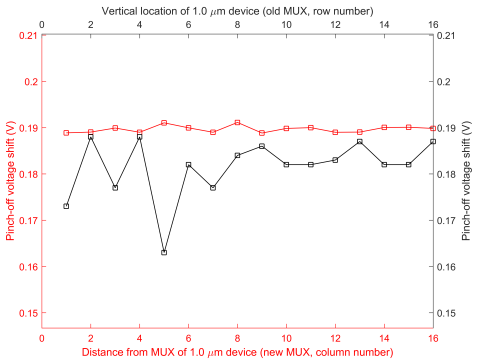

(f) 1.0 μm bar gate.

Figure A.2: Pinch-off voltage change of certain width bar gate devices with 10 kHz, -10 dBm RF applied on the old and new MUX bar gate arrays. The black line is the pinch-off shift as a function of the vertical location of each row on the old MUX bar gate array, the distance between each row is 100 μm. The red line is the pinch-off shift as a function of the distance from RF MUX in the new MUX bar gate array, the distance between each row is 130 μm.

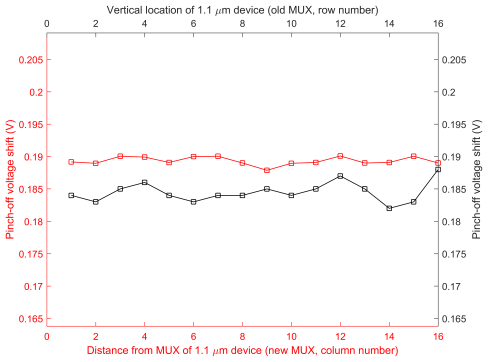

(a) 1.1 μm bar gate.

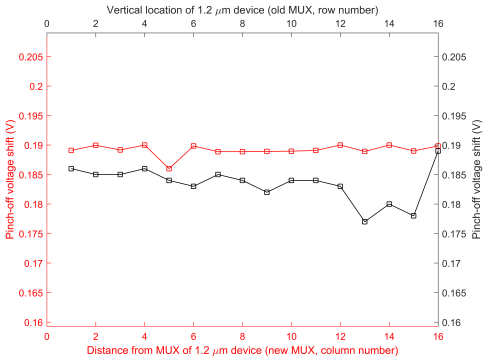

(b) 1.2 μm bar gate.

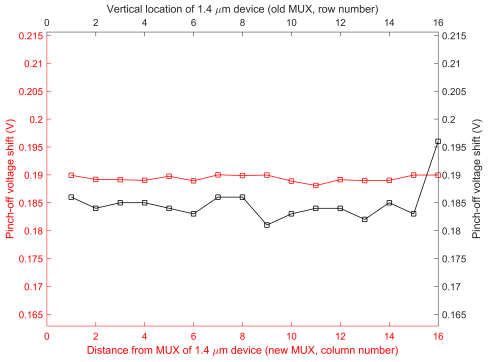

(c) 1.4 μm bar gate.

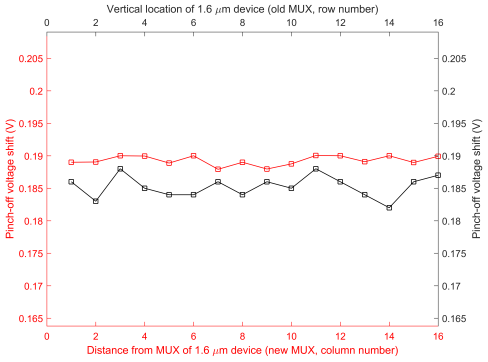

(d) 1.6 μm bar gate.

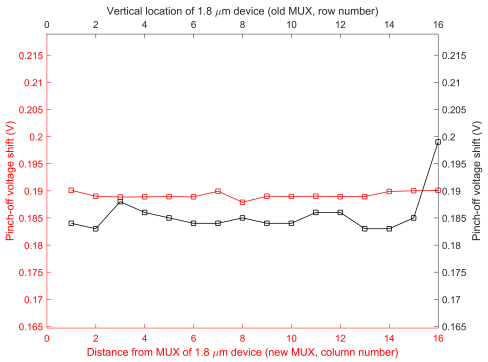

(e) 1.8 μm bar gate.

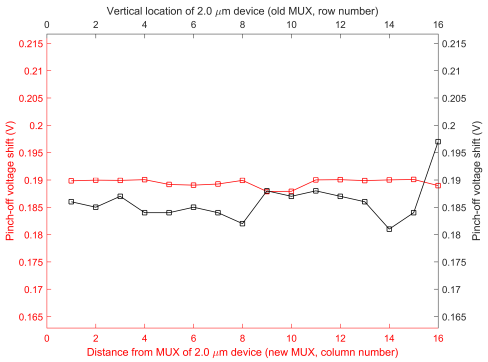

(f) 2.0 μm bar gate.

Figure A.3: Pinch-off voltage change of certain width bar gate devices with 10 kHz, -10 dBm RF applied on the old and new MUX bar gate arrays. The black line is the pinch-off shift as a function of the vertical location of each row on the old MUX bar gate array, the distance between each row is 100 μm. The red line is the pinch-off shift as a function of the distance from RF MUX in the new MUX bar gate array, the distance between each row is 130 μm.

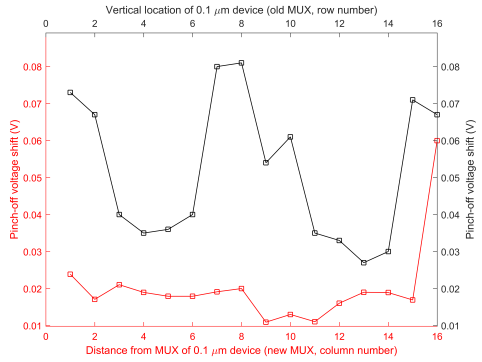

(a) 0.1 μm bar gate.

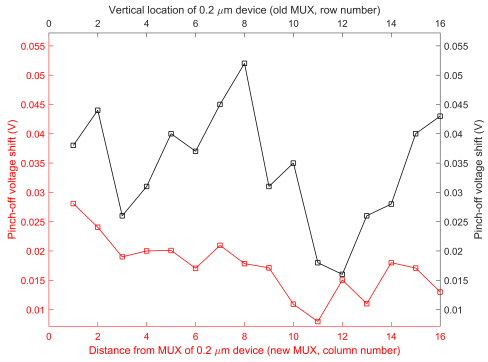

(b) 0.2 μm bar gate.

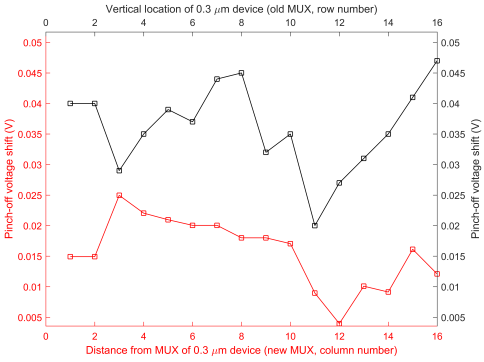

(c) 0.3 μm bar gate.

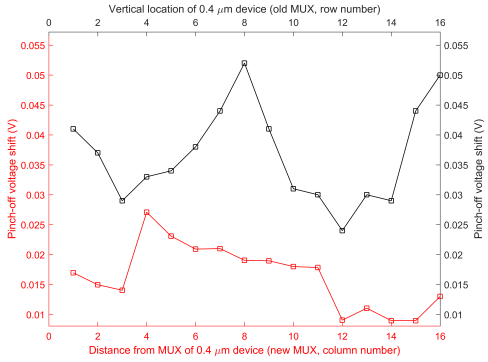

(d) 0.4 μm bar gate.

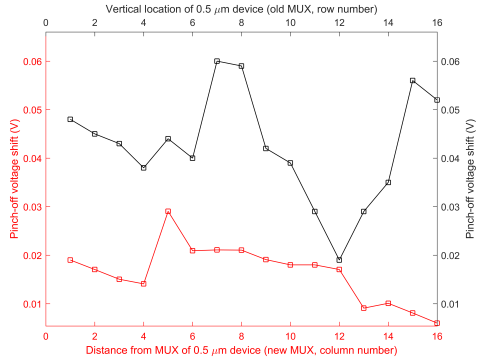

(e) 0.5 μm bar gate.

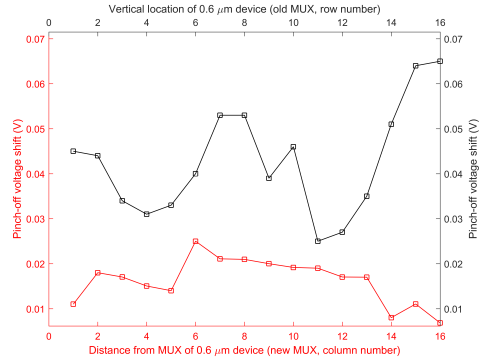

(f) 0.6 μm bar gate.

Figure A.4: Pinch-off voltage change of certain width bar gate devices with 110 MHz, -10 dBm RF applied on the old and new MUX bar gate arrays. The black line is the pinch-off shift as a function of the vertical location of each row on the old MUX bar gate array, the distance between each row is 100 μm. The red line is the pinch-off shift as a function of the distance from RF MUX in the new MUX bar gate array, the distance between each row is 130 μm.

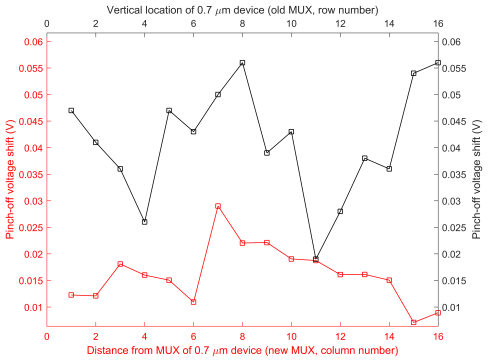

(a) 0.7 μm bar gate.

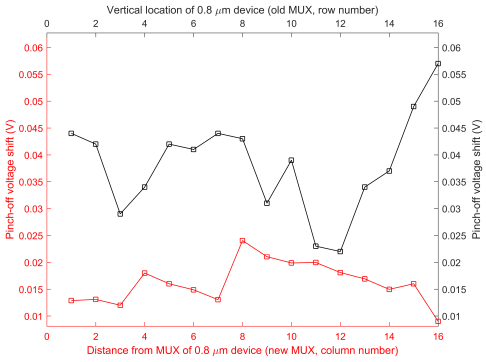

(b) 0.8 μm bar gate.

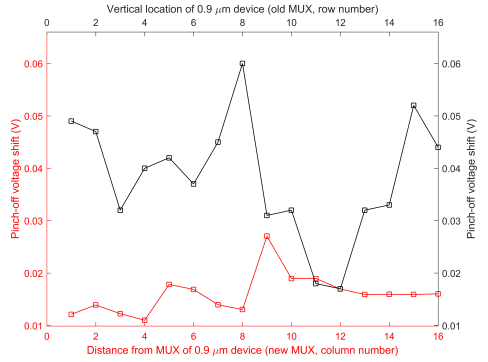

(c) 0.9 μm bar gate.

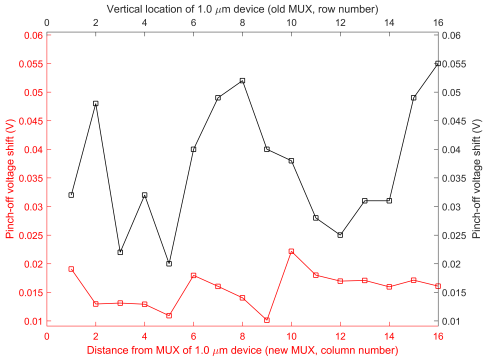

(d) 1.0 μm bar gate.

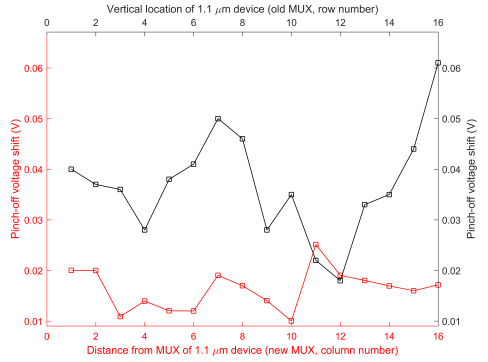

(e) 1.1 μm bar gate.

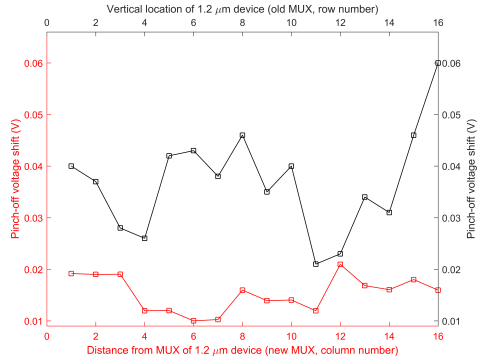

(f) 1.2 μm bar gate.

Figure A.5: Pinch-off voltage change of certain width bar gate devices with 110 MHz, -10 dBm RF applied on the old and new MUX bar gate arrays. The black line is the pinch-off shift as a function of the vertical location of each row on the old MUX bar gate array, the distance between each row is 100 μm. The red line is the pinch-off shift as a function of the distance from RF MUX in the new MUX bar gate array, the distance between each row is 130 μm.

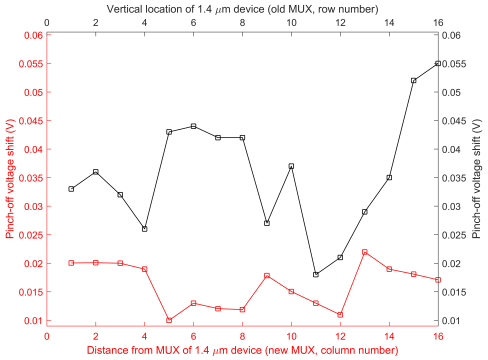

(a) 1.4 μm bar gate.

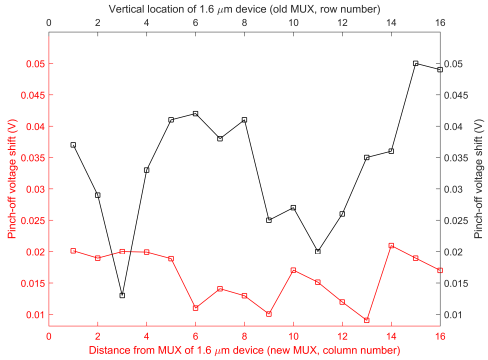

(b) 1.6 μm bar gate.

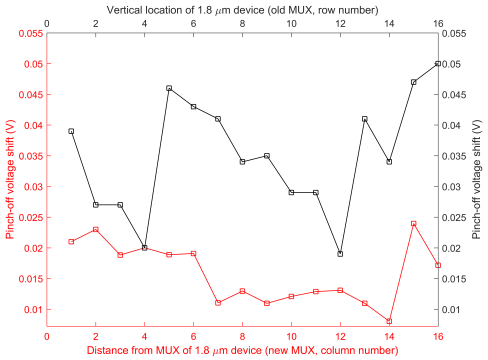

(c) 1.8 μm bar gate.

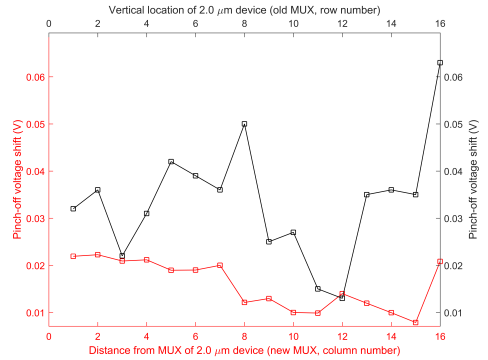

(d) 2.0 μm bar gate.

Figure A.6: Pinch-off voltage change of certain width bar gate devices with 110 MHz, -10 dBm RF applied on the old and new MUX bar gate arrays. The black line is the pinch-off shift as a function of the vertical location of each row on the old MUX bar gate array, the distance between each row is 100 μm. The red line is the pinch-off shift as a function of the distance from RF MUX in the new MUX bar gate array, the distance between each row is 130 μm.